METAL COMPLEXES DERIVATIZED METAL OXIDES AS NANOSTRUCTURED ELECTRODES IN ELECTROCHEMISTRY OR PHOTOELECTROCHEMISTRY

Hanlin Luo

A dissertation submitted to the faculty at the University of North Carolina at Chapel Hill in partial fulfillment of the requirements for the degree of Doctor of Philosophy in the Program of Materials Sciences.

Chapel Hill
2014

Approved by:

Thomas J. Meyer

Rene Lopez

Wei You

Scott C. Warren

James F. Cahoon

ABSTRACT

Hanlin Luo: Metal Complexes Derivatized Metal Oxides as Nanostructured Electrodes in Electrochemistry or Photoelectrochemistry
(Under the Direction of Thomas J. Meyer)

This dissertation focuses on three types of metal oxide nanostructured electrodes: niobium oxides (Nb_2O_5), strontium oxides ($SrTiO_3$), and antimony-doped tin oxides (ATO) in electrochemical and/or photoelectrochemical applications.

The chapter 2 and 3 discuss Nb_2O_5 and $SrTiO_3$ respectively. Both metal oxides were investigated as alternative photoanodes to titanium dioxides (TiO_2) in Dye-sensitized solar cells (DSSCs) and Dye-sensitized photoelectrosyntheis cells (DSPECs) because their conduction band are reported to be ~ 0.2-0.4 eV higher than TiO_2. Systematic investigations on Nb_2O_5 and $SrTiO_3$ in comparison to TiO_2 in equivalent devices were conducted, with conduction band, energy levels of chromophore, electron transfer dynamics, current-voltage relationship, and H_2 evolution or photo to current conversion efficiency discussed in the content. T-phase orthorhombic Nb_2O_5 films have shown conduction band potential slightly positive than that for anatase TiO_2. Trap state distributions, conduction band energies, and interfacial barriers appear to contribute to a slower back electron transfer rate, lower injection yield on the nsec timescale, and a lower V_{oc} for T-phase Nb_2O_5 compared to anatase TiO_2. In chapter 3, $SrTiO_3$ photoanodes indicated slower back electron transfer than TiO_2 after a Znic porphyrin sensitization. They suffered from the low energy conversion efficiency due to large interfacial charge transfer resistance between conduction band of $SrTiO_3$ and electrolyte and high conduction band edge.

The chapter 4 explores fabrication of 3-D mesoporous nanostructured ATO electrodes and their applications in electrochemical and photoelectrochemical catalysis. ATO nanostructured electrodes are characteristic of high interfacial area and drift electron transport. To obtain large-pore mesoporous materials, amphiphilic copolymers are chosen to as templates that unfortunately suffer from poor control of interaction with metal precursors and requirements for post annealing. Mesoporous ATO nanoelectrodes were fabricated based on ATO nanocrystals by microwave irradiation and grafted copolymers, poly (vinyl chloride)-g-poly (oxyethylene methacrylate) (PVC-g-POEM), templating. ATO nanoelectrodes indicated rapid electron transfer and proved to be suitable substrates for electrochemical catalysis after derivatized by a ruthenium water oxidation catalyst. Moreover, core-shell photoanodes, consisting of core of mesoporous conductive ATO film and shell of TiO_2 by atomic layer deposition (ALD), were derivatized by a ruthenium chromophore, working as a photocathode in H_2 evolution.

ACKNOWLEDGEMENTS

This dissertation would not have been possible without the support of many people. I would like to first express my sincere gratitude to my advisor, Dr. Thomas J. Meyer, for the opportunity to work in his lab on several exciting projects and all of the invaluable discussions that we have had about my research and my future career over the last five years. In particular, I am very thankful for the unique way Dr. Meyer supervised me, the skills that I picked up along the way, and most importantly the mindset I have now to solve real problems. Without his direction and constant support, I would have never completed all of the projects that I carried out. I would also like to thank the other members of my committee, Dr. Rene Lopez, Dr. Wei You, Dr. James F. Cahoon and Dr. Scott C. Warren for the consideration of this dissertation.

I am also grateful to the present and former members of the Meyer group throughout the past five years. It is a memorable experience to join such a great team, which I think should be nicknamed "RUBPY". Dr. Wenjing Song, Dr. Zuofeng Chen and Dr. Paul G. Hoertz mentored me in the hardest time when I first joined the group. Zhen Fang showed his great patience in teaching me the fundamentals of synthesis. Dr. Animesh Nayak prepared porphyrin compounds for me in the $SrTiO_3$ project. Special thanks go as well to Dr. M. K. Brennaman, Dr. Kenneth Hanson, Dr. Akitaka Ito, Dr. Javier J. Concepcion, Dr. Robert Binstead, Dr. Byron H. Farnum, Dr. Na Song, Dr. Aaron K. Vannucci, Dr. Kyung-Ryang Wee, Dr. Benjamin Sherman, Dr. Peng Kang and all other colleagues not listed here for their valuable discussions and advices throughout the past days. I would like to express my deep gratitude to Dr. Amar Kumbhar for training me on a lot of useful facilities of CHANL at unc, and to Dr. Rudresh Ghosh, Dr.

Myoung OK, Andrew S. Miller, Adam J. Rieth and Timothy Garvey for the help in measurements and preparation of metal oxides.

What's more, I would like to thank the Royster Fellowship for funding. We also acknowledge support for the purchase of instrumentation from the UNC EFRC: Center for Solar Fuels, an Energy Frontier Research Center funded by the U.S. Department of Energy, Office of Science, Office of Basic Energy Sciences under Award Number DE-SC0001011, and UNC SERC ("Solar Energy Research Center Instrumentation Facility" funded by the U.S. Department of Energy Office of Energy Efficiency & Renewable Energy under award number DE-EE0003188).

Finally, I truly appreciate my beloved parents and my husband, Demin Liu. Without your thoughtfulness and constant support, I would not have made it to this point of my life.

TABLE OF CONTENTS

LIST OF TABLES

LIST OF FIGURES

LIST OF ABBREVIATIONS

ALD	Atomic layer deposition
ATO	Antimony doped tin oxide
ATR-FTIR	Attenuated total reflectance Fourier transform infrared spectroscopy
ATRP	Atom-transfer radical polymerization
AZO	Aluminum doped zinc oxide
BET	Brunauer, Emmett, and Teller (according to gas absorption)
CV	Cyclic voltammetry
DSSCs	Dye-Sensitized Solar Cells
DSPEC	Dye-sensitized photoelectrosyntheis cells
EDS	Energy dispersive X-ray analysis
$EDTA^{4+}$	Ethylenediaminetetraacetic tetra-anion
EIS	Electrochemical impedance spectroscopy
EISA	Evaporation induced self-assembly
FE-SEM	Field emission scanning electron microscopy
FF	Fill factor
FIB	Focused ion beam
FTIR	Fourier transform infrared

FTO	Fluorine doped tin oxide
FWHM	Half maximum intensity
G1	PVC-g-POEM with starting material weight ratio PVC: POEM = 3: 7.5
G2	PVC-g-POEM with starting material weight ratio PVC: POEM = 3: 4.5
GC	gas chromatography
GPC	Gel permeation chromatography
GZO	Gallium doped zinc oxide
HPC	Hydroxypropyl cellulose
HRTEM	High-resolution transmission electron microscopy
IPCE	Incident-photon- to-electron conversion efficiency
IR	Infrared
ITO	Tin doped indium oxide
IUPAC	International Union of Pure and Applied Chemistry
Mebimpy	2,6-bis(1-methylbenzimidazol-2-yl)pyridine
MeCN	Acetonitrile
MLCT	Metal-to-ligand charge transfer
MT	Mott-Schottky plot

NBB	Nanobuilding blocks
NHE	Normal hydrogen electrode
NIR	Near Infrared
NMP	1-Methyl-2-pyrrolidinone
n-TCO	n type Transparent Conducting Oxides
P123	poly (ethylene oxide- propylene oxide − ethylene oxide)
PDI	Polydispersity index
PLD	pulsed laser deposited
POEM	poly(ethylene glycol) methyl ether methacrylate
p-TCO	p type Transparent Conducting Oxides
PVC-g-POEM	poly(vinyl chloride)-g-poly(oxyethylene methacrylate)
PVC	poly(vinyl chloride)
Q	total charge
RuP	$[Ru(bpy)_2(4,4'-(PO_3H_2)_2bpy)]^{2+}$
SCE	Saturated calomel electrode
SEM	Scanning electron microscopy
TA	Transient Absorption

TCOs	Transparent Conducting Oxides
TEM	Transmission electron microscope
TEOA	triethanolamine
TGA	Thermogravimetric analysis
THF	Tetrahydrofurane
UV	Ultraviolet
XPS	X-ray photoelectron spectroscopy
XRD	X-ray diffraction
ZnPC	Znic porphyrin used in chapter 3, see scheme 3-1
1-PO_3H_2	$[RuII(Mebimpy)(4,4'\text{-}(PO_3H_2P)_2bpy)(OH_2)]^{2+}$
2-PO_3H_2	$[RuII(Mebimpy)(4,4'\text{-}(PO_3H_2CH_2)_2bpy)(OH_2)]^{2+}$

LIST OF SYMBOLS

°C	degrees Celsius
C	Coulomb
Ω	Ohm
e	electronic charge
ε	molar absorption coefficient
η_{col}	electron collection efficiency
k_{bet}	back electron transfer
eV	Electron volt (1 eV = 1.602×10^{-19} J)
ρ	resistivity
σ	conductivity
m*	effective electron mass
N	carrier concentration
μ	carrier mobility
Φ_{Fa}	Faradaic efficiency
Φ_{H2}	H_2 quantum yields
τ	relaxation mean time between collisions
λ	wavelength

λ_{ex}	wavelength of excitation
Γ	Surface coverage
μm	micrometer
π	pie
S	Siemens, unit of conductivity
T_g	glass transition temperature
V	volt
V_{oc}	open circuit voltage
η	overall solar-to-electrical energy conversion efficiency
J_{sc}	short-circuit current

Chapter 1: Introduction

1.1 Semiconductor materials past TiO_2 for photoanodes, photocathodes and tandem cells

Back to 1960s, dye molecules were verified to not only absorb solar irradiation, but inject electrons into n-type semiconductor conduction band. In the following years, dyes were proved to work efficiently when they were chemically linked on the surface of semiconductors either by carboxylic acid or phosphoric acid groups.[1] The idea led to employment of dispersed particles to provide large area for dye/semiconductor interface,[2] and subsequently photoelectrodes.[3,4] A well-known breakthrough for high efficient Dye-Sensitized Solar Cells (DSSCs) in 1991 by Grätzel used a mesoporous TiO_2 photoelectrode derivatized by a monolayer of a sensitizer.[5] Nanocrystalline TiO_2 layer, approximately, magnifies surface area to a 1000 times compact analogs.[6] Besides, low conductivity, absence of built-in electrical field, and three-dimensional architecture distinct mesoporous TiO_2 film from bulk TiO_2. [3] Meanwhile, TiO_2 is advantageous for its low cost, earth abundance, and non-toxicity. Therefore, TiO_2 becomes a preferred choice of photoelectrodes in dye derivatized solar devices, and holds the world record of power conversion efficiency in DSSCs with industrial mass production (G24Innovation, SONY, DYESOL).[7]

The basic operational principle of DSSCs is displayed in Figure 1-1.[8] The photoanode, made of a mesoporous nanostructured metal oxide derivatized by certain chromophore, accepts electrons from the photo-excited dye which is thereby oxidized. The oxidized dye in turn

oxidizes the redox mediator present in the electrolyte. The mediator is regenerated by reduction at the cathode through electrons circulated by the external circuit.

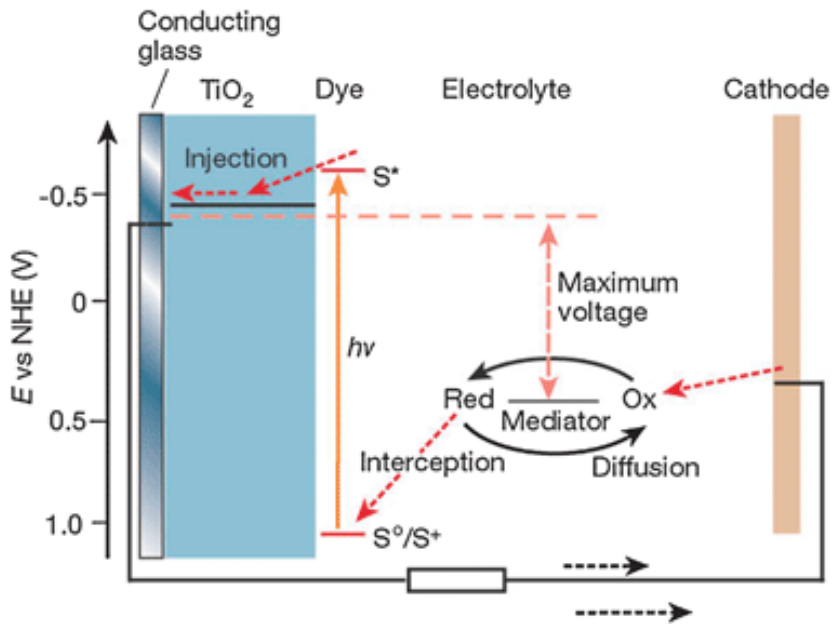

Figure 1-1. Schematic illustration of a typical DSSC. Adapted from reference 8.

In general, improvements of light absorption, electron injection, and electron collection are the key requirements for photoelectrode materials. Specifically, for maximum incident light absorption, photoelectrodes will have:[9] (1) appropriate band gap to obtain high transparency; (2) sufficiently large internal surface area ; (3) long term stability under irradiation and most chemical environment. To facilitate electron injection, a large density of unpopulated states (conduction band) should positively exist at the potential of dye excited state, $dye^{*/+}$, for photoanodes; whereas populated states (valence band) should negatively lie at the potential of dye oxidized state, $dye^{*/-}$, for photocathodes (all in NHE scale). Electron collection efficiency normally depends on the competition between electron diffusion that is the rate of electrons collection, and electron lifetime that is the rate of electron interception and recombination.[9,10] Nanoparticle films show significantly slow charge transport, governed by trap-limited diffusion

process through percolation network of nanoparticles.[11,12] Drift transport is inhibited by ions in the electrolyte that screen macroscopic electric fields.[13] Nonetheless, the charge collection efficiency is high owing to the slow back electron transfer of injected electrons with oxidized dye or redox mediator (eg. I_3^-). [13,14] Thus electron diffusion length in these devices is long, up to several tens of micrometers at low light intensities, [15-17] even though with small electron diffusion coefficient. Electron kinetics inside photoelectrodes is in fact highly complicated, and for detailed analysis, readers are referred to literatures.[18-21]

Despite the success of TiO_2 as a photoanode in the past two decades, forefront research tends to explore supported metal oxide other than titania, especially in H_2O splitting or CO_2 reduction photoactive electrodes, among which metal oxides such as ZnO, SnO_2, and Nb_2O_5 et al. indicate promising properties. Here we give a short summary on recent progress of nanostructured photoelectrodes in dye sensitized photochemical devices.

1.2 n-type photoanode materials

1.2.1 ZnO

ZnO has the longest history as photoanode candidates in DSSCs. It has similar band gap (3.2 eV) and band edge position to anatase TiO_2, [22] but larger electronic mobility that would benefit electron transport with decreased recombination.[23] In contrast to TiO_2, no need for a high temperature annealing step endows ZnO with great potential to be produced in an abundance of nanostructures: i.e., nanoparticles, [24] nanosheets, [25]nanobelt, [26] nanowires, [27] tetrapods, [28] etc. To date, the highest conversion efficiency for ZnO-based DSSC is 7.5 % that is much lower than record of titania. [29] More detailed reviews of ZnO as photoanodes was reported here. [23,30-32]

The limited performance for ZnO might be traced back to its instability in carboxylated or phosphonated dyes possessing low pKa,[30] resulting in a thick layer of znic carboxylate/phosphonate crystals of dyes.[33] ZnO with a point of zero charge (PZC) ~ 9 is more basic than TiO2 with ~ 6.[34] At pH lower than PZC, surface of ZnO is predominantly positively charged, and consequently absorbed protons will dissolve ZnO. The Zn^{2+}/dye layer is isolated from ZnO by the dye monolayer, and thus inactive to electron injection.[35] Moreover, dyes containing complexing agents can remove zinc cations from the ZnO lattice.[36] In view of these, ruthenium dyes with only one carboxylic group[36] and organic dyes(e.g. indoline dye[37]) were proved to reduce dye precipitation and achieve better performance. What's more, chemical stability could be increased by forming ZnO core/shell structure with coatings, such as SiO_2,[38] TiO_2[39] and Al_2O_3.[35]

Additionally, ZnO is found to have poor electron injection efficiency. Both electron injection into conduction band of TiO_2 and ZnO is biphasic kinetics, comprising one fast component of less than 100 fs and slower components on a picosecond time scale.[40,41] Nonetheless, for electron injection with Ru dye, ZnO was dominated by slow component, while TiO2 was the opposite. This is presumably explained from a band structure view, that is, since conduction band of ZnO was largely comprised of empty s and p orbital of Zn^{2+},[42] accordingly, the density of conduction band states is reported to be two orders of magnitude higher than TiO_2.[43] Stockwell et al.[44] also proposed another possibility. They compared C343 derivatized ZnO with TiO_2, suggesting that low efficiency might be due to a relatively strong electrostatic interaction between bound electron/oxide dye pairs in ZnO, as it has a smaller permittivity (~ 10) than TiO2(~ 30-40).[33]

1.2.2 SnO_2

SnO_2 is a wide band gap (~ 3.6 eV) n-type semiconductor with fast electron transport.[45,46] Owing to the large band gap, SnO_2 is less likely to experience direct band excitation under UV irradiation, and thus has a decent long term stability in chemical environment[47]. SnO_2 has a relatively positive conduction band level compared to TiO_2 from 0.3 [48] 0.4,[49] 0.5 eV,[50,51] frequently leading to low open-circuit voltage values.[52-54] On the other hand, this allows electron injection from sensitizers with low lying LUMOs that can hardly realize in TiO_2, such as perylene dyes[55] as well as a probably faster electron injection than in their TiO2 counterparts.

Nanostructured SnO_2 has been intensively studied as photoelectrodes.[55,56] However, power conversion efficiency of cells is not as good as TiO_2 or ZnO.[57,58] Birkel et al. examined morphological impact on SnO_2-based DSSCs via a microwave-assisted high-throughput method. [59] Different nanostructures are tuned according to various precursors, but all SnO_2 nanocrystal products belong to the same cassiterite phase ($P4_{2/mnm}$ space group). Meanwhile, as-synthesized nanorod-rich SnO_2 electrodes have electron diffusion efficiency (5×10^{-4} cm^2 s^{-1}) of ten times faster than TiO_2, but a lower V_{oc} than TiO_2 that is in accordance with conduction band position. Specifically, a power conversion efficiency of 3.2% was observed, which is the highest efficiency record of untreated SnO_2/DSSCs. The poor performance probably originates from the fast electron recombination [49] and weak adsorption of acid dyes.[60] Tiwana et al. carried out a comparative study of TiO_2, ZnO, and SnO_2 nanoparticle films derivatized with Z907 ruthenium dye.[58] Like ZnO, electron injection from the sensitizer to SnO_2 nanostructured film was dominated by a slow component over tens to hundreds of picoseconds, limiting the overall photocurrent generated by the solar cell. While for TiO_2, the injection process only last a few picoseconds. Green et al. show that SnO_2 films derivatized with N3 dye have faster

recombination kinetics of injected electrons both to dye cation and redox electrolyte, as a consequence of lower trap densities and large electron diffusion constant inside SnO_2 films. [49] One typical strategy to boost SnO_2 photoanodes performance is to modify surface by coatings such as TiO_2,[57,61,62] ZnO, Al_2O_3,[63] MgO,[47,57,60] Y_2O_3.[56] The PZC of SnO_2 is around 4-5,[34] and thus surface of oxide coating is more basic than SnO_2, resulting in a more favorable attachment of dye carboxylic acid groups.

1.2.3 Zn_2SnO_4

Ternary oxide photoelectrode, Zinc stannate (Zn_2SnO_4), has high electron mobility and satisfying chemically stability due to wide band gap of 3.6 eV. [64] The nano-sized Zn_2SnO_4 have been employed as photocatalysts to decompose benzene in aqueous solution.[65] Interests of Zn_2SnO_4 in dye sensitized solar devices was initiated by results that mesoporous photoanode mixed of ZnO and SnO_2 generated greatly enhanced efficiencies.[66] Wu group[67] and Hagfeldt group,[68] at the same time, introduced Zn_2SnO_4 as a new type of photoanodes in DSSC tests with efficiency up to 3.8 %. Zn_2SnO_4 loaded with N719 Ru dye is more stable against acidic sensitizers than ZnO, as well as it has much better performance than pure SnO_2 cell. Photoelectrochemical measurements point out that it has higher conduction band edge energy than TiO2.[68,69] Wu and co-workers first displayed the flat band potential of nanocrystalline Zn_2SnO_4 depended on pH of aqueous solution that is similar to that of nanostructured TiO_2 electrodes.[70] Kou et al. further established a Nernstian relationship of flat band potential to pH. Trap state density also change according to pH variation, implying that traps are mostly surface-related states.[69] Recently, hexagonal nanoplate/micro-octahedron Zn_2SnO_4 was prepared with a photo conversion efficiency of 3.1 %.[71]

Additionally, Zn_2SnO_4 nanowire was also first reported to have a photo conversion efficiency of 2.8 % in DSSCs.[72] An increment of Voc (> 0.1 V) was frequently observed than nanocrystalline counterparts. The electron diffusion length of the Zn_2SnO_4 nanowire was tested to be longer than that of nanoparticle film by EIS. More detailed studies on electron transport dynamics in Zn_2SnO_4 film are still under future investigation.

1.2.4 Nb_2O_5

Nb_2O_5 is a large band gap n-semiconductor with a conduction band comprised of empty Nb^{5+}4d orbitals[73] and a conduction band generally accepted to be 0.1-0.3 eV higher than TiO_2.[53,74-77] Several groups have prepared Nb_2O_5 as nanoparticles,[74,78-81] nanobelts,[82] nanowires,[83] nano-forests,[84] blocking layers,[85] and TiO_2–Nb_2O_5 bilayers[86,87] in DSSCs. Despite that Nb_2O_5 has several different crystal structures: monoclinic, hexagonal, and orthorhombic; all unit cell dimensions are large, bringing up difficulties in enlarging internal surface area. Sayama et al. [76] carried out a comparative study regarding DSSC device performance of TiO_2, Nb_2O_5, ZnO, SnO_2, In_2O_3, WO_3, Ta_2O_5, and ZrO_2, among which Nb_2O_5 had the second highest IPCE and highest value of Voc. Ou et al.[88] recently illustrated that a crisscross nanoporous Nb_2O_5 film(~4 μm) prepared by elevated temperature anonization showed a remarkably higher efficiency of 4.1 %, compared to nanotubular TiO_2 DSSCs attached with N3 dye. Impedance spectroscopy implied that was due to large charge transport resistance and long electron lifetime.

Literature values for E_g and E_{cb} for Nb_2O_5 are ambiguous in that they are typically cited without specification of crystal structure, morphology, and measurement conditions.[6,53,76,79,89-93] One of the most cited paper reported that E_g ~ 3.4 eV and E_{cb} -0.5 V Vs NHE at pH 7 with the latter 0.2V more negative than TiO_2[94] although the sample was prepared by metal anodic

oxidation without thermal treatment and was possibly amorphous. Another widely referred to value for E_{cb} places it ~0.2 eV negatively shifted (NHE scale) compared to anatase TiO_2 for a sample that was TT-phase (hexagonal crystal).[92,95] Although Nb_2O_5 is generally considered to have a conduction band negatively shifted than TiO_2, we found out that Nb_2O_5 nanoporous orthorhombic film synthesized in our lab exhibited slightly positively conduction band (< 100mV) to anatase TiO_2 film by spectroelectrochemistry measurements.[96] Conduction band edge for PLD Nb_2O_5 film of the same crystalline structure also showed the positively shift compared to PLD TiO_2 counterparts measured in vacuum. Thus, it is too general to conclude that Nb_2O_5 has a higher conduction band than TiO_2 and exemptions should apply in specific case. In our system, Nb_2O_5 was derivatized by RuP in the presence of EDTA as an electron donor. Hydrogen evolution was maintained in the assistance of applied bias under steady state illumination. Nb_2O_5 displayed a slower component of back electron transfer between injected electrons and oxidized dye than TiO_2. This might be related to trap-dependent electron diffusion process. A lack of deep trap states in Nb_2O_5 films contributed to a slow recombination component. For hydrogen production efficiency, we saw a comparable but no superior for Nb_2O_5 performance to TiO_2 in DSPEC.

1.2.5 **$SrTiO_3$**

As a ternary metal oxide, $SrTiO_3$ with perovskite type cubic structure shares a similar structure to anatase TiO_2,[97] where titanium atoms are in 6-fold octahedral coordination in $SrTiO_3$. Grain size up to 80nm for $SrTiO_3$ behaves electrically mesoscopic as a result of a high dielectric constant (e.g. ~175 at 300 °C[98]) . [99]$SrTiO_3$ has a more negative flat band potential than anatase TiO_2 [48]and therefore a $SrTiO_3$-based DSSC is expected to have a higher Voc than anatase-based one. [100] Burnside et al. [100] carried out flash laser photolysis and absorbance

studies, proposing that the low photocurrents observed for N3 sensitized $SrTiO_3$ nanofilms could be attributed to poor dye loading on the oxide surface, but not to electron injection or transport problems in the semiconductor. Yang et al. found out flat band potential and trap states of $SrTiO_3$ nanocrystalline film greatly dependent on the pH of aqueous electrolyte solution.[101] Flat band edge of $SrTiO_3$ was correlated linearly with pH by expression: $E_{fb}= -0.59 - 0.04pH$ (Vs Ag/AgCl). Later, Yang group [102] tested flat band edges of $SrTiO_3$ nanoparticle film in propionitrile (PN), acetylacetone (Acac), and PN/Acac in order to study the solvent chelation effects on the band energies. They found out a very negative flat band edge at the present of exclusive tetrabutylammonium ions. Addition of lithium cations will shift flat band positively and reduce trap states densities as well. They also tuned band energies of N3-derivatized $SrTiO_3$ film by optimizing electrolyte composition. The best $SrTiO_3$ DSSC cell in their paper was using Acac, giving high open-circuit voltage of 0.6V and short circuit current of 0.41 $mA \cdot cm^{-2}$ under 100mW.cm^{-2} Xe lamp, which could be explained by the smallest trap state density and thus less recombination.

WO_3 has recently been developed as photoanodes in dye sensitized solar cells.[103] It has a narrower band gap ranging from 2.6 to 3.1 eV for common crystal phases[104] when compared to anatase TiO_2. Moreover, WO_3 is chemically stable, facile to synthesis, and [105-107] tunable to morphologies.[103] Generally speaking, conduction band edge for WO_3 is more positive than TiO_2.[108] Sadek et al. first utilized nanoplatelets WO_3 by anodization at elevated temperatures in DSSCs.[109] Nanoparticle based WO_3 based DSSC reported by Zheng et al. had a low power conversion efficiency of 0.75 %, which was improved to 1.46 % after $TiCl_4$ treatment. The relatively low efficiency was attributed to very acidic metal oxide surface of poor dye loading.[110]

1.2.6 **Other photoanodes**

In addition to simple binary or ternary photoanodes described above, other metal oxides receiving less attention as TiO_2 replacement are still under investigation, such as Ta_2O_5,[111] CeO_2,[112,113] $BaSnO_3$.[114,115] There is also an extensive literature of doped TiO2 materials. One best example is tantalum (Ta) doped TiO_2. [116-118] Feng et al. [117] successfully fabricated DSSCs employing Ta doped rutile TiO_2 nanowires, achieving a high open circuit voltage of 0.87 V that is close to the theoretical maximum of 0.95 V.[119] The significantly enhanced V_{oc}, likely, was due to higher electron concentration introduced by Ta^{5+} filling surface traps, leading to a higher quasi-Fermi level. Liu et al. [118] illustrated that Ta-doped TiO_2 nanocrystalline photoanode improved efficiency from 7.40 % to 8.18 %. Ta doping brought about a positive shift of conduction band, fast electron transport and concentration of carriers, resulting in better DSSC device performance. Another case in point is Nb-doped TiO_2.[120-124] Lü et al. saw an overall efficiency of 7.8 % with a remarkable increment efficiency up to 18.2 % for 5 mol % Nb doped TiO_2. [121] After doping, flat band edge was found to be positively shifted to that of TiO2, followed by argument of the photoanode conductivity. In addition, other doped TiO2 photoelectrodes, such as Sn,[125,126], W,[127] Cr,[128] Sr, Sb,[129] Zn,[130] Cu,[131] Ru,[132] Zr,[133] Ge,[133] N,[134,135] B,[134,136] I,[137] are under vigorous study for dye sensitized solar cells. A summary of different band position for different n type semiconductors is shown in Figure 1-2.[8]

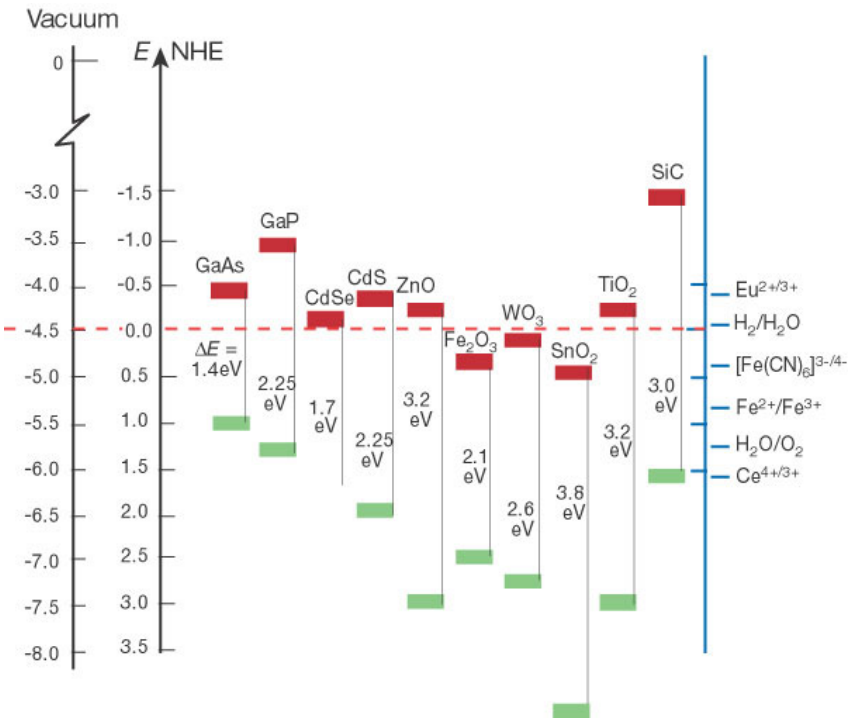

Figure 1-2. Band positions of several semiconductors in contact with aqueous electrolyte at pH 1. Adapted from reference 8.

1.3 p-type photocathode materials

Compared to n type photoanode materials, there has been limited attention on improving p-type photocathodes in dye sensitized solar devices. For a typical p type metal oxide, the key is light-induced hole transfer from the excited dye which is equivalent to electron transfer from the valence band of the semiconductor, equation 1-1. Thus, the upper edge of valence band have to be above the dye*/- couple. The photocathode should be transparent in visible spectrum and chemically stable. A summary of the properties and applications of common p-type materials is presented below with readers referred to the literature for further details. [50,138,139]

$$MO_x\text{-dye} \xrightarrow{h\nu} MO_x\text{-dye}^* \rightarrow MO_x(h^+)\text{-dye}^- \qquad (1\text{-}1)$$

1.3.1 **NiO**

The most comprehensively-studied photocathode is NiO, most likely as a consequence of years of studies of NiO films for electrochromic devices. NiO is a wide band gap semiconductor ranging from 3.6 to 4 eV of a cubic burnsenite structure.[138] Its valence band and conduction band approximately located at 0.54 V and -3.06 V, respectively, at pH 7.[138-140] In 1999, Lindquist and co-workers[141] reported the first p-type DSSC, to our knowledge, using a nanoporous NiO derivatized by tetrakis(4-carboxyphenyl)porphyrin (TPPC) and erythrosin B with a fairly low incident photon-to-current conversion efficiencies of 0.24 % and 3.44 %, respectively, under AM 1.5. The low overall efficiency (<0.01%) and V_{oc} was accounted for the small energy difference between the NiO valence band and the redox system, I_2/I_3^-. Recently, several groups have made prominent progress on improving V_{oc} by using new types of redox mediator for p-type photocathodes.[142-144]

A large number of p-type sensitizers have been investigated, such as porphyrins,[141,145] coumarin,[146,147] perylene,[148] arylamine-based.[149,150] However, most have an IPCE value of less than 10 %. Donor-acceptor type dyes were carefully designed with anchoring group located on the donor side. For example, Bach and co-workers[151] successfully built perylene imide based dyes that reaching the record power electricity conversion efficiency of 0.41 % at present. Sun and co-workers also developed a series of donor acceptor dyes[152-154] (i.e. P1, P4, P7) with triphenylamine as the donor and dicyanovinylene as the acceptor. P1 in particular could give satisfying efficiencies- combined with a double layer NiO nanoporous film, the efficiency would be 0.15 % and an IPCE of 64 % under AM 1.5. In addition, the same group integrated a H_2 evolving catalyst Co1 with P1 derivatized NiO film into a DSPEC device under 400nm light

illumination, in which electrons were transferred from reduced dye $P1^-$ to Co1(II), forming Co(I) that starting proton reduction.[155]

A possible reason is that significantly slow hole diffusion coefficient in NiO films (10^{-8}-10^{-7} $cm^2 \cdot s^{-1}$), which is more than 2 orders of magnitude lower than electron diffusion coefficient of TiO_2.[156,157] Morandeira et al.[146] , for example, studied Coumarin 343(C343), a benchmark of p type sensitizer. They found out that the hole injection occurred at 0.2-2 ps and hole-reduced dye recombination majorly occurred within 20 ps; whereas regeneration of ground state dye happened at a microsecond timescale which was unable to beat the ultrafast charge recombination.

Hole diffusion in NiO films (10^{-8}-10^{-7} $cm^2 \cdot s^{-1}$) is 2 orders of magnitude slower than electron diffusion in TiO_2.[156,157] This increases the possibility of holes anniled with redox mediator, leading to poor device performance. A widely existed fast charge recombination with NiO films also limits photoconversion efficiency. With [146] Coumarin 343(C343) as a benchmark, hole injection was shown to occur in 0.2-2 ps and back electron transfer within 20 ps while regeneration of ground state dye occurred on the microsecond timescale unable to beat ultrafast charge recombination. [146]

1.3.2 **Copper-based photocathodes**

Although less explored, p-type photocathodes other than NiO have gradually strong potential in DSSC/DSPEC applications, such as p-GaP,[158] N-doped Ta_2O_5.[159,160]

Copper based semiconductor is a promising category for NiO replacement. Sumikura et al. [161] prepared Cu(II)O p-type materials sensitized with several dyes including Fast Green FCF, NK-3628, and N3. Though small efficiency was obtained in DSSC device, it in principle

validated the possibility of using CuO as photocathodes. Copper(I) oxide has a narrow band gap (2.0-2.2 eV) and conduction band edge at -1.15 V Vs NHE at pH 7,[162] suitable for hydrogen production or CO_2 reduction. Grätzel et al. applied $ZnO/Al_2O_3/TiO_2$ atomic layer deposition to stabilize Cu_2O oxide surface in aqueous solution, obtaining consistent H_2 generation.[163] Despite no direct report exists, stabilized Cu_2O could be utilized in dye sensitized solar devices.

In addition, $CuMO_2$ (M=Metal) semiconductor family also contains good NiO alternatives. Bandara et al. employed p-type $CuAlO_2$ semiconductor with band gap 3.55 eV to make a N3 sensitized solar cell.[164] $CuGaO_2$ delafossite nanoplates sensitized by P1 recently was utilized in p-type DSSCs, [125] possessing a band gap of 3.60 -3.8 eV and valence band edge of 0.6 V vs NHE.[165] It is white p-type materials, presenting an advantage over NiO by preventing completion of visible light between metal oxide film and sensitizers. By employing a $Co^{3+/2+(}$dtb-bpy) electrolyte, DSSC device achieved a V_{oc} of 0.357 V under AM 1.5, accompanied with a saturation of photovoltage up to 0.464 V using increased light intensity.

1.4 Tandem applications

An n-type photoanode and a p-type photocathode could be combined together to fabricate a tandem solar cell. Theoretical calculation implies that efficiency for tandem cells should overcome the limit of single junction solar cell.[166,167] A tandem DSSC would benefit from two dyes with complimentary spectral harvest on each single compartment, and from an increased V_{oc} that has a maximum value of the sum of V_{oc} for two compartments.[168] Tandem cells could be connected in parallel[169], face to face,[170] or in series.[171] He et al. first experimentally demonstrated an DSSC N_3 derivatized tandem cell comprising a TiO_2 photoanode and NiO photocathode,[138] obtaining V_{oc} of 0.732 V and overall efficiency of 0.39 %. Particularly, V_{oc} for tandem was contributed by 0.65 V from TiO_2-based n-DSSC and 0.08 V from NiO-based p-DSSC. Suzuki et

al. improved NiO film internal surface area by a triblockcopolymer template(poly(ethylene oxide)−poly(propylene oxide)−poly(ethylene oxide) (PEO-PPO-PEO, Pluronic P123) loaded with more efficiency dye NK-2684, giving rise to a higher overall efficiency of 0.66 % and V_{oc} of 0.918 V.[172] Hammarström et al. improved open circuit voltage of tandem DSSC cell up to 0.91 V by applying a cobalt redox mediator with NiO and TiO_2 sensitized by PMI−NDI dyad and N719 respectively.[142] The highest efficiency of DSSC tandem cell was kept by Bach and co-workers[151] as much as 2.42 % where oligothiophene−PMI dyad bridge was utilized as NiO sensitizer, leading to a reduced charge recombination. Apart from TiO_2, other n-type photoanodes are also able to be integrated into tandem cells. For example, SnO_2/NiO p-n junction electrode sensitized by N3 dye showed improved performance than bare SnO_2 based DSSC.[173] Although progress has been obtained gradually, the state-of-art tandem DSSC cells are inferior to single TiO2 n-type DSSC. The major breakthrough should be closely related to development of p-type photocathodes.

Table 1-1. Common sensitizers mentioned in content.

Name	Structure	reference
N3	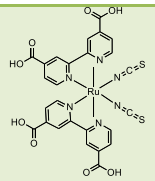	174
N719	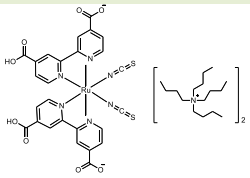	175

Z907	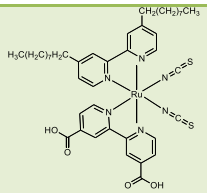	176
RuP	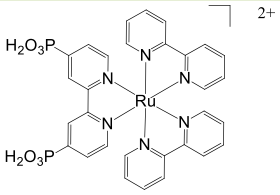	177
C343	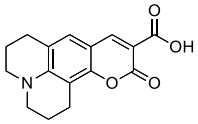	178
P1	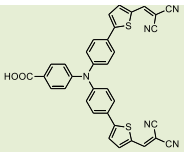	179
P4	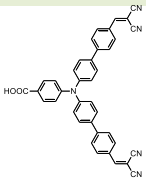	180
P7	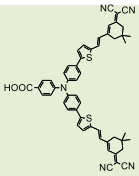	181
Co(dtb-bpy)$_3$	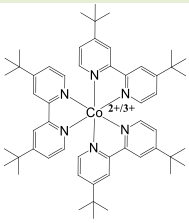	143

NK-2684	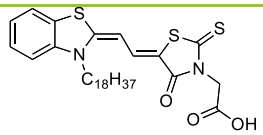	172
PIND	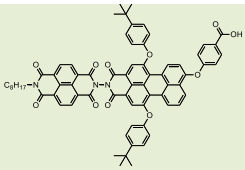	182

1.5 Transparent Conducting Oxides (TCOs)

Transparent conductive oxides (TCOs) based on heavily doped wide band gap metal oxides have gained broad attention in optoelectronic devices and solar cells by taking advantage of their optical transparency and conductivity. [183-186] TCO materials are readily divided into n-type and p-type. n-Type TCO (n-TCO) materials possess defects such as oxygen vacancies, impurity substitutions and interstitials that donate electrons into the conduction band of metal oxides, whereas p-type TCO (p-TCO) materials contain cation vacancies, impurity acceptor and oxygen interstitials that accept electrons thermally promoted from valence band, leaving holes behind. [187] In both cases, the band gap between conduction and valence band remain unchanged from the undoped metal oxides that is the prerequisite to guarantee high optical transparency (> 80 %). Generally speaking, ideal TCO materials have a carrier concentration > 10^{20} cm^{-3}, resistivity < 10^{-3} Ω.cm, mobility > 62.5 cm^2 V^{-1} S^{-1} and a band gap energy > 3 eV. [187] The resistivity ρ, conductivity σ, carrier concentration N, and carrier mobility μ are correlated according to equation 1-2 and 1-3:

$$\frac{1}{\rho} = \sigma = N\mu e \qquad (1\text{-}2)$$

$$\mu = \frac{e\tau}{m^*} \qquad (1\text{-}3)$$

Where e is the electronic charge (1.602×10^{-19} C), τ is the relaxation mean time between collisions, and m* is the effective electron mass. τ and N are intrinsically negatively correlated and cannot be simultaneously increased. An increase in τ might require less carrier densities and fewer defects that contributed from reduced grain boundaries and less neutral impurities. [187]

The actual carrier transport in n type TCOs is proposed to be limited by addition of a series of different independent scattering mechanisms, including grain boundary scattering, ionised impurity scattering, neutral impurity scattering, optical phonon scattering, acoustic-phonon scattering, and piezoelectric scattering. [188-192] Generally, when $N \leq 10^{19}$ cm^{-3}, grain boundary scattering is the dominant mechanism; while $N > 10^{19}$ cm^{-3}, ionised impurities become the primary scattering center.[189,190,192,193] In addition, if mobility is kept the same, the decrease of resistivity is accompanied by the increase of carrier densities. The carrier density has a negative correlation to the ultraviolet (UV) absorption edge of TCO films due to Burstein-Moss effect that is apparent energy band gap enlarges at higher carrier density. But the carrier density is positively corresponded to the position of the infrared (IR) absorption edge. Given that the TCO film transmission particularly in near infrared region (NIR) results from free carrier absorption or by metal-like reflection, it is highly possible that growth of carrier density can harm the transparency of TCO films.[187 194]

Since $CuAlO_2$ has been first prepared as p type transparent conductive films in 1997 by Kawazoe et al., [195] up-to-date a much smaller number of p types TCOs have been investigated than n-type materials. The optical transparency and conductivity of existed p-TCOs are not comparable to current widely used n-TCOs. [196] A possible reason is the large electronegativity of

oxygen leads to strong localization of holes at far low lying oxygen 2p levels than the valence orbitals of metallic atoms. This strong hole localization gives rise to formation of a deep acceptor level. As a result, hole movements in crystal lattice are restricted, leading to poor mobility and high resistivity.[197,198] In light of this hypothesis, chemical modulation of the valence band method was applied to introduce appropriate metal counter cations that reduced strong coulombic force of oxygen ions, freeing the originally localized holes.[198] Therefore, p-TCOs from families of $AgM^{III}O_2$ and $CuM^{III}O_2$ (M^{III} = trivalent cations) have been discovered. [199,200]

Compared to p-TCOs, a large variety of n type TCOs have been investigated in the past, which can be divided into three main groups: doped binary TCOs, ternary TCOs and multicomponent TCOs. [201] The most common n-TCOs are listed in Table 1-2. The lowest conduction band level of metal oxides is normally the spatially spread spherical s orbital of metal that is characteristic of small effective masses and thus large mobility of electrons. As long as high electron concentration is achieved by choosing appropriate dopants, it is easier to discover n type TCOs than p-TCOs. [202]

Doped binary TCOs have been the most widely used TCOs with more than 20 kinds based on several host metal oxides SnO_2, In_2O_3, CdO, or ZnO. [185,201,203] These host metal oxides can be prepared into TCOs possessing high transparency and conductivity without intentional impurity doping owing to intrinsic oxygen vacancies and/or interstitial metal atoms.[201] For example, ZnO thin films have a carrier density at 10^{20} cm^{-3} and resistivity from 10^{-2} to 10^{-4} Ω.cm.[204] Also, SnO_2 TCOs has a charge carrier concentration at 10^{19} to 10^{20} cm^{-3} and resistivity in the range of 10^{-3} to 10^{-2} Ω.cm.[194,205,206] However, undoped TCOs might suffer from instability that limits practical application and incorporation of intentional dopant can greatly reduce their resistivity.[190,204,207]

Table 1-2. Common n-TCO compounds and dopants. Adapted from reference 201 and 21.

Classification	Host material	Dopant or compound
Binary TCO	SnO_2	F, Sb, As, Nb, Ta
	In_2O_3	Sn, Ge, Mo, F, Ti, Zr, Hf, Nb, Ta, W, Te
	ZnO	Al, Ga, B, In, Y, Sc, F, V, Si, Ge,Ti, Zr, Hf, Mg, As, H
	CdO	In, Sn
Ternary TCO	$GaInO_3$	Sn, Ge
	$CdSb_2O_3$	Y
	$MgIn_2O_4$	
	$ZnO–SnO_2$	Zn_2SnO_4, $ZnSnO_3$
	$ZnO–In_2O_3$	$Zn_2In_2O_5$, $Zn_3In_2O_6$
	$In_2O_3– SnO_2$	$In_4Sn_3O_{12}$
	$CdO–SnO_2$	Cd_2SnO_4, $CdSnO_3$
	$CdO–In_2O_3$	$CdIn_2O_4$
multicomponent TCOs	$ZnO– In_2O_3– SnO_2$	$Zn_2In_2O_5–In_4Sn_3O_{12}$
	$ZnO–CdO– In_2O_3– SnO_2$	

Based on the known host binary metal oxides, ternary TCOs have lately been explored, such as Zn_2SnO_4, $In_4Sn_3O_{12}$, $CdSnO_4$, $Zn_2In_2O_5$, and $GaInO_3$, by referring to multi-dimensional phase diagram of host binary materials. [203,208,209 210] However, ternary TCOs have yet to be widely investigated practically as effective dopants are still lacking.[201]

Additionally, new trend has been discovery of multicomponent TCOs that combine binary and/or ternary TCO films. As-obtained TCOs attain specialized applications by controlling the chemical composition of multicomponent oxides, which in turn brings about desired physical property change. [211] As example, ZnO–In_2O_3 and $MgIn_2O_4$-$Zn_2In_2O_5$ have shown enhanced thermal stability of resistivity than undoped ZnO, In_2O_3, and $MgIn_2O_4$ under oxygen atmosphere. [211-213]

1.6 Antimony-doped tin oxides (ATOs)

Amongst n-TCOs, tin doped indium oxide (ITO) has so far been the most preferential conductive material with 10^{-4} ~10^{-5} Ω cm resistivity commercially available. Demands for finding alternatives to ITO have substantially increased owing to the high cost and rarity of indium metal. [214] Aluminum doped znic oxide (AZO), Gallium doped zinc oxide (GZO) and In-doped CdO can reach a resistivity at the order of 1×10^{-5} Ω cm by suitable deposition technique.[201,215,216] Considering the environmental toxicity of cadmium, TCOs based on CdO did not have practical use. Impurity doped znic oxide are promising candidates as alternatives to ITO in light of their non-toxic and cheap metal source. The current problems for AZO or GZO arise from complicated deposition techniques and difficulty to develop target on large surface scale. Apart from the above-mentioned effective dopants by metallic ions, donor level can also be successfully formed by incorporation of non-metallic ions. Fluorine doped tin oxide (FTO) has gained much attention recently, especially in non-silicon solar cells. The O^{2-} ion is replaced with

a F^- ion, bringing about increased electron concentration and mobility. [190,217] The transparency and conductivity of FTO are normally inferior to ITO and AZO electrodes.[190,194,207]

Antimony-doped tin oxide (ATO) has also been a well-known TCO material owing to the cheap cost, abundance of antimony, and good thermal stability.[185] Its conductivity originated from oxygen vacancies and substitution of Sn^{4+} with nonmetallic Sb^{5+} cation, with one more electron donating to the conduction band of tin oxide. [190] Antimony dopants give rise to a donor level at 35 meV.[185] The dopants form a donor level below conduction band edge, leading to a blue shift of optical absorption edge (Burstein-Moss effect), requiring higher energy for an electron promoted from valence band to conduction band. The free electron carriers also lead to NIR-IR absorption and reflection well explained by Drude theory, in which the onset of NIR is calculated by plasma frequency that is dependent on the carrier concentration and mean free path of carriers. [218] Therefore, with low dopant concentration, the onset of NIR locates at NIR region and TCOs are transparent within the visible spectrum. With high dopant concentration, NIR onset shifts into red region, leaving TCO with bluish color. [219-221]

It has been found that different antimony oxidation states coexist inside ATO films, Sb^{5+}, an electron donor, and Sb^{3+}, an electron acceptor. The net excess of Sb^{5+} over Sb^{3+} gives rise to the conductivity of ATO films. In addition, extremely high concentration (Sb/Sn=0.38) of antimony dopant might cause blackening of ATO film due to electron transfer between the two Sb oxidation states.[222]

The resistivity of ATO films largely depends on antimony doping ratio and ATO particle size. A typical ATO dense film has a charge carrier concentration of 10^{20} cm^{-3}, a mobility of 10 - 30 cm^2 V^{-1} S^{-1} and resistivity of 10^{-3} Ω.cm with transmittance ~ 80-90 %. [185] At low doping

concentration, Sb^{5+} is the predominant dopant.[223] When doping concentration is greater than

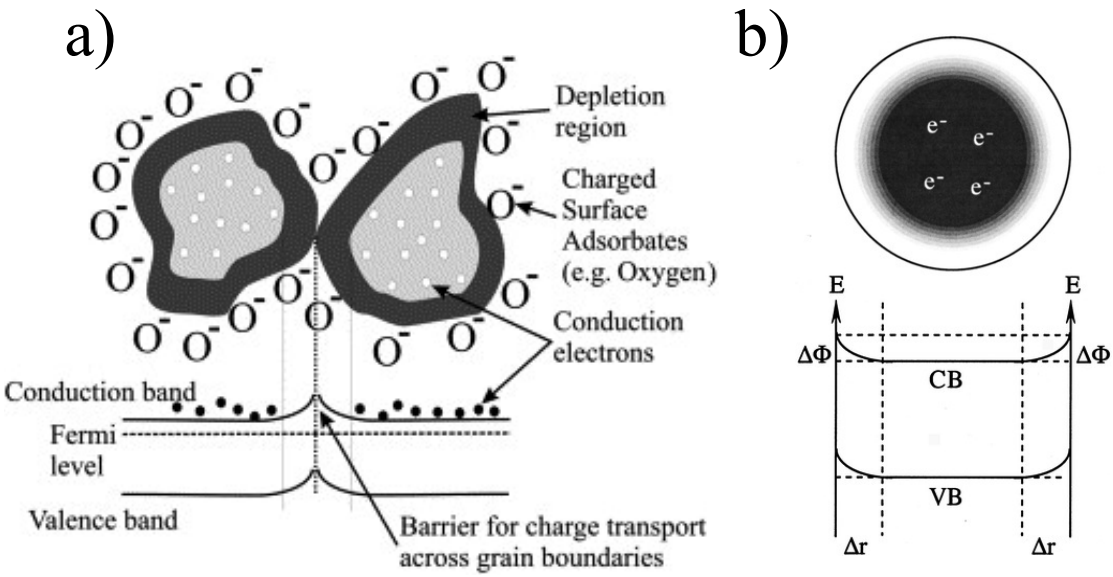

Figure 1-3. a): Charge carrier concentration distribution in SnO_2 grains. Negative surface charges lead to an upward band bending and consequently a depletion layer, causing a Schottky-like barrier across grain boundaries. Adapted from reference 194. b): Upper part: conduction-band electron concentration in a highly n-doped semiconductor nanoparticle under depletion condition. Lower part: band bending and energy diagram of n type TCO nanoparticle. Adapted from reference 224.

4 %, Sb^{3+} can enter the lattice, accompanied by a decrease in conductivity.[221] A thermal annealing treatment might cause reoxidation of Sb^{3+} to Sb^{5+} state.[221] The highest conductivity values for bulk ATO materials were achieved from 2 % to 7 % doping ratios according to preparation technique. Heavily doped ATO has a smaller size than lightly doped films.[218,222]

In case of ATO films made of small nanoparticles, the grain sizes also greatly influence resistivity. Ionised impurity scattering has been a main scatter mechanism in many TCOs and it also limits of resistivity for ATO films. More importantly, scattering at grain boundaries arising

from an electron depletion layer, in particular, plays a role in further decreasing conductivity for ATO nanomaterials. [203,217,220,225] Geraldo et al. has found that doped ATO film made of 3-5 nm nanoparticles indicated low conductivity even with a high free electron concentration of 4-5 $\times 10^{20}$ cm^{-3} as predicated by Drude's model. They ascribed the small conductivity to the intense grain boundary scattering and low mobility. [218] This could be further proved by Nütz et al. who reported a resistivity of 10 Ω.cm of ATO pellet made from 4-9 nm nanoparticles, a value of 4 orders of magnitude higher than bulk ATO even after high temperature treatment. [220]

This grain boundary effects for ATO films could be understood in Figure 1-3. [194,224] Negative surface charges (e.g. caused by chemisorbed oxygen in a) or by n type metal oxide / electrolyte interface in b)) bend conduction band of n- TCO upward, causing a decrease of the charge carrier concentration and formation of an electron depletion layer with positive space charge region. Thus conduction band electrons have to overcome energy barrier caused by space charge electric field across the grain boundary. In consequence, the conductivity will rely on the charge carrier depletion zone.[194] For samples with dimensions comparable to that of space charge depletion layer, a particular strong change in the conductance may be expected.[224,225]

1.7 Soft chemical synthesis for metal oxide nanoparticle

Preparation of nanomaterials at < 100 nm scale has been particularly attractive for metal oxides research with significant applications in solid-state-chemistry, electroceramics, catalysis, energy storage and conversion. [226,227] Both physical and chemical methods have successfully prepared nanomaterials. [228,229] Physical methods, such as spray pyrolysis and ball milling, are normally inferior to chemical method owing to the difficulty for size and morphology control.

In the field of chemical synthesis, traditional aqueous sol-gel procedure has long been the dominant technique that transfers molecular metal precursors into metal oxides. Sol refers to a

dispersion of colloidal particles in liquid and the latter means solid particles of 1-100 nm size. Gel represents an interconnected, rigid, and porous inorganic network by polymeric chain enclosing a continuous liquid phase. [230] It is worthy to notice that sol-gel procedure sometimes follow simple precipitation instead of formation of a sol and gel. [226,230] Usually, the metal oxide starting compounds could either be inorganic salt such as nitrates, chlorides, acetates, or be organic species such as metal alkoxides which is widely adopted in sol-gel reaction. On the other hand, aqueous sol-gel route suffers from major disadvantages including time consuming process, requirement of post heat to induce crystallization, difficulty of control synthesis parameters due to the complexity of aqueous environment.[226]

A typical aqueous sol gel route involves two main steps: hydrolysis and condensation as described in equations1-4 to 1-6, in which —OR is the alkoxide group, —M is metal, and —OH is he hydroxide group. [231,232]

Hydrolysis for formation of reactive M-OH:

$$\equiv M - OR + H_2O \rightarrow \equiv M - OH + ROH \qquad (1\text{-}4)$$

Condensation to form metal-oxygen-metal bridge:

$$\equiv M - OR + HO - M \rightarrow \equiv M - O - M \equiv + H_2O \qquad (1\text{-}5)$$

or

$$\equiv M - OR + HO - M \rightarrow \equiv M - O - M \equiv + R - OH \qquad (1\text{-}6)$$

In the hydrolysis step, nucleophilic attack of the oxygen atom from water leads to formation of metal hydroxide and alcohol release. In the sequential step, condensation reaction produces metal-oxygen-metal bonds between two metal hydroxides or one metal alkoxide and metal hydroxide, forming either water or alcohol as in situ byproducts. This simultaneous

occurrence of condensation step gives rise to a large number of different species hard to identify.[233] Therefore, aqueous sol-gel route is hard to control.

Another main drawback of the aqueous sol-gel synthesis is fast reaction rate for most metal oxide precursors, resulting in a loss of morphological and structural control over the final oxide material. [226] One way is to increase molecular complexity of a given metal alkoxide precursors that might reduce the chemical reactivity.[229] For example, titanium butoxide is less reactive than titanium propoxide. Another way is to introduce chelating organic additives such as carboxylic acids, acetylacetone, or functional alcohols by substitution of the alkoxide group, decreasing the hydrolysis rate. [229,233-235] In addition, slow release of water by chemical or physical process and thus control over local water concentration can effectively control metal precursor hydrolysis rate.[236-238]

Under the consideration of decreasing sol-gel hydrolysis and condensation rate, non-aqueous sol-gel route by avoiding the presence of water has been developed, even though hydrated metal oxide precursors and in situ product of water might be incorporated. [229,236,239-241] The nucleophilic attack to metal precursor is then not from oxygen of water but from ethers, alcohols, or alkoxide. The reaction rate is then determined by the oxygen carbon bond.[240,242,243] Consequently, non-aqueous sol gel route has gained growing interests by taking advantage of high crystallinity at low temperatures, robust synthesis parameters and ease control of crystal growth.[226,239]

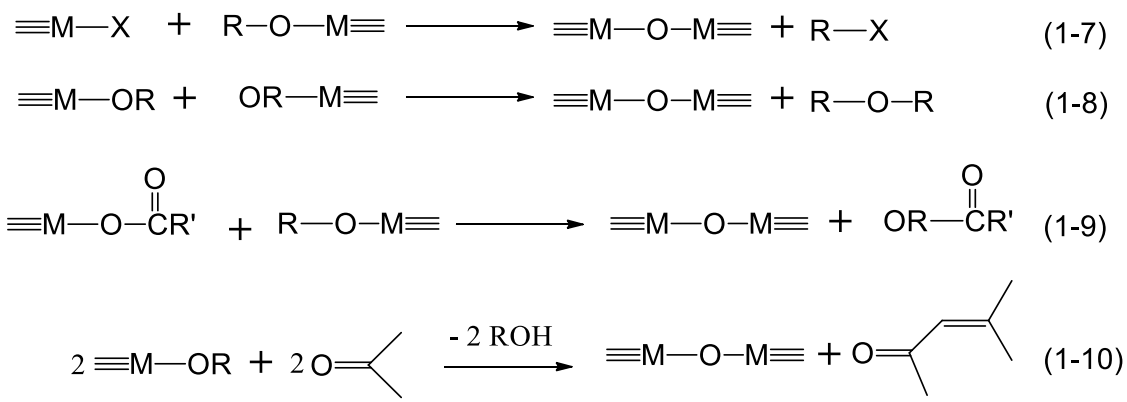

The condensation steps in non-aqueous route are summarized in equation 1-7 to 1-10. Equation 1-7 displays the metal halide and metal alkoxide condensation. Equation 1-8 shows ether elimination by condensation of two metal alkoxides. Equation 1-9 involves ester elimination between metal carboxylates and metal alkoxides. Equation 1-10 indicates aldol condensation with the ketones as solvents. [239]

Benzyl alcohol serves as a good solvent for non-aqueous synthesis in that it can react with a variety of metal precursors such as metal alkoxides, halides, acetylacetonates or acetates to prepare assorted metal oxides.[244-246] Benzyl alcohol is considered to be more reactive than aliphatic alcohol. A C-C bond formation mechanism is proposed to control condensation step.[247] For instance, Niederberger et al. has found a C-C bond formation between the isopropoxy ligand of titanium isopropoxide and benzyl alcohol when preparing $BaTiO_3$ nanomaterials. In consequence, as obtained Ti-OH group further induces metal oxide under release of 4-phenyl-2-butanol, shown in Figure 1-4.[239,242,247] Another possibility for benzyl alcohol assisted route is from the perspective of a S_N1 reaction, especially in the presence of metal chlorides precursors displayed in Figure 1-5. [246] Benzyl alcohol has a largely delocalized benzyl carbocation due to the benzene ring. Hu et al. have confirmed the generation of benzyl chloride and benzyl ether for metal-oxygen-metal condensation in a series of benzyl alcohol and metal chloride reactions. The

readily-formed benzyl carbocation in benzyloxy group is attacked and later substituted by nucleophilic agent (chloride ions, benzyloxy group et al.)

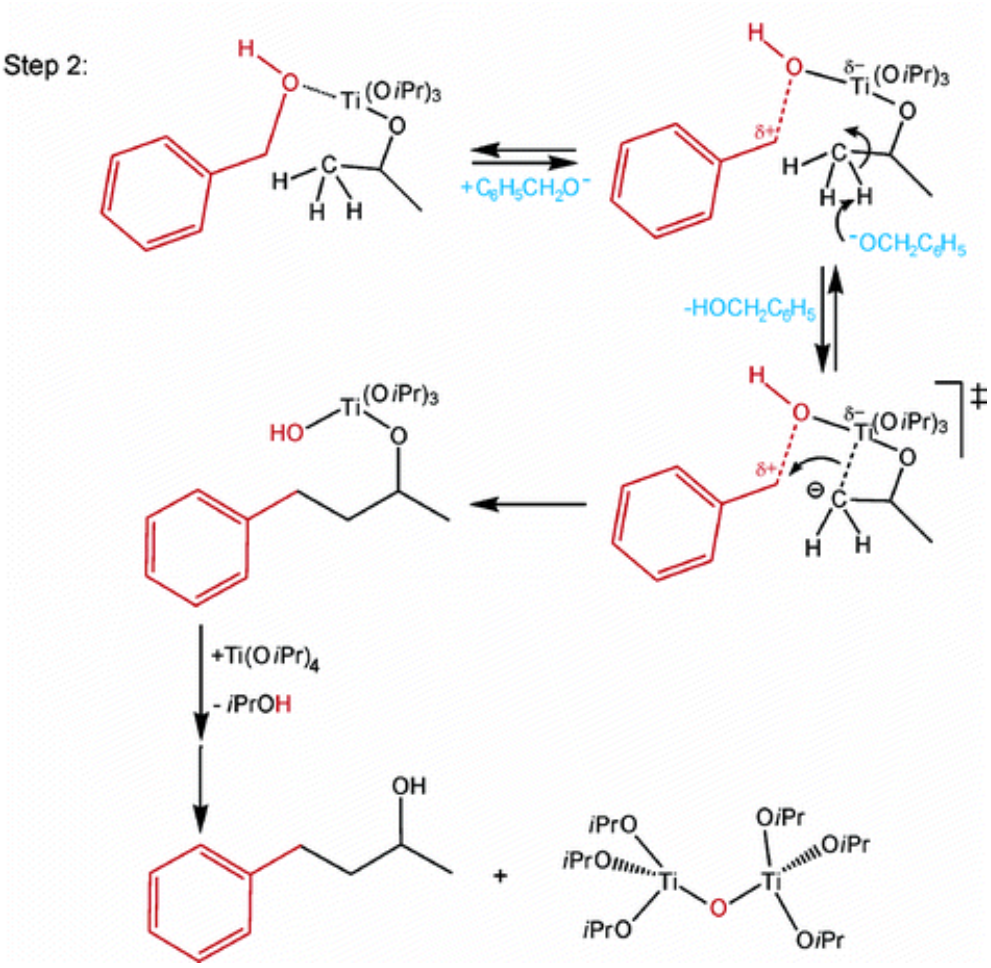

Figure 1-4. Proposed mechanism for a C–C bond formation for the simultaneous generation of $BaTiO_3$ nanoparticles and 4-phenyl-2-butanol. Adapted from reference 226 and 239.

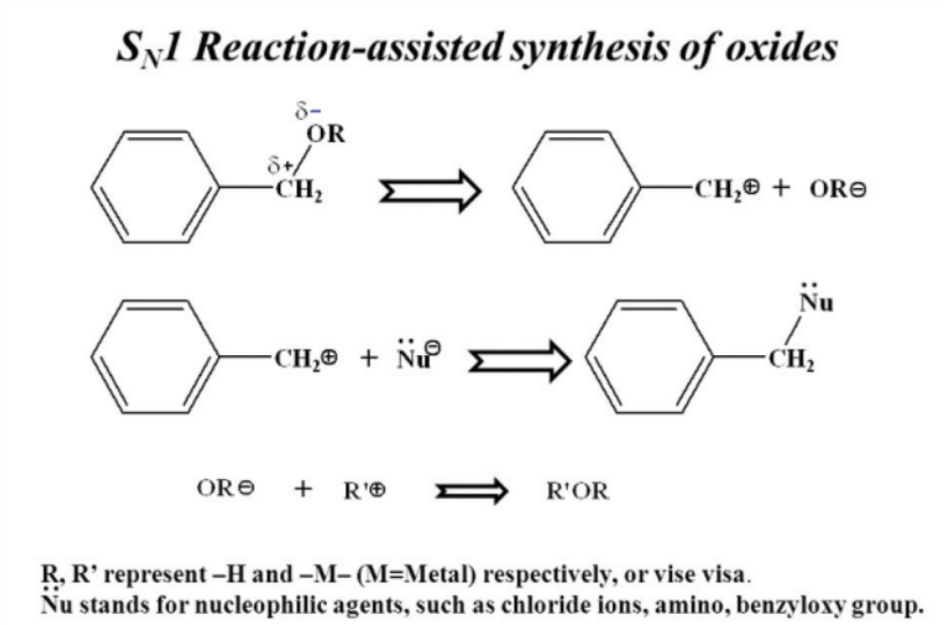

Figure 1-5. Proposed SN1 reaction mechanism in the reactions of benzyl alcohol and metal chlorides for the synthesis of metal oxide nanoparticles. Adapted from reference 246.

1.8 Nanocrystal synthesis by microwave irradiation

By far heating chemical transformations on a laboratory scale has largely based on heating mantles, oil baths, and hot plates with the help of a reflux set-up. Therefore, the upper limit for reaction temperature highly depends on the boiling point of the solvent. A main drawback of this traditional form of heating lies in a slow and inefficient energy transfer to a reaction mixture, a process that is limited by convective currents an thermal conductivity of the various materials that have to be penetrated, leading to inhomogeneous temperature of the reaction vessel and the reaction solution.[248,249] In contrast, microwave irradiation gives rise to efficient uniform temperature growth by direct coupling of microwave energy to the molecules that are present in the reaction mixture.[248]

Two main mechanisms are involved in the microwave reaction. The first one is by dipolar polarization in which dipoles inside reaction medium align with the electric field and

reorganize themselves as electric filed oscillates with an applied microwave frequencies. The amount of heat generated by molecular friction or dielectric loss greatly depends on the ability of the dipoles to align with electric field. Commercially available microwave systems typically use 2.45 GHz that allows dipoles have enough time to realign but not to reorient too fast with applied field.[250,251] Another mechanism, ionic conduction, employs charged particles or ions that oscillate back and forth according to microwave field, generating heat by collisions. The latter mechanism produces heat more efficiently than dipolar effect. In general, the capability of material to convert microwave energy to heat is described by loss tangent (tan σ) that is determined by dielectric loss and dielectric constant. [252] A high value of tan σ (> 0.5) is required for appropriate reaction solvents under 2.45 GHz.

Microwave route substantially accelerates reaction rate which is proposed to mainly originate from aforementioned thermal/kinetic effect that is high temperature can be fast reached under microwave irradiation. However, "specific microwave effect" defined as "rate acceleration cannot be achieved or duplicated by conventional heating, but are essentially still thermal effects" must be taken into accounts. [253] Those specific microwave effects includes "superheating" effect of solvents at atmospheric pressure, selective heating of strongly microwave absorbing heterogeneous catalysts in a comparatively less polar reaction medium and the disappearance of wall effects caused by inverted temperature gradients.[252,253] There have been a lot of debates and uncertainties in rationalizing microwave effects in chemical synthesis.

In a typical nanocrystal sol-gel synthesis, once molecular precursor initiates hydrolysis or alcolysis, a large number of highly reactive intermediates (monomers) induce nucleation after supersaturation threshold is passed. Secondary precipitation like Ostwald ripening might exist, promoting the formation of big particles at the expense of small nanoparticles. [229,254] Since

microwave reactions are normally one-pot, single step in practical, the given amount of precursors will govern the final nanoparticle size. High nuclei concentration rapidly formed at the beginning leads to a small number of monomers left to feed nuclei center, thereby small nanoparticles are obtained.

Numerous nanoparticles have been prepared by microwave assisted synthesis such as single metal catalysts, core shell nanoparticles, and nanostructured metal oxides.[248] A combination of microwave reaction and non-aqueous sol-gel route has proven to be simple, time efficient, size controllable. [255,256] Benzyl alcohol has been a suitable solvent for microwave procedure due to a high boiling point and high dielectric loss factor. Thus, benzyl alcohol assisted non-aqueous route has successfully prepared versatile nanomaterials, including ZnO, $BaTiO_3$, CoO, MnO, $NiFe_2O_4$, and Mn_3O_4. [244,256-258] Moreover, this route offers an efficient pathway to obtain doped nanomaterials.[248] ITO nanoparticles were attained by a two-step polyol method under microwave irradiation at 200 °C with a pellet resistivity of 1.9×10^{-2} Ω cm.[259] AZO (Al:ZnO) and Sn:ZnO nanoparticles with different doping ratio were synthesized in the presence of benzyl alcohol and microwave irradiation, and further processed into transparent conductive electrodes. [260,261]

1.9 Mesoporous nanomaterials

Ordered porous materials have periodically aligned 2-(2D) or 3-dimensional (3D) pore structures. They can be classified into three types based on International Union of Pure and Applied Chemistry (IUPAC) nomenclature according to their pore diameters (d): microporous ($d < 2$ nm), mesoporous ($2 \text{ nm} < d < 50$ nm), and macroporous ($d > 50$ nm).[262] Numerous methods in ordered mesoporous materials originate from the pursuit of large porous crystalline frameworks for heavy oil conversion and traditional zeolite and molecular sieves with

micropores in 1990s.[263,264] Even though mesoporous silica has been intensively studied, preparation for non-silica mesoporous structures is still challenging due to the difficulty in controlling non-silica precursor hydrolysis and condensation during the sol-gel process. Mesoporous metal oxides, in particular, have gained much attention as they exhibit a variety of applications, such as adsorption, separation, catalysis, drug delivery, and energy conversion and storage.[265-270]

Synthesis for mesoporous materials generally is based on templating methodology that is divided into two kinds: soft templates and hard templates. The soft templates are normally surfactant like molecules such as cetyltrimethylammonium bromide (CTAB), and amphiphilic block copolymers like Pluronic P123 (poly (ethylene oxide- propylene oxide − ethylene oxide), PEO-PPO-PEO, $EO_{20}PO_{70}EO_{20}$).[264,265,271] The hard templates usually produce material with rigid framework like silica, carbon, and colloidal crystals.[272,273] The requirement of tedious fabrication and thin pore wall thicknesses for hard templating prevent it from practical use at large scale. On the contrary, soft templating is versatile for its high efficiency and good shape and size control during the synthesis.[271]

There are generally four routes to obtain mesoporous metal oxides from metal precursors: direct precipitation; true liquid crystal templating; Evaporation induced self-assembly (EISA) and exotemplating, as demonstrated in Figure 1-6.[263,274] Direct precipitation is based on the cooperative assembly of the metal precursors and the supramolecular template that occurs via hydrolysis and condensation of the inorganic species. True liquid crystal templating involves

nonionic surfactant forming a liquid mesophase, followed by infiltration with metal precursor.

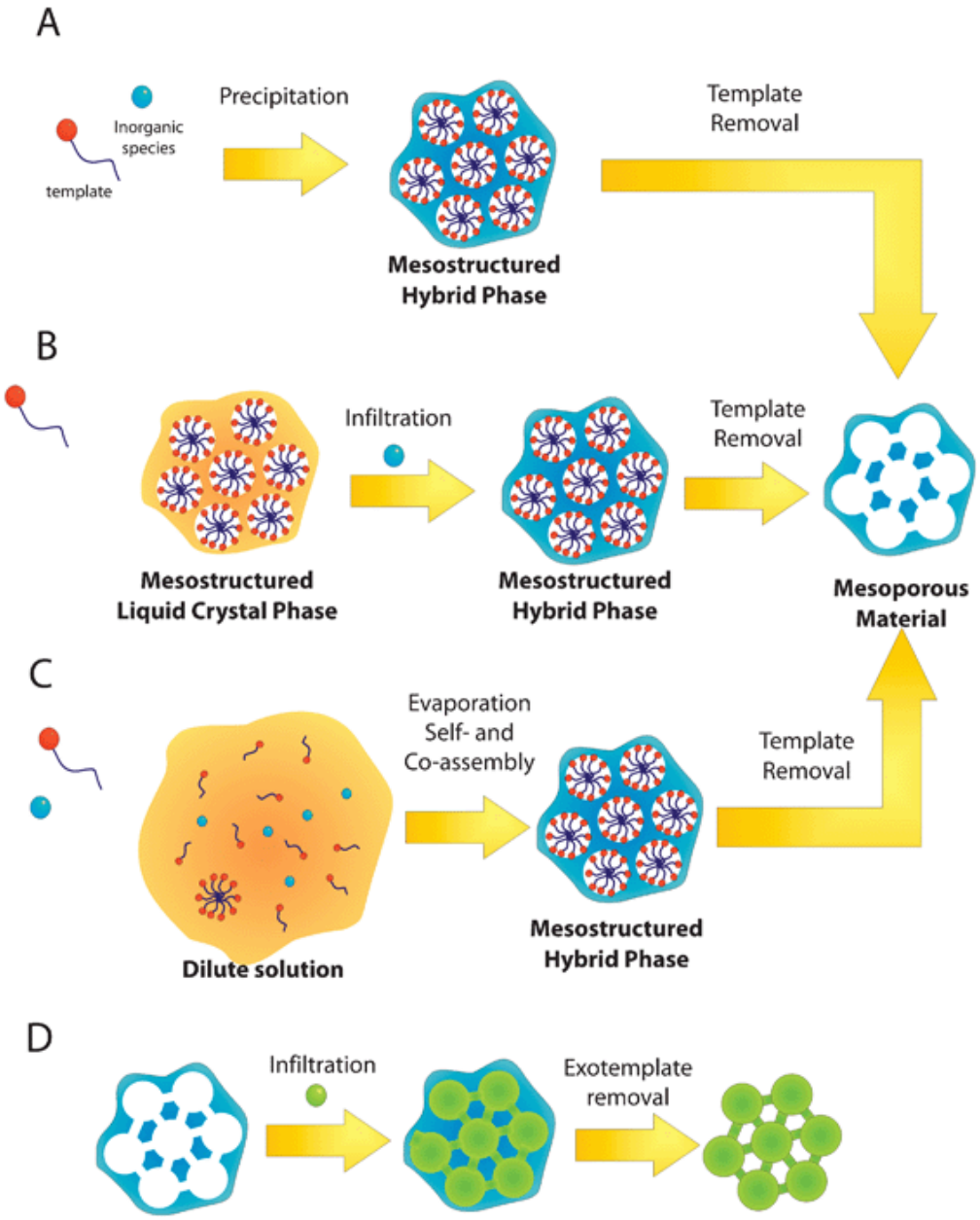

Figure 1-6. Scheme of the main synthesis routes to mesoporous materials from metal precursors: precipitation (A), True Liquid Crystal Templating (B), Evaporation-Induced Self-Assembly (C) and Exotemplating (D). Adapted from reference 274.

EISA is the most used synthetic strategy for mesoporous structures, including an initially dilute and homogenous mixture of metal precursor, templating agent and other additives, the solvent of which is then evaporated by dip or spin coating, inducing micelle formation and cooperative self-assembly between templates and metal-precursors driven by phase segregation. By employing a subsequent heating or adding condensation enhancer, the organic/inorganic hybrid starts to condensate and remove templates. Exotemplating or hard templating relies on two steps: fabricating a previously formed mesoporous matrix template; removing this template, leaving a mesoporous structure "negative" of the exotemplate.

Since aforementioned routes prepare mesoporous structure directly from metal precursors, the obtained organic/inorganic composites are normally amorphous and require a post annealing at elevated temperatures to increase crystallinity, often giving rise to collapse of the original mesostructure. To overcome this problem, strategies based on presynthesized well-defined nanobuilding blocks (NBBs) are developed, the mesoporous structure is attained by self-assembly of NBBs directly or by templating agents. [275] These NBBs should be at least 4 times smaller than the micelles so as to adopt the curvature (2-30 nm in size) of the organic template interface. [276]

A general NBB assisted route includes four steps: formation of well-defined metal oxide nanocrystals; mixing of the nanocrystal and templating agents; cooperative assembly of nanocrystals into mesoporous hybrid and remove the template by calcination.[277]

1.9.1 3-dimentional mesoporous metal oxides templated by amphiphilic polymers

Up to now, soft templates to synthesize mesoporous structures employ assorted cationic, nonionic and anionic surfactants, which usually refer to low-molecular weight amphiphilic

molecules with small hydrophilic heads and hydrophobic tails. As obtained mesoporous materials possess small mesopores less than 10 nm arising from short hydrophobic chains.[265]

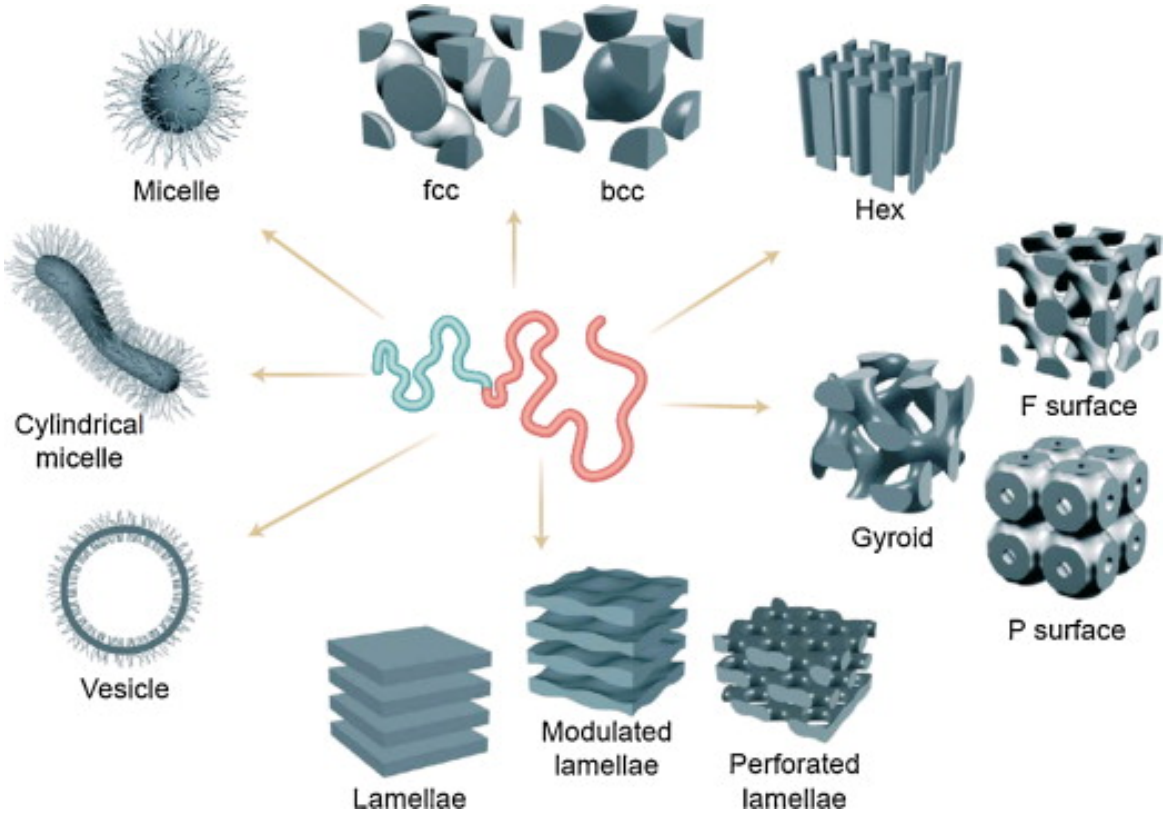

Figure 1-7. Various mesophases diagram of block copolymers templates, including spherical and cylindrical micelles, vesicles, spheres with face-centered cubic, and body-centered cubic, hexagonally packed cylinders, bicontinuous gyroid, F surface, P surfaces, and lamella. Adapted from reference 278.

In order to explore large-pore mesoporous materials, amphiphilic block copolymer was first discovered by Zhao et al. to prepare mesoporous silica.[279] This opened a door to large-pore mesoporous materials by using polymer as structure directing agents especially for applications in catalysis, adsorption, and sensors that benefit from large open voids and high surface area. This breakthrough is ascribed to the microphase separation property in block copolymers that

consist of two or more chemically distinct homopolymer subunits covalently linked, self-assembly into widely-tunable structures by adjusting concentration, shown in Figure 1-7.[278,280,281] Thermodynamic incompatibility of blocks originates from small entropy of mixing per unit volume and an inverse correlation between entropy of mixing and molecular weight. [270,282] The coexistence of long range repulsion (e.g. excluded volume, phase separation) and short range attraction (e.g. covalent bond, minimum space required, electroneutrality) between different building blocks drives copolymers to form ordered structures.[282] The final morphology results from bulk microphase separation can be theoretically predicted by block length ratio and segregation parameter obtained from Flory–Huggins interaction parameter.[283]

3-dimentional mesoporous metal oxide electrodes have found substantial utilizations in catalysis, solar cells and energy storage. The mesoporous framework provides a 3D pathway for minimized diffusion of ions and electrons. The porous structure allows high surface area exposed to electroactive species. [284] Despite of merits for 3D mesoporous metal oxides, their synthesis strategies remain challenging in comparison to silicate porous materials. As mentioned previously, metal oxide precursors often show much faster rate for hydrolysis and condensation during sol-gel synthesis than silicate mesoporous materials. Additionally, requirement of high crystallinity for metal oxide films easily lead to collapse of mesoporous structures.[265]

Pluronic family, based on triblock copolymer PEO-PPO-PEO such as P123, F127, F108, belongs to the most widely utilized block copolymer in mesoporous metal oxides.[285,286] In 2005, a DSSC solar efficiency of 4.04 % was reported by P123 templated TiO_2 film grown layer by layer, which was 50 % efficiency enhancement from traditional films of the same thickness. [287] State-of-art solar efficiency for a NiO/p-type DSSC cell was obtained by F108 templating.[288] However, pluronic copolymers also suffer from small PPO subunits that are unfavorable to pore

size > 12 nm and wall thickness < 6 nm.[265,289] Moreover, due to the weak thermo-stability of pluronic copolymers, it is difficulty to produce ordered mesoporous crystalline metal oxide as the decompose at relatively low temperatures 200-350 °C whereas metal oxide crystallinity normally require 400-600 °C.[289]

By contrast, non-pluronic copolymers often contain lower oxygen and higher carbon content, higher glass transition temperature, and better thermostability. Nedelcu et al. first fabricated TiO_2 film by templating from poly(isoprene-b-ethyleneoxide) (PI-b-PEO) block copolymers in solid state DSSCs with the 2,2′7,7′-tetrakis-(N,N-di-p-methoxyphenyl-amine)-9,9′-spirobifluorene (spiro-MeOTAD) as hole collection medium.[290] The TiO_2 morphology was controllable on the 10 nm length scale with pore sizes ranging from 20 to 80 nm. More recently, an upgraded PI-b-PEO templated solid state TiO_2/DSSC device was reported with an efficiency of 4 %.[291] Poly(4-fluorostyrene-block-D,L-lactide) (PFS-b-PLA) was later discovered to build TiO_2 mesoporous films for DSSCs.[292,293] PFS-b-PLA copolymer self-assembled into a double bi-continuous interwoven gyroid phase. After selectively removing PLA component, titanium oxides were electrochemically deposited into previous gyroid voids, forming continuous anatase network with pores after calcinations. As prepared solid state DSSC of 400 nm thickness reached up to 1.7 % power conversion efficiency. The gyroid structure was found to outperform quasi-1D nanowire and randomly-oriented system in liquid DSSC system. Sponge-like TiO_2 nanostructures have been prepared directed by poly(styrene-block-ethylene oxide) (PS-b-PEO) by addition of TiO_2 by HCl treatment of titanium tetraisopropoxide. [294] There are still a couple of common PEO-rich copolymer templates, including poly(butadiene -b-ethyleneoxide)(PEO-PB),[295] poly(isobutylene-b-ethyleneoxide)(PIB-b-PEO),[296,297] poly(methyl acrylate-b-ethyleneoxide)(PMA-PEO),[298] poly(ethylene-co-butylene-b- ethyleneoxide) (PHB-PEO referred

to also as "KLE"),[299-302] and poly(ethyleneoxide-b-butadiene-b-PEO (PEO-PB-PEO).[303] Besides TiO_2, other mesoporous metal oxides with improved performance have been synthesized templated by copolymers, such as IrO_2, SnO_2, ZrO_2, Nb_2O_5.[265,296,304]

Grafted copolymers as metal oxide film templating agents have recently been proposed by Kim group.[305-307] This new type of copolymer, poly (vinyl chloride)-g-poly (oxyethylene methacrylate) (PVC-g-POEM), is advantageous in low cost and ease of synthesis. The technique has been applied to micron-thick TiO_2 films in a one-pot process rather than by the more tedious layer-by-layer deposition that is usually required. A solid state TiO_2 DSSC templated by a grafted copolymerization with the N719 dye gave an impressive solar conversion efficiency of 7.1 % under 100 mW illumination demonstrating real promise for grafted copolymers as directing agents for metal oxide films.[308]

Homopolymers have also been used to tune the size and morphology of nanostructures.[309,310] Polystyrene added to PS-b-PEO copolymer was used to template a titania sol which resulted in a morphological transition to thinner and smaller TiO_2 nanostructures.[310] Homopolymers can directly lead to templating. Inverse opal films of TiO_2 prepared by monodispersed polystyrene spheres have been reported. [311] This procedure was used to prepare a 10 μm TiO_2 photoanode with an efficiency of 4.2 % based on a N719-sensitized DSSC.

1.9.2 **3D mesoporous ATO electrodes**

Transparent conducting oxides (TCOs) have successfully been utilized in a wide range of optoelectronic and photoelectrochemical devices.[183,184] In comparison to flat TCOs, 3-dimentional mesoporous nanostructured TCOs (2 nm <pore diameter < 50 nm) are characteristic of high interfacial area exposed to electroactive species and fast drift electron transport rather

than diffusive transport in traditional metal oxide semiconductors like TiO_2.[312,313] These properties bring mesoporous TCO electrodes with broad applications such as dye sensitized solar cells (DSSCs), electrochemical catalysis, and biochemical sensors.[314-318] Despite that Sn-doped In_2O_3 (ITO) has been the most popular TCO material, demands for finding alternatives to it have substantially increased due to the high cost and rarity of indium metal.[214] Antimony-doped tin oxide (ATO) is a promising alternative to ITO since it has high transparency with a large band gap (> 3.6 eV) and good electric conductivity.[185] Therefore, strategies toward 3-D mesoporous nanostructured ATO films are highly desirable.

The most used synthetic route to obtain 3-D mesoporous ATO is based on inorganic metal precursors soft templated by organic surfactant molecules and amphiphilic copolymers through evaporation induced self-assembly (EISA).[264,265,271] In order to explore large-pore mesoporous materials, amphiphilic copolymers are chosen to structurally direct mesoporous metal oxide formation, driven by microphase separation of copolymers containing thermodynamically incompatible subunits. [278,280]

In spite of the elegance of this approach, it suffers from several limitations. Complications associated with mixed Sn and Sb precursors that often show fast rate for hydrolysis and condensation, making it difficult to control interaction with organic copolymers.[316] In addition, as obtained mesoporous structures are usually amorphous and thus require post annealing at elevated temperature to increase crystallinity, leading to a strain induced collapse of the original mesopores. [265] It apparently limits the choices of structure directing polymers for mesoporous ATO films to poly(ethylene-co-butylene)-b-poly(ethylene oxide) KLE copolymer, polyisobutylene-b-poly(ethylene oxide) copolymer, and pluronic block copolymer F127.[296,316] To overcome these weaknesses, mesoporous materials based on

presynthesized well-defined ATO nanocrystals was proposed, which also allows a fine tune of doping level of metal oxides. Müller et al. have attained mesoporous ATO films with presynthesized small ATO nanoparticles soft templated by F127 copolymer.[319] However, pluronic copolymers normally decompose at relatively low temperatures compared with high temperatures to maintain high crystallinity of metal oxides. [265,289] Therefore, it is highly demanded to explore non-pluronic copolymers with lower oxygen and higher carbon content, higher glass transition temperature, and better thermostability in the synthesis of mesoporous ATO electrodes.

1.10 REFERENCES

(1) Tsubomura, H.; Matsumura, M.; Nomura, Y.; Amamiya, T. *Nature* **1976**, *261*, 402.

(2) D. Duonghong, N. S., M. Grätzel *Helv. Chim. Acta* **1984**, *67*, 1012.

(3) Michael, G. *Journal of Photochemistry and Photobiology C: Photochemistry Reviews* **2003**, *4*, 145.

(4) Desilvestro, J.; Graetzel, M.; Kavan, L.; Moser, J.; Augustynski, J. *J. Am. Chem. Soc.* **1985**, *107*, 2988.

(5) O'Regan, B.; Gratzel, M. *Nature* **1991**, *353*, 737.

(6) Jose, R.; Thavasi, V.; Ramakrishna, S. *J. Am. Ceram. Soc.* **2009**, *92*, 289.

(7) Yella, A.; Lee, H.-W.; Tsao, H. N.; Yi, C.; Chandiran, A. K.; Nazeeruddin, M. K.; Diau, E. W.-G.; Yeh, C.-Y.; Zakeeruddin, S. M.; Grätzel, M. *Science* **2011**, *334*, 629.

(8) Gratzel, M. *Nature* **2001**, *414*, 338.

(9) Hamann, T. W.; Jensen, R. A.; Martinson, A. B. F.; Van Ryswyk, H.; Hupp, J. T. *Energy & Environmental Science* **2008**, *1*, 66.

(10) Martinson, A. B. F.; Hamann, T. W.; Pellin, M. J.; Hupp, J. T. *Chemistry – A European Journal* **2008**, *14*, 4458.

(11) Solbrand, A.; Keis, K.; Södergren, S.; Lindström, H.; Lindquist, S.-E.; Hagfeldt, A. *Sol. Energy Mater. Sol. Cells* **2000**, *60*, 181.

(12) Cahen, D.; Hodes, G.; Grätzel, M.; Guillemoles, J. F.; Riess, I. *J. Phys. Chem. B* **2000**, *104*, 2053.

(13) Kopidakis, N.; Schiff, E. A.; Park, N. G.; van de Lagemaat, J.; Frank, A. J. *J. Phys. Chem. B* **2000**, *104*, 3930.

(14) Hochbaum, A. I.; Yang, P. *Chem. Rev.* **2009**, *110*, 527.

(15) Péchy, P.; Renouard, T.; Zakeeruddin, S. M.; Humphry-Baker, R.; Comte, P.; Liska, P.; Cevey, L.; Costa, E.; Shklover, V.; Spiccia, L.; Deacon, G. B.; Bignozzi, C. A.; Grätzel, M. *J. Am. Chem. Soc.* **2001**, *123*, 1613.

(16) Nakade, S.; Matsuda, M.; Kambe, S.; Saito, Y.; Kitamura, T.; Sakata, T.; Wada, Y.; Mori, H.; Yanagida, S. *J. Phys. Chem. B* **2002**, *106*, 10004.

(17) Wang, P.; Zakeeruddin, S. M.; Moser, J. E.; Nazeeruddin, M. K.; Sekiguchi, T.; Gratzel, M. *Nat Mater* **2003**, *2*, 402.

(18) Listorti, A.; O'Regan, B.; Durrant, J. R. *Chem. Mat.* **2011**, 3381.

(19) Bisquert, J.; Fabregat-Santiago, F.; Mora-Seró, I. n.; Garcia-Belmonte, G.; Giménez, S. *J. Phys. Chem. C* **2009**, *113*, 17278.

(20) Nelson, J.; Chandler, R. E. *Coord. Chem. Rev.* **2004**, *248*, 1181.

(21) Kamat, P. V.; Tvrdy, K.; Baker, D. R.; Radich, J. G. *Chem. Rev.* **2010**, *110*, 6664.

(22) Wei, D.; Andrew, P.; Ryhänen, T. *Journal of Chemical Technology & Biotechnology* **2010**, *85*, 1547.

(23) Zhang, Q.; Dandeneau, C. S.; Zhou, X.; Cao, G. *Adv. Mater.* **2009**, *21*, 4087.

(24) Saito, M.; Fujihara, S. *Energy & Environmental Science* **2008**, *1*, 280.

(25) Akhtar, M. S.; Khan, M. A.; Jeon, M. S.; Yang, O. B. *Electrochim. Acta* **2008**, *53*, 7869.

(26) Lin, C.; Lin, H.; Li, J.; Li, X. *Journal of Alloys and Compounds* **2008**, *462*, 175.

(27) Xu, C.; Wu, J.; Desai, U. V.; Gao, D. *J. Am. Chem. Soc.* **2011**, *133*, 8122.

(28) Hsu, Y. F.; Xi, Y. Y.; Yip, C. T.; Djurisic, A. B.; Chan, W. K. *J. Appl. Phys.* **2008**, *103*, 083114.

(29) Memarian, N.; Concina, I.; Braga, A.; Rozati, S. M.; Vomiero, A.; Sberveglieri, G. *Angew. Chem., Int. Ed.* **2011**, *50*, 12321.

(30) Anta, J. A.; Guillén, E.; Tena-Zaera, R. *J. Phys. Chem. C* **2012**, *116*, 11413.

(31) Xu, F.; Sun, L. *Energy & Environmental Science* **2011**, *4*, 818.

(32) Gonzalez-Valls, I.; Lira-Cantu, M. *Energy & Environmental Science* **2009**, *2*, 19.

(33) Peter, L. M. *J. Phys. Chem. Lett.* **2011**, 1861.

(34) Parks, G. A. *Chem. Rev.* **1965**, *65*, 177.

(35) Law, M.; Greene, L. E.; Radenovic, A.; Kuykendall, T.; Liphardt, J.; Yang, P. *J. Phys. Chem. B* **2006**, *110*, 22652.

(36) Nguyen, H.-M.; Mane, R. S.; Ganesh, T.; Han, S.-H.; Kim, N. *J. Phys. Chem. C* **2009**, *113*, 9206.

(37) Guillen, E.; Idigoras, J.; Berger, T.; Anta, J. A.; Fernandez-Lorenzo, C.; Alcantara, R.; Navas, J.; Martin-Calleja, J. *Physical Chemistry Chemical Physics* **2011**, *13*, 207.

(38) Shin, Y.-J.; Lee, J.-H.; Park, J.-H.; Park, N.-G. *Chemistry Letters* **2007**, *36*, 1506.

(39) Greene, L. E.; Law, M.; Yuhas, B. D.; Yang, P. *The Journal of Physical Chemistry C* **2007**, *111*, 18451.

(40) Anderson, N. A.; Ai, X.; Lian, T. *The Journal of Physical Chemistry B* **2003**, *107*, 14414.

(41) Benkö, G.; Kallioinen, J.; Korppi-Tommola, J. E. I.; Yartsev, A. P.; Sundström, V. *Journal of the American Chemical Society* **2001**, *124*, 489.

(42) Anderson, N. A.; Lian, T. *Coordination Chemistry Reviews* **2004**, *248*, 1231.

(43) Enright, B.; Fitzmaurice, D. *The Journal of Physical Chemistry* **1996**, *100*, 1027.

(44) Stockwell, D.; Yang, Y.; Huang, J.; Anfuso, C.; Huang, Z.; Lian, T. *J. Phys. Chem. C* **2010**, *114*, 6560.

(45) Jarzebski, Z. M.; Marton, J. P. *J. Electrochem. Soc.* **1976**, *123*, 299C.

(46) Falabretti, B.; Robertson, J. *J. Appl. Phys.* **2007**, *102*, 123703.

(47) Senevirathna, M. K. I.; Pitigala, P. K. D. D. P.; Premalal, E. V. A.; Tennakone, K.; Kumara, G. R. A.; Konno, A. *Sol. Energy Mater. Sol. Cells* **2007**, *91*, 544.

(48) Bolts, J. M.; Wrighton, M. S. *J. Phys. Chem.* **1976**, *80*, 2641.

(49) Green, A. N. M.; Palomares, E.; Haque, S. A.; Kroon, J. M.; Durrant, J. R. *The Journal of Physical Chemistry B* **2005**, *109*, 12525.

(50) Hagfeldt, A.; Boschloo, G.; Sun, L.; Kloo, L.; Pettersson, H. *Chem. Rev.* **2010**, *110*, 6595.

(51) Vinodgopal, K.; Kamat, P. V. *Environmental Science & Technology* **1995**, *29*, 841.

(52) Vinodgopal, K.; Bedja, I.; Kamat, P. V. *Chem. Mat.* **1996**, *8*, 2180.

(53) Scaife, D. E. *Solar Energy* **1980**, *25*, 41.

(54) Ramasamy, E.; Lee, J. *J. Phys. Chem. C* **2010**, *114*, 22032.

(55) Ferrere, S.; Zaban, A.; Gregg, B. A. *J. Phys. Chem. B* **1997**, *101*, 4490.

(56) Bedja, I.; Hotchandani, S.; Kamat, P. V. *J. Phys. Chem.* **1994**, *98*, 4133.

(57) Snaith, H. J.; Ducati, C. *Nano Letters* **2010**, *10*, 1259.

(58) Tiwana, P.; Docampo, P.; Johnston, M. B.; Snaith, H. J.; Herz, L. M. *ACS Nano* **2011**, *5*, 5158.

(59) Birkel, A.; Lee, Y.-G.; Koll, D.; Meerbeek, X. V.; Frank, S.; Choi, M. J.; Kang, Y. S.; Char, K.; Tremel, W. *Energy & Environmental Science* **2012**, *5*, 5392.

(60) Kay, A.; Grätzel, M. *Chem. Mat.* **2002**, *14*, 2930.

(61) Qian, J.; Liu, P.; Xiao, Y.; Jiang, Y.; Cao, Y.; Ai, X.; Yang, H. *Adv. Mater.* **2009**, *21*, 3663.

(62) Xing, J.; Fang, W. Q.; Li, Z.; Yang, H. G. *Industrial & Engineering Chemistry Research* **2012**, *51*, 4247.

(63) Kumara, G. R. R. A.; Tennakone, K.; Perera, V. P. S.; Konno, A.; Kaneko, S.; Okuya, M. *Journal of Physics D: Applied Physics* **2001**, *34*, 868.

(64) Coutts, T. J.; Young, D. L.; Li, X.; Mulligan, W. P.; Wu, X. *J. Vac. Sci. Technol. A* **2000**, *18*, 2646.

(65) Cun, W.; Xinming, W.; Jincai, Z.; Bixian, M.; Guoying, S.; Ping'an, P.; Jiamo, F. *J. Mater. Sci.* **2002**, *37*, 2989.

(66) Tennakone, K.; R. R. A. Kumara, G.; R. M. Kottegoda, I.; P. S. Perera, V. *Chem. Commun.* **1999**, 15.

(67) Tan, B.; Toman, E.; Li, Y.; Wu, Y. *J. Am. Chem. Soc.* **2007**, *129*, 4162.

(68) Lana-Villarreal, T.; Boschloo, G.; Hagfeldt, A. *J. Phys. Chem. C* **2007**, *111*, 5549.

(69) Kou, H.; Yang, S. *J. Phys. Chem. C* **2012**, *116*, 6376.

(70) Alpuche-Aviles, M. A.; Wu, Y. *J. Am. Chem. Soc.* **2009**, *131*, 3216.

(71) Li, Z.; Zhou, Y.; Zhang, J.; Tu, W.; Liu, Q.; Yu, T.; Zou, Z. *Crystal Growth & Design* **2012**, *12*, 1476.

(72) Chen, J.; Lu, L.; Wang, W. *J. Phys. Chem. C* **2012**, *116*, 10841.

(73) Sayama, K.; Arakawa, H.; Domen, K. *Catal. Today* **1996**, *28*, 175.

(74) Lenzmann, F.; Krueger, J.; Burnside, S.; Brooks, K.; Grätzel, M.; Gal, D.; Rühle, S.; Cahen, D. *J. Phys. Chem. B* **2001**, *105*, 6347.

(75) Maruska, H. P.; Ghosh, A. K. *Solar Energy* **1978**, *20*, 443.

(76) Sayama, K.; Sugihara, H.; Arakawa, H. *Chem. Mat.* **1998**, *10*, 3825.

(77) *Light, Water, Hydrogen: The Solar Generation of Hydrogen by Water Photoelectrolysis*; Grimes, C. A.; Varghese, O. K.; Ranjan, S., Eds.; Springer: New York, 2007.

(78) Chen, S. G.; Chappel, S.; Diamant, Y.; Zaban, A. *Chem. Mat.* **2001**, *13*, 4629.

(79) Guo, P.; Aegerter, M. A. *Thin Solid Films* **1999**, *351*, 290.

(80) Aegerter, M. A.; Schmitt, M.; Guo, Y. *Int. J. Photoenergy.* **2002**, *4*, 1.

(81) EGUCHI, K.; KOGA, H.; SEKIZAWA, K.; SASAKI, K. *JCS-Japan* **2000**, *108*, 1067.

(82) Wei, M.; Qi, Z.-m.; Ichihara, M.; Zhou, H. *Acta Materialia* **2008**, *56*, 2488.

(83) Le Viet, A.; Jose, R.; Reddy, M. V.; Chowdari, B. V. R.; Ramakrishna, S. *J. Phys. Chem. C* **2010**, *114*, 21795.

(84) Ghosh, R.; Brennaman, M. K.; Uher, T.; Ok, M.-R.; Samulski, E. T.; McNeil, L. E.; Meyer, T. J.; Lopez, R. *ACS Applied Materials & Interfaces* **2011**.

(85) Xia, J.; Masaki, N.; Jiang, K.; Yanagida, S. *J. Phys. Chem. C* **2007**, *111*, 8092.

(86) Zaban, A.; Chen, S. G.; Chappel, S.; Gregg, B. A. *Chem. Commun.* **2000**, 2231.

(87) Kwang-Soon, A.; Moon-Sung, K.; Jae-Kwan, L.; Byong-Cheol, S.; Ji-Won, L. *Appl. Phys. Lett.* **2006**, *89*, 013103.

(88) Ou, J. Z.; Rani, R. A.; Ham, M.-H.; Field, M. R.; Zhang, Y.; Zheng, H.; Reece, P.; Zhuiykov, S.; Sriram, S.; Bhaskaran, M.; Kaner, R. B.; Kalantar-zadeh, K. *ACS Nano* **2012**, *6*, 4045.

(89) Chen, X.; Shen, S.; Guo, L.; Mao, S. S. *Chem. Rev.* **2010**, *110*, 6503.

(90) Prado, A. G. S.; Bolzon, L. B.; Pedroso, C. P.; Moura, A. O.; Costa, L. L. *Appl. Catal. B.* **2008**, *82*, 219.

(91) Kung, H. H.; Jarrett, H. S.; Sleight, A. W.; Ferretti, A. *J. Appl. Phys.* **1977**, *48*, 2463.

(92) Moser, J. E.; Wolf, M.; Lenzmann, F.; Grätzel, M. *Zeitschrift für Physikalische Chemie* **1999**, *212*, 85.

(93) Kim, Y. I.; Atherton, S. J.; Brigham, E. S.; Mallouk, T. E. *J. Phys. Chem.* **1993**, *97*, 11802.

(94) P. Clechet, J. M., R. Oliver, and C. Vallouy *C.R. Acad. Sci. C* **1976**, *282*, 887.

(95) Barros Filho, D.; Abreu Filho, P.; Werner, U.; Aegerter, M. *J. Sol-Gel Sci. Technol.* **1997**, *8*, 735.

(96) Hanlin Luo , W. S., Paul G. Hoertz, Kenneth Hanson, Rudresh Ghosh , Sylvie Rangan, M. Kyle Brennaman, Javier J. Concenpcion, Robert Binstead, Rene Lopez, and Thomas J. Meyer. **2012**.

(97) Lotnyk, A.; Senz, S.; Hesse, D. *Thin Solid Films* **2007**, *515*, 3439.

(98) De Souza, R. A.; Fleig, J.; Maier, J.; Kienzle, O.; Zhang, Z.; Sigle, W.; Rühle, M. *Journal of the American Ceramic Society* **2003**, *86*, 922.

(99) Balaya, P.; Jamnik, J.; Fleig, J.; Maier, J. *Appl. Phys. Lett.* **2006**, *88*, 062109.

(100) Burnside, S.; Moser, J.-E.; Brooks, K.; Grätzel, M.; Cahen, D. *J. Phys. Chem. B* **1999**, *103*, 9328.

(101) Yang, S.; Kou, H.; Wang, H.; Cheng, K.; Wang, J. *J. Phys. Chem. C* **2009**, *114*, 815.

(102) Yang, S.; Kou, H.; Wang, J.; Xue, H.; Han, H. *J. Phys. Chem. C* **2010**, *114*, 4245.

(103) Zheng, H.; Tachibana, Y.; Kalantar-zadeh, K. *Langmuir* **2010**, *26*, 19148.

(104) Dixon, R. A.; Williams, J. J.; Morris, D.; Rebane, J.; Jones, F. H.; Egdell, R. G.; Downes, S. W. *Surf. Sci.* **1998**, *399*, 199.

(105) Zheng, H.; Sadek, A. Z.; Latham, K.; Kalantar-Zadeh, K. *Electrochemistry Communications* **2009**, *11*, 768.

(106) Liu, Z.; Bando, Y.; Tang, C. *Chem. Phys. Lett.* **2003**, *372*, 179.

(107) Yang, M.; Shrestha, N. K.; Schmuki, P. *Electrochemistry Communications* **2009**, *11*, 1908.

(108) Miyauchi, M.; Nakajima, A.; Watanabe, T.; Hashimoto, K. *Chemistry of Materials* **2002**, *14*, 4714.

(109) Sadek, A. Z.; Zheng, H.; Breedon, M.; Bansal, V.; Bhargava, S. K.; Latham, K.; Zhu, J.; Yu, L.; Hu, Z.; Spizzirri, P. G.; Wlodarski, W.; Kalantar-zadeh, K. *Langmuir* **2009**, *25*, 9545.

(110) Kosmulski, M. *Journal of the American Chemical Society* **2001**, *124*, 1127.

(111) Lu, X.; Ding, S.; Lin, T.; Mou, X.; Hong, Z.; Huang, F. *Dalton Trans.* **2012**, *41*, 622.

(112) Turković, A.; Cmjak Orel, Z. *Sol. Energy Mater. Sol. Cells* **1997**, *45*, 275.

(113) Lu, X.; Zheng, D.; Zhang, P.; Liang, C.; Liu, P.; Tong, Y. *Chem. Commun.* **2010**, *46*, 7721.

(114) Zhang, Y.; Zhang, H.; Wang, Y.; Zhang, W. F. *J. Phys. Chem. C* **2008**, *112*, 8553.

(115) Guo, F.-a.; Li, G.; Zhang, W. *Int. J. Photoenergy.* **2010**, *2010*.

(116) Choi, J.-H.; Kwon, S.-H.; Jeong, Y.-K.; Kim, I.; Kim, K.-H. *J. Electrochem. Soc.* **2011**, *158*, B749.

(117) Feng, X.; Shankar, K.; Paulose, M.; Grimes, C. A. *Angew. Chem., Int. Ed.* **2009**, *48*, 8095.

(118) Liu, J.; Yang, H.; Tan, W.; Zhou, X.; Lin, Y. *Electrochim. Acta* **2010**, *56*, 396.

(119) Ogomi, Y.; Kato, T.; Hayase, S. *Journal of Photopolymer Science and Technology* **2006**, *19*, 403.

(120) Tsvetkov, N.; Larina, L.; Shevaleevskiy, O.; Ahn, B. T. *J. Electrochem. Soc.* **2011**, *158*, B1281.

(121) Lü, X.; Mou, X.; Wu, J.; Zhang, D.; Zhang, L.; Huang, F.; Xu, F.; Huang, S. *Adv. Funct. Mater.* **2010**, *20*, 509.

(122) Yang, J.; Zhang, X.; Wang, C.; Sun, P.; Wang, L.; Xia, B.; Liu, Y. *Solid State Sciences* **2012**, *14*, 139.

(123) Mei, B.; Sanchez, M. D.; Reinecke, T.; Kaluza, S.; Xia, W.; Muhler, M. *J. Mater. Chem.* **2011**, *21*, 11781.

(124) Archana, P. S.; Jose, R.; Yusoff, M. M.; Ramakrishna, S. *Appl. Phys. Lett.* **2011**, *98*, 152106.

(125) Yu, M.; Natu, G.; Ji, Z.; Wu, Y. *J. Phys. Chem. Lett.* **2012**, *3*, 1074.

(126) Duan, Y.; Fu, N.; Liu, Q.; Fang, Y.; Zhou, X.; Zhang, J.; Lin, Y. *J. Phys. Chem. C* **2012**, *116*, 8888.

(127) Ko, K. H.; Lee, Y. C.; Jung, Y. J. *J. Colloid Interface Sci.* **2005**, *283*, 482.

(128) Kim, C.; Kim, K.-S.; Kim, H. Y.; Han, Y. S. *J. Mater. Chem.* **2008**, *18*, 5809.

(129) Wang, M.; Bai, S.; Chen, A.; Duan, Y.; Liu, Q.; Li, D.; Lin, Y. *Electrochim. Acta* **2012**.

(130) Wang, K.-P.; Teng, H. *Physical Chemistry Chemical Physics* **2009**, *11*, 9489.

(131) Navas, J.; Fernández-Lorenzo, C.; Aguilar, T.; Alcántara, R.; Martín-Calleja, J. *physica status solidi (a)* **2012**, *209*, 378.

(132) So, S.; Lee, K.; Schmuki, P. *physica status solidi (RRL) – Rapid Research Letters* **2012**, *6*, 169.

(133) Imahori, H.; Hayashi, S.; Umeyama, T.; Eu, S.; Oguro, A.; Kang, S.; Matano, Y.; Shishido, T.; Ngamsinlapasathian, S.; Yoshikawa, S. *Langmuir* **2006**, *22*, 11405.

(134) Tian, H.; Hu, L.; Li, W.; Sheng, J.; Xu, S.; Dai, S. *J. Mater. Chem.* **2011**, *21*, 7074.

(135) Zhang, J.; Sun, Q.; Zheng, J.; Zhang, X.; Cui, Y.; Wang, P.; Li, W.; Zhu, Y. *Journal of Renewable and Sustainable Energy* **2011**, *3*, 033108.

(136) Subramanian, A.; Wang, H.-W. *Appl. Surf. Sci.* **2012**, *258*, 6479.

(137) Hou, Q.; Zheng, Y.; Chen, J.-F.; Zhou, W.; Deng, J.; Tao, X. *J. Mater. Chem.* **2011**, *21*, 3877.

(138) He, J.; Lindström, H.; Hagfeldt, A.; Lindquist, S.-E. *Sol. Energy Mater. Sol. Cells* **2000**, *62*, 265.

(139) Boschloo, G.; Hagfeldt, A. *J. Phys. Chem. B* **2001**, *105*, 3039.

(140) Bandara, J.; Weerasinghe, H. *Sol. Energy Mater. Sol. Cells* **2005**, *85*, 385.

(141) He, J.; Lindström, H.; Hagfeldt, A.; Lindquist, S.-E. *J. Phys. Chem. B* **1999**, *103*, 8940.

(142) Gibson, E. A.; Smeigh, A. L.; Le Pleux, L.; Fortage, J.; Boschloo, G.; Blart, E.; Pellegrin, Y.; Odobel, F.; Hagfeldt, A.; Hammarström, L. *Angew. Chem., Int. Ed.* **2009**, *48*, 4402.

(143) Gibson, E. A.; Smeigh, A. L.; Le Pleux, L. c.; Hammarström, L.; Odobel, F.; Boschloo, G.; Hagfeldt, A. *J. Phys. Chem. C* **2011**, *115*, 9772.

(144) Le Pleux, L.; Smeigh, A. L.; Gibson, E.; Pellegrin, Y.; Blart, E.; Boschloo, G.; Hagfeldt, A.; Hammarstrom, L.; Odobel, F. *Energy & Environmental Science* **2011**, *4*, 2075.

(145) Borgström, M.; Blart, E.; Boschloo, G.; Mukhtar, E.; Hagfeldt, A.; Hammarström, L.; Odobel, F. *J. Phys. Chem. B* **2005**, *109*, 22928.

(146) Morandeira, A.; Boschloo, G.; Hagfeldt, A.; Hammarström, L. *J. Phys. Chem. B* **2005**, *109*, 19403.

(147) Mizoguchi, Y.; Fujihara, S. *Electrochemical and Solid-State Letters* **2008**, *11*, K78.

(148) Morandeira, A.; Fortage, J.; Edvinsson, T.; Le Pleux, L.; Blart, E.; Boschloo, G.; Hagfeldt, A.; Hammarstrom, L.; Odobel, F. *J. Phys. Chem. C* **2008**, *112*, 1721.

(149) Yen, Y.-S.; Chen, W.-T.; Hsu, C.-Y.; Chou, H.-H.; Lin, J. T.; Yeh, M.-C. P. *Org. Lett.* **2011**, *13*, 4930.

(150) Ji, Z.; Natu, G.; Huang, Z.; Wu, Y. *Energy & Environmental Science* **2011**, *4*, 2818.

(151) Nattestad, A.; Mozer, A. J.; Fischer, M. K. R.; Cheng, Y. B.; Mishra, A.; Bauerle, P.; Bach, U. *Nat Mater* **2010**, *9*, 31.

(152) Qin, P.; Zhu, H.; Edvinsson, T.; Boschloo, G.; Hagfeldt, A.; Sun, L. *J. Am. Chem. Soc.* **2008**, *130*, 8570.

(153) Qin, P.; Wiberg, J.; Gibson, E. A.; Linder, M.; Li, L.; Brinck, T.; Hagfeldt, A.; Albinsson, B.; Sun, L. *J. Phys. Chem. C* **2010**, *114*, 4738.

(154) Qin, P.; Linder, M.; Brinck, T.; Boschloo, G.; Hagfeldt, A.; Sun, L. *Adv. Mater.* **2009**, *21*, 2993.

(155) Li, L.; Duan, L.; Wen, F.; Li, C.; Wang, M.; Hagfeldt, A.; Sun, L. *Chem. Commun.* **2012**, *48*, 988.

(156) Mori, S.; Fukuda, S.; Sumikura, S.; Takeda, Y.; Tamaki, Y.; Suzuki, E.; Abe, T. *J. Phys. Chem. C* **2008**, *112*, 16134.

(157) Li, L.; Gibson, E. A.; Qin, P.; Boschloo, G.; Gorlov, M.; Hagfeldt, A.; Sun, L. *Adv. Mater.* **2010**, *22*, 1759.

(158) Chitambar, M.; Wang, Z.; Liu, Y.; Rockett, A.; Maldonado, S. *J. Am. Chem. Soc.* **2012**.

(159) Arai, T.; Tajima, S.; Sato, S.; Uemura, K.; Morikawa, T.; Kajino, T. *Chem. Commun.* **2011**, *47*, 12664.

(160) Sato, S.; Arai, T.; Morikawa, T.; Uemura, K.; Suzuki, T. M.; Tanaka, H.; Kajino, T. *J. Am. Chem. Soc.* **2011**, *133*, 15240.

(161) Sumikura, S.; Mori, S.; Shimizu, S.; Usami, H.; Suzuki, E. *Journal of Photochemistry and Photobiology A: Chemistry* **2008**, *194*, 143.

(162) Tran, P. D.; Wong, L. H.; Barber, J.; Loo, J. S. C. *Energy & Environmental Science* **2012**, *5*, 5902.

(163) Paracchino, A.; Laporte, V.; Sivula, K.; Grätzel, M.; Thimsen, E. *Nat Mater* **2011**, *10*, 456.

(164) Bandara, J.; Yasomanee, J. P. *Semiconductor Science and Technology* **2007**, *22*, 20.

(165) Benko, F. A.; Koffyberg, F. P. *Journal of Physics and Chemistry of Solids* **1984**, *45*, 57.

(166) Henry, C. H. *J. Appl. Phys.* **1980**, *51*, 4494.

(167) Martí, A.; Araújo, G. L. *Sol. Energy Mater. Sol. Cells* **1996**, *43*, 203.

(168) Yum, J.-H.; Baranoff, E.; Wenger, S.; Nazeeruddin, M. K.; Gratzel, M. *Energy & Environmental Science* **2011**, *4*, 842.

(169) Kubo, W.; Sakamoto, A.; Kitamura, T.; Wada, Y.; Yanagida, S. *Journal of Photochemistry and Photobiology A: Chemistry* **2004**, *164*, 33.

(170) Murayama, M.; Mori, T. *Journal of Physics D: Applied Physics* **2007**, *40*, 1664.

(171) Yamaguchi, T.; Uchida, Y.; Agatsuma, S.; Arakawa, H. *Sol. Energy Mater. Sol. Cells* **2009**, *93*, 733.

(172) Sumikura, S.; Mori, S.; Shimizu, S.; Usami, H.; Suzuki, E. *Journal of Photochemistry and Photobiology A: Chemistry* **2008**, *199*, 1.

(173) Bandara, J.; Divarathne, C. M.; Nanayakkara, S. D. *Sol. Energy Mater. Sol. Cells* **2004**, *81*, 429.

(174) Nazeeruddin, M. K.; Kay, A.; Rodicio, I.; Humphry-Baker, R.; Mueller, E.; Liska, P.; Vlachopoulos, N.; Graetzel, M. *J. Am. Chem. Soc.* **1993**, *115*, 6382.

(175) Nazeeruddin, M. K.; Zakeeruddin, S. M.; Humphry-Baker, R.; Jirousek, M.; Liska, P.; Vlachopoulos, N.; Shklover, V.; Fischer, C.-H.; Grätzel, M. *Inorg. Chem.* **1999**, *38*, 6298.

(176) Wang, P.; Zakeeruddin, S. M.; Comte, P.; Charvet, R.; Humphry-Baker, R.; Grätzel, M. *J. Phys. Chem. B* **2003**, *107*, 14336.

(177) Song, W.; Brennaman, M. K.; Concepcion, J. J.; Jurss, J. W.; Hoertz, P. G.; Luo, H.; Chen, C.; Hanson, K.; Meyer, T. J. *J. Phys. Chem. C* **2011**, *115*, 7081.

(178) Enea, O.; Moser, J.; Grätzel, M. *J . Electroanal. Chem. Interfacial Electrochem.* **1989**, *259*, 59.

(179) Qin, P.; Zhu, H.; Edvinsson, T.; Boschloo, G.; Hagfeldt, A.; Sun, L. *J. Am. Chem. Soc.* **2008**, *130*, 8570.

(180) Qin, P.; Linder, M.; Brinck, T.; Boschloo, G.; Hagfeldt, A.; Sun, L. *Adv. Mater.* **2009**, *21*, 2993.

(181) Qin, P.; Wiberg, J.; Gibson, E. A.; Linder, M.; Li, L.; Brinck, T.; Hagfeldt, A.; Albinsson, B.; Sun, L. *J. Phys. Chem. C* **2010**, *114*, 4738.

(182) Morandeira, A.; Fortage, J.; Edvinsson, T.; Le Pleux, L.; Blart, E.; Boschloo, G.; Hagfeldt, A.; Hammarstrom, L.; Odobel, F. *J. Phys. Chem. C* **2008**, *112*, 1721.

(183) Armstrong, N. R.; Veneman, P. A.; Ratcliff, E.; Placencia, D.; Brumbach, M. *Acc. Chem. Res.* **2009**, *42*, 1748.

(184) Walzer, K.; Maennig, B.; Pfeiffer, M.; Leo, K. *Chem. Rev.* **2007**, *107*, 1233.

(185) Chopra, K. L.; Major, S.; Pandya, D. K. *Thin Solid Films* **1983**, *102*, 1.

(186) Ginley, D. S.; Bright, C. *MRS Bull.* **2000**, *25*, 15.

(187) Calnan, S.; Tiwari, A. N. *Thin Solid Films* **2010**, *518*, 1839.

(188) Lundstrom, M. *Fundamentals of Carrier Transport*; Cambridge University Press, 2009.

(189) Ellmer, K.; Mientus, R. *Thin Solid Films* **2008**, *516*, 5829.

(190) Thangaraju, B. *Thin Solid Films* **2002**, *402*, 71.

(191) Clanget, R. *Appl. Phys.* **1973**, *2*, 247.

(192) Ellmer, K. *Journal of Physics D: Applied Physics* **2001**, *34*, 3097.

(193) Chopra, K.; Das, S. In *Thin Film Solar Cells*; Springer US: 1983, p 1.

(194) Batzill, M.; Diebold, U. *Progress in Surface Science* **2005**, *79*, 47.

(195) Kawazoe, H.; Yasukawa, M.; Hyodo, H.; Kurita, M.; Yanagi, H.; Hosono, H. *Nature* **1997**, *389*, 939.

(196) Exarhos, G. J.; Zhou, X.-D. *Thin Solid Films* **2007**, *515*, 7025.

(197) Banerjee, A. N.; Chattopadhyay, K. K. *Progress in Crystal Growth and Characterization of Materials* **2005**, *50*, 52.

(198) Kawazoe, H.; Yanagi, H.; Ueda, K.; Hosono, H. *MRS Bull.* **2000**, *25*, 28.

(199) Yanagi, H.; Hase, T.; Ibuki, S.; Ueda, K.; Hosono, H. *Appl. Phys. Lett.* **2001**, *78*, 1583.

(200) Tate, J.; Jayaraj, M. K.; Draeseke, A. D.; Ulbrich, T.; Sleight, A. W.; Vanaja, K. A.; Nagarajan, R.; Wager, J. F.; Hoffman, R. L. *Thin Solid Films* **2002**, *411*, 119.

(201) Tadatsugu, M. *Semiconductor Science and Technology* **2005**, *20*, S35.

(202) Hosono, H. *Thin Solid Films* **2007**, *515*, 6000.

(203) Kurz, A.; Brakecha, K.; Puetz, J.; Aegerter, M. A. *Thin Solid Films* **2006**, *502*, 212.

(204) Minami, T.; Nanto, H.; Shooji, S.; Takata, S. *Thin Solid Films* **1984**, *111*, 167.

(205) Dawar, A. L.; Joshi, J. C. *J. Mater. Sci.* **1984**, *19*, 1.

(206) Minami, T. *MRS Bull.* **2000**, *25*, 38.

(207) Tseng, S.-F.; Hsiao, W.-T.; Chiang, D.; Huang, K.-C.; Chou, C.-P. *Appl. Surf. Sci.* **2011**, *257*, 7204.

(208) Minami, T.; Takeda, Y.; Takata, S.; Kakumu, T. *Thin Solid Films* **1997**, *308–309*, 13.

(209) Enoki, H.; Nakayama, T.; Echigoya, J. *physica status solidi (a)* **1992**, *129*, 181.

(210) Tadatsugu, M.; Hideo, S.; Toshikazu, K.; Shinzo, T. *Japanese Journal of Applied Physics* **1995**, *34*, L971.

(211) Minami, T. *Journal of Vacuum Science & Technology A* **1999**, *17*, 1765.

(212) Minami, T.; Takata, S.; Kakumu, T.; Sonohara, H. *Thin Solid Films* **1995**, *270*, 22.

(213) Minami, T.; Takata, S.; Kakumu, T.; Sonohara, H. *Thin Solid Films* **1995**, *270*, 22.

(214) Gordon, R. G. *MRS Bull.* **2000**, *25*, 52.

(215) Akio Suzuki; Tatsuhiko Matsushita; Naoki Wada; Yoshiaki Sakamoto; Masahiro Okuda *Japanese Journal of Applied Physics* **1996**, *35*, L56.

(216) Minami, T.; Ida, S.; Miyata, T. *Thin Solid Films* **2002**, *416*, 92.

(217) Shanthi, E.; Banerjee, A.; Dutta, V.; Chopra, K. L. *J. Appl. Phys.* **1982**, *53*, 1615.

(218) Geraldo, V.; Scalvi, L. V. A.; Lisboa-Filho, P. N.; Morilla-Santos, C. *Journal of Physics and Chemistry of Solids* **2006**, *67*, 1410.

(219) Hamberg, I.; Granqvist, C. G. *J. Appl. Phys.* **1986**, *60*, R123.

(220) Nütz, T.; Felde, U. z.; Haase, M. *The Journal of Chemical Physics* **1999**, *110*, 12142.

(221) Rockenberger, J.; zum Felde, U.; Tischer, M.; Tröger, L.; Haase, M.; Weller, H. *The Journal of Chemical Physics* **2000**, *112*, 4296.

(222) Kojima, M.; Kato, H.; Gatto, M. *Philosophical Magazine Part B* **1993**, *68*, 215.

(223) Berry, F. J.; Laundy, B. J. *Journal of the Chemical Society, Dalton Transactions* **1981**, 1442.

(224) Nütz, T.; Haase, M. *J. Phys. Chem. B* **2000**, *104*, 8430.

(225) Boschloo, G.; Fitzmaurice, D. *J. Phys. Chem. B* **1999**, *103*, 3093.

(226) Niederberger, M.; Garnweitner, G. *Chemistry – A European Journal* **2006**, *12*, 7282.

(227) Livage, J.; Ganguli, D. *Sol. Energy Mater. Sol. Cells* **2001**, *68*, 365.

(228) Niederberger, M. P., Nicola *Metal Oxide Nanoparticles in Organic Solvents*; Springer-Verlag: London, 2009.

(229) Cushing, B. L.; Kolesnichenko, V. L.; O'Connor, C. J. *Chem. Rev.* **2004**, *104*, 3893.

(230) Hench, L. L.; West, J. K. *Chem. Rev.* **1990**, *90*, 33.

(231) Bradley, D. C. *Chem. Rev.* **1989**, *89*, 1317.

(232) Mehrotra, R. C.; Singh, A. *Progress in Inorganic Chemistry, Vol 46* **1997**, *46*, 239.

(233) In, M.; Sanchez, C. *J. Phys. Chem. B* **2005**, *109*, 23870.

(234) Hubert-Pfalzgraf, L. G. *J. Mater. Chem.* **2004**, *14*, 3113.

(235) Livage, J.; Henry, M.; Sanchez, C. *Progress in Solid State Chemistry* **1988**, *18*, 259.

(236) Corriu, R. J. P.; Leclercq, D. *Angewandte Chemie International Edition in English* **1996**, *35*, 1420.

(237) Monge, M.; Kahn, M. L.; Maisonnat, A.; Chaudret, B. *Angewandte Chemie* **2003**, *115*, 5479.

(238) Kominami, H.; Kohno, M.; Takada, Y.; Inoue, M.; Inui, T.; Kera, Y. *Industrial & Engineering Chemistry Research* **1999**, *38*, 3925.

(239) Niederberger, M. *Acc. Chem. Res.* **2007**, *40*, 793.

(240) Hay, J. N.; Raval, H. M. *Chem. Mat.* **2001**, *13*, 3396.

(241) Masashi, I. *Journal of Physics: Condensed Matter* **2004**, *16*, S1291.

(242) Garnweitner, G.; Niederberger, M. *J. Am. Ceram. Soc.* **2006**, *89*, 1801.

(243) Mutin, P. H.; Vioux, A. *Journal of Materials Chemistry A* **2013**, *1*, 11504.

(244) Bilecka, I.; Djerdj, I.; Niederberger, M. *Chem. Commun.* **2008**, 886.

(245) Pinna, N.; Neri, G.; Antonietti, M.; Niederberger, M. *Angew. Chem., Int. Ed.* **2004**, *43*, 4345.

(246) Hu, M.; Xu, J.; Gao, J.; Yang, S.; Wong, J. S. P.; Li, R. K. Y. *Dalton Trans.* **2013**, *42*, 9777.

(247) Niederberger, M.; Garnweitner, G.; Pinna, N.; Antonietti, M. *J. Am. Chem. Soc.* **2004**, *126*, 9120.

(248) Baghbanzadeh, M.; Carbone, L.; Cozzoli, P. D.; Kappe, C. O. *Angew. Chem., Int. Ed.* **2011**, *50*, 11312.

(249) Hoz, A. d. l. *Microwaves in Organic Synthesis*; Wiley-VCH: Weinheim, 2013.

(250) Mingos, D. M. P.; Baghurst, D. R. *Chem. Soc. Rev.* **1991**, *20*, 1.

(251) Gabriel, C.; Gabriel, S.; H. Grant, E.; H. Grant, E.; S. J. Halstead, B.; Michael P. Mingos, D. *Chem. Soc. Rev.* **1998**, *27*, 213.

(252) C. Oliver Kappe, D. D., Shaun S. Murphree; Wiley-VCH: Weinheim, 2009.

(253) Oliver Kappe, C. *Chem. Soc. Rev.* **2008**, *37*, 1127.

(254) Park, J.; Joo, J.; Kwon, S. G.; Jang, Y.; Hyeon, T. *Angew. Chem., Int. Ed.* **2007**, *46*, 4630.

(255) Bilecka, I.; Elser, P.; Niederberger, M. *ACS Nano* **2009**, *3*, 467.

(256) Kubli, M.; Luo, L.; Bilecka, I.; Niederberger, M. *CHIMIA International Journal for Chemistry* **2010**, *64*, 170.

(257) Bilecka, I.; Kubli, M.; Amstad, E.; Niederberger, M. *J. Sol-Gel Sci. Technol.* **2011**, *57*, 313.

(258) Bilecka, I.; Luo, L.; Djerdj, I.; Rossell, M. D.; Jagodič, M.; Jagličić, Z.; Masubuchi, Y.; Kikkawa, S.; Niederberger, M. *J. Phys. Chem. C* **2011**, *115*, 1484.

(259) Hammarberg, E.; Prodi-Schwab, A.; Feldmann, C. *Thin Solid Films* **2008**, *516*, 7437.

(260) Luo, L.; Rossell, M. D.; Xie, D.; Erni, R.; Niederberger, M. *ACS Sustainable Chemistry & Engineering* **2012**, *1*, 152.

(261) Luo, L.; Häfliger, K.; Xie, D.; Niederberger, M. *J. Sol-Gel Sci. Technol.* **2013**, *65*, 28.

(262) Sing, K. S. W. E., D. H.; Haul, R. A. W.; Moscou, L.; Pierotti, R. A.; Rouquerol,J.; Siemieniewska, T. *Pure Appl. Chem.* **1985**, *57*, 603.

(263) Beck, J. S.; Vartuli, J. C.; Roth, W. J.; Leonowicz, M. E.; Kresge, C. T.; Schmitt, K. D.; Chu, C. T. W.; Olson, D. H.; Sheppard, E. W. *J. Am. Chem. Soc.* **1992**, *114*, 10834.

(264) Kresge, C. T. L., M. E.;Roth, W. J.;Vartuli, J. C.; Beck, J. S.; *Nature Chem* **1992**, *359*, 710.

(265) Deng, Y.; Wei, J.; Sun, Z.; Zhao, D. *Chem. Soc. Rev.* **2013**, *42*, 4054.

(266) Hartmann, M. *Chem. Mat.* **2005**, *17*, 4577.

(267) Grün, M.; Kurganov, A. A.; Schacht, S.; Schüth, F.; Unger, K. K. *Journal of Chromatography A* **1996**, *740*, 1.

(268) Lai, C.-Y.; Trewyn, B. G.; Jeftinija, D. M.; Jeftinija, K.; Xu, S.; Jeftinija, S.; Lin, V. S. Y. *J. Am. Chem. Soc.* **2003**, *125*, 4451.

(269) Chang, H.; Joo, S. H.; Pak, C. *J. Mater. Chem.* **2007**, *17*, 3078.

(270) Orilall, M. C.; Wiesner, U. *Chem. Soc. Rev.* **2011**, *40*, 520.

(271) Wan, Y.; Zhao *Chem. Rev.* **2007**, *107*, 2821.

(272) Ren, Y.; Ma, Z.; Bruce, P. G. *Chem. Soc. Rev.* **2012**, *41*, 4909.

(273) Shi, Y.; Wan, Y.; Zhao, D. *Chem. Soc. Rev.* **2011**, *40*, 3854.

(274) Soler-Illia, G. J. A. A.; Azzaroni, O. *Chem. Soc. Rev.* **2011**, *40*, 1107.

(275) Sanchez, C.; Soler-Illia, G. J. d. A. A.; Ribot, F.; Lalot, T.; Mayer, C. R.; Cabuil, V. *Chem. Mat.* **2001**, *13*, 3061.

(276) Sanchez, C.; Boissière, C.; Grosso, D.; Laberty, C.; Nicole, L. *Chem. Mat.* **2008**, *20*, 682.

(277) Ren, Y.; Ma, Z.; Bruce, P. G. *Chem. Soc. Rev.* **2012**.

(278) Bucknall, D. G.; Anderson, H. L. *Science* **2003**, *302*, 1904.

(279) Zhao, D.; Feng, J.; Huo, Q.; Melosh, N.; Fredrickson, G. H.; Chmelka, B. F.; Stucky, G. D. *Science* **1998**, *279*, 548.

(280) Pan, J. H.; Zhao, X. S.; Lee, W. I. *Chemical Engineering Journal* **2011**, *170*, 363.

(281) Farrell, R.; Fitzgerald, T.; Borah, D.; Holmes, J.; Morris, M. *Int. J. Mol. Sci.* **2009**, *10*, 3671.

(282) Forster, S.; Konrad, M. *J. Mater. Chem.* **2003**, *13*, 2671.

(283) Cochran, E. W.; Garcia-Cervera, C. J.; Fredrickson, G. H. *Macromolecules* **2006**, *39*, 2449.

(284) Innocenzi, P.; Malfatti, L. *Chem. Soc. Rev.* **2013**, *42*, 4198.

(285) Yang, P.; Zhao, D.; Margolese, D. I.; Chmelka, B. F.; Stucky, G. D. *Nature* **1998**, *396*, 152.

(286) Yang, P.; Zhao, D.; Margolese, D. I.; Chmelka, B. F.; Stucky, G. D. *Chem. Mat.* **1999**, *11*, 2813.

(287) Zukalová, M.; Zukal, A.; Kavan, L.; Nazeeruddin, M. K.; Liska, P.; Grätzel, M. *Nano Lett.* **2005**, *5*, 1789.

(288) Li, L.; Gibson, E. A.; Qin, P.; Boschloo, G.; Gorlov, M.; Hagfeldt, A.; Sun, L. *Adv. Mater.* **2010**, *22*, 1759.

(289) Yu, C.; Fan, J.; Tian, B.; Stucky, G. D.; Zhao, D. *J. Phys. Chem. B* **2003**, *107*, 13368.

(290) Nedelcu, M.; Lee, J.; Crossland, E. J. W.; Warren, S. C.; Orilall, M. C.; Guldin, S.; Huttner, S.; Ducati, C.; Eder, D.; Wiesner, U.; Steiner, U.; Snaith, H. J. *Soft Matter* **2009**, *5*, 134.

(291) Guldin, S.; Docampo, P.; Stefik, M.; Kamita, G.; Wiesner, U.; Snaith, H. J.; Steiner, U. *Small* **2012**, *8*, 432.

(292) Crossland, E. J. W.; Nedelcu, M.; Ducati, C.; Ludwigs, S.; Hillmyer, M. A.; Steiner, U.; Snaith, H. J. *Nano Lett.* **2008**, *9*, 2813.

(293) Crossland, E. J. W.; Kamperman, M.; Nedelcu, M.; Ducati, C.; Wiesner, U.; Smilgies, D. M.; Toombes, G. E. S.; Hillmyer, M. A.; Ludwigs, S.; Steiner, U.; Snaith, H. J. *Nano Lett.* **2008**, *9*, 2807.

(294) Perlich, J.; Kaune, G.; Memesa, M.; Gutmann, J. S.; Müller-Buschbaum, P. *Philosophical Transactions of the Royal Society A: Mathematical, Physical and Engineering Sciences* **2009**, *367*, 1783.

(295) Kuemmel, M.; Smatt, J.-H.; Boissiere, C.; Nicole, L.; Sanchez, C.; Linden, M.; Grosso, D. *Journal of Materials Chemistry* **2009**, *19*, 3638.

(296) Wang, Y.; Brezesinski, T.; Antonietti, M.; Smarsly, B. *ACS Nano* **2009**, *3*, 1373.

(297) Brezesinski, T.; Groenewolt, M.; Antonietti, M.; Smarsly, B. *Angew. Chem., Int. Ed.* **2006**, *45*, 781.

(298) Lin, C.-F.; Lin, H.-P.; Mou, C.-Y.; Liu, S.-T. *Microporous and Mesoporous Materials* **2006**, *91*, 151.

(299) Smarsly, B.; Grosso, D.; Brezesinski, T.; Pinna, N.; Boissière, C.; Antonietti, M.; Sanchez, C. *Chem. Mat.* **2004**, *16*, 2948.

(300) Brezesinski, T.; Fattakhova Rohlfing, D.; Sallard, S.; Antonietti, M.; Smarsly, B. M. *Small* **2006**, *2*, 1203.

(301) Fattakhova-Rohlfing, D.; Wark, M.; Brezesinski, T.; Smarsly, B. M.; Rathouský, J. *Adv. Funct. Mater.* **2007**, *17*, 123.

(302) Wu, J.-M.; Antonietti, M.; Gross, S.; Bauer, M.; Smarsly, B. M. *ChemPhysChem* **2008**, *9*, 748.

(303) Ortel, E.; Fischer, A.; Chuenchom, L.; Polte, J.; Emmerling, F.; Smarsly, B.; Kraehnert, R. *Small* **2012**, *8*, 298.

(304) Ortel, E.; Reier, T.; Strasser, P.; Kraehnert, R. *Chem. Mat.* **2011**, *23*, 3201.

(305) Ahn, S. H.; Chi, W. S.; Park, J. T.; Koh, J. K.; Roh, D. K.; Kim, J. H. *Adv. Mater.* **2012**, *24*, 519.

(306) Son, K. J.; Ahn, S. H.; Kim, J. H.; Koh, W.-G. *ACS Appl. Mater. Interfaces* **2011**, *3*, 573.

(307) Roh, D. K.; Seo, J. A.; Chi, W. S.; Koh, J. K.; Kim, J. H. *J. Mater. Chem.* **2012**, *22*, 11079.

(308) Ahn, S. H.; Chi, W. S.; Park, J. T.; Koh, J. K.; Roh, D. K.; Kim, J. H. *Adv. Mater.* **2012**, *24*, 519.

(309) Cheng, Y.-J.; Gutmann, J. S. *J. Am. Chem. Soc.* **2006**, *128*, 4658.

(310) Perlich, J.; Schulz, L.; Abul Kashem, M. M.; Cheng, Y. J.; Memesa, M.; Gutmann, J. S.; Roth, S. V.; Müller-Buschbaum, P. *Langmuir* **2007**, *23*, 10299.

(311) Seo, Y. G.; Woo, K.; Kim, J.; Lee, H.; Lee, W. *Adv. Funct. Mater.* **2011**, *21*, 3094.

(312) Forman, A. J.; Chen, Z.; Chakthranont, P.; Jaramillo, T. F. *Chem. Mat.* **2014**, *26*, 958.

(313) Yang, Z.; Gao, S.; Li, T.; Liu, F.-Q.; Ren, Y.; Xu, T. *ACS Appl. Mater. Interfaces* **2012**, *4*, 4419.

(314) Müller, V.; Rathousky, J.; Fattakhova-Rohlfing, D. *Electrochim. Acta* **2014**, *116*, 1.

(315) Aksu, Y.; Frasca, S.; Wollenberger, U.; Driess, M.; Thomas, A. *Chem. Mat.* **2011**, *23*, 1798.

(316) Hou, K.; Puzzo, D.; Helander, M. G.; Lo, S. S.; Bonifacio, L. D.; Wang, W.; Lu, Z.-H.; Scholes, G. D.; Ozin, G. A. *Adv. Mater.* **2009**, *21*, 2492.

(317) Kent, C. A.; Concepcion, J. J.; Dares, C. J.; Torelli, D. A.; Rieth, A. J.; Miller, A. S.; Hoertz, P. G.; Meyer, T. J. *J. Am. Chem. Soc.* **2013**, *135*, 8432.

(318) Fattakhova-Rohlfing, D.; Brezesinski, T.; Rathouský, J.; Feldhoff, A.; Oekermann, T.; Wark, M.; Smarsly, B. M. *Adv. Mater.* **2006**, *18*, 2980.

(319) Müller, V.; Rasp, M.; Rathouský, J.; Schütz, B.; Niederberger, M.; Fattakhova-Rohlfing, D. *Small* **2010**, *6*, 633.

Chapter 2: A Sensitized Nb_2O_5 Photoanode for Hydrogen Production in a Dye-Sensitized Photoelectrosynthesis Cell

2.1 Introduction

Since the development of $Ru(^{II})$ polypyridyl dye sensitized nanocrystalline TiO_2 ($nanoTiO_2$) photoelectrochemical cells by Grätzel et al. in 1991,[1] dye-sensitized solar cells (DSSCs) based on wide-band gap semiconductor oxides have been improved to reach solar energy conversion efficiencies of > 10 %.[2-4] This makes DSSCs a promising as low cost alternative to traditional silicon photovoltaic devices. The photovoltage and photocurrent in DSSCs are generated from sequential steps: photo-induced molecular excitation, electron injection into the semiconductor, and intra-film electron transfer.[5] This basic scheme has also been proposed in dye-sensitized Photoelectrosynthesis cells (DSPECs) for water splitting. [6-12]

Recently, we reported a detailed study on H_2 evolution in a DSPEC based on $[Ru(bpy)_2(4,4'\text{-}(PO_3H_2)_2bpy)]^{2+}$ (Figure 2-1.; **RuP**) derivatized TiO_2 as the photoanode, a platinum cathode, and triethanolamine (TEOA) or ethylenediaminetetraacetic tetra-anion ($EDTA^{4-}$) as the reductive scavengers in aqueous solution.[13]

The role of the added scavenger was to capture Ru^{III} by reduction to Ru^{II}, thus avoiding deleterious back electron transfer between photo injected electrons, and the oxidized chromophore ($TiO_2(e^-)\text{-}Ru^{III} \rightarrow TiO_2\text{-}Ru^{II}$). The photoinjected electrons are then free to diffuse through the TiO_2 nanostructure to the underlying conducting substrate for delivery to a physically separated Pt cathode for proton reduction to H_2.

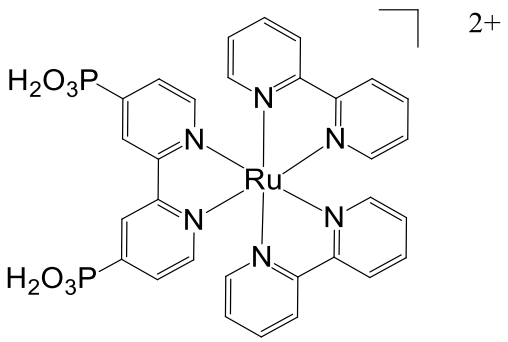

RuP

Figure 2-1. Structures of $[Ru(bpy)_2(4,4'\text{-}(PO_3H_2)_2bpy)]^{2+}$ (**RuP**).

TiO_2 has been, by far, the most intensively studied wide band gap semiconductor in DSSC and DSPEC applications. It has three types of crystal structures with different band gaps: anatase (3.23 eV), rutile (3.05 eV), and brookite (3.26 eV). [14] Anatase is normally preferable in DSSC and DSPEC applications due to its more negative conduction band potential (NHE scale) which results in a higher open circuit voltage (V_{oc}). The maximum attainable V_{oc}, the driving force for proton reduction in DSSCs, is dictated by the potential difference between the redox couple of the carrier couple, typically I_3^-/I^- in DSSC, and the conduction band of the semiconductor. In principle, devices based on semiconductor oxides with higher conduction band potentials should be able to attain an increased V_{oc} and higher photo-conversion efficiencies.

Nb_2O_5 is a wide band gap n-type semiconductor with a conduction band comprised of empty Nb^{5+} 4d orbitals[15] and a conduction band generally accepted to be 0.2-0.4 eV higher than TiO_2.[16-20] Unlike with TiO_2, literature values for the conduction band potential, E_{cb}, and band gap energy, E_g, for Nb_2O_5 are ambiguous in that they are typically cited without specification of crystal structure, morphology, and measurement conditions.[14,18,19,21-26] A conduction band energy of -0.5 V (vs NHE) for Nb_2O_5 photoelectrodes at pH 7 is commonly cited, however it is

important to note that the sample was prepared by anodic oxidation of the metal without thermal treatment and the sample was possibly amorphous.[27] Another widely referred to value for E_{cb}, for a sample that was TT-phase (hexagonal crystal), is ~ 0.4 V (vs. NHE in dry propylene carbonate with 0.2 M tetra-N-butylammonium triflate) which is negatively shifted compared to anatase TiO_2.[16,24,28] These results are particularly important because they suggest that the conduction band potential of Nb_2O_5 is at least 0.2 V more negative than TiO_2 (vs. NHE).

Nb_2O_5 has been prepared as nanoparticles,[16,25,29-31] nanobelts,[32] nanowires,[33] nano-forests,[34] blocking layers,[35] and TiO_2−Nb_2O_5 bilayers[36,37] in DSSCs. Direct band gap excitation of mesoporous Nb_2O_5 modified by a Pt co-catalyst was able to efficiently produce H_2 with methanol as a sacrificial electron donor.[38] However, there have been no reports of the use of Nb_2O_5 in as a photoanode in DSPECs for solar fuel production and H_2 generation.

We report here a detailed study on H_2 evolution based on **RuP** as the sensitizer in orthorhombic Nb_2O_5 nanocrystalline films with the added reductive scavenger EDTA to evaluate its potential DSPEC applications. The system was systematically investigated and the properties-conduction band energy, trap-state distribution, electron transfer dynamics, current-voltage relationship, and H_2 evolution efficiency— were compared to the TiO_2 equivalent device.

2.2 Experimental Section

2.2.1 Materials

Aqueous solutions were prepared from water purified by a Milli-Q purification system. Lithium perchlorate (99.999 % trace metal basis), 70 % perchloric acid (99.999%), ethylenediaminetetraacetic acid (EDTA) disodium salt dehydrate (ACS reagent), titanium isopropoxide, isopropanol, hydroxypropyl cellulose (HPC), 2,4-pentaedione, and 1,8-

diazabicyclo[5.4.0]undec-7-ene(DBU,98 %) were used as received from Sigma-Aldrich. [**RuP**]Cl_2[39] were prepared according to previously published procedures.

2.2.2 **Photoanodes**

Anatase nanoTiO_2 films (thickness ~ 5.5 ± 1 μm) on top of 11 mm × 70 mm FTO (fluorine-doped SnO_2, sheet resistance 15 Ω/□, Hartford Glass Co. Inc.) slides were prepared according to reported literature procedures.[40,41] NanoNb_2O_5 films were prepared by a modified procedure.[41,42] Inside a glove box, 2 mL 2,4-pentaedione was mixed with 2.5 mL niobium ethoxide (Alfa Aesar). After stirring for 10 min, 20 mL ethanol was added. Outside the glove box, the mixture was further stirred at 50 ^{o}C for 30 min. The alkoxide solution was added in to a flask containing five drops of DBU and 18 mL of water, giving rise to a transparent yellow solution. The mixture was then concentrated by rotary evaporation to remove ethanol until the final volume reached 30 mL. Adding 30 mL Milli-Q water, solution was again reduced to 30 mL. Additional drops of DBU were added until the pH was ~ 9-10. The solution was then transferred to an autoclave bomb (Parr Instruments) and heated at 230 ^{o}C for 12 hours and cooled to room temperature. The resulting white-brown wet gel was ground using an agate mortar. An aqueous solution of HPC (Mw=100,000) was added to the gel to give 6 wt % Nb_2O_5 and 3 wt % HPC. After stirring for 3 days, as-prepared paste was doctor-bladed onto FTO glass by scotch tape to control thickness. The transparent Nb_2O_5/FTO slides with thickness ~3 μm or 5 μm were annealed at 600 ^{o}C for one hour before storage. Metal oxide/FTO photoanodes were derivatized by soaking in 200 μM **RuP** either in a 0.1 M $HClO_4$ aqueous solution or in water overnight, followed by soaking for an additional 12 h in 0.1 M $HClO_4$ or water to remove any possible **RuP** aggregates. Surface coverage (Γ in mol/cm^2) was determined by absorption measurements with

$\Gamma = A/\varepsilon/1000$,[43] with $\varepsilon_{(457nm)} = 13{,}700 \pm 120\ M^{-1}cm^{-1}$ at pH 1 $HClO_4$ and $15{,}100 \pm 300\ M^{-1}cm^{-1}$ in water.

Nb_2O_5/FTO samples were analyzed by powder X-ray diffraction (Rigaku Multiflex diffractometer in theta-two theta mode) using Cu K_α radiation (λ = 1.5418 Å). Morphology analysis was conducted by a Hitachi 4700 Field Emission scanning electron microscopy (FESEM), a JEM 100CX-II transmission electron microscope (TEM) and a JEOL 2010F FasTEM for HRTEM images. Absorptance measurements were conducted on a Cary50 UV-Vis spectrophotometer or a Cary 5000 UV-Vis-NIR spectrophotometer with a specular reflectance accessory for transmission and reflectance measurements. ZrO_2/FTO transparent electrodes were prepared according to previously-published procedures.[44]

2.2.3 Steady-State Emission

Emission spectra were recorded at room temperature by using an Edinburgh FLS920 spectrometer with the emitted light first passing through a 495 nm long-pass filter, then a single grating (1800 L/mm, 500 nm blaze) Czerny-Turner monochromator (5 nm bandwidth) and finally detected by a peltier-cooled Hamamatsu R2658P photomultiplier tube.

2.2.4 Transient Absorption (TA)

TA experiments were performed by using nanosecond laser pulses produced by a Spectra-Physics Quanta-Ray Lab-170 Nd:YAG laser combined with a VersaScan OPO (532 nm, 5-7 ns, operated at 1 Hz, beam diameter 1 cm) integrated into a commercially available Edinburgh LP920 laser flash photolysis spectrometer system. White light probe pulses generated by a pulsed 450 W Xe lamp were passed through the sample, focused into the spectrometer (3 nm bandwidth), then detected by a photomultiplier tube (Hamamatsu R928). Appropriate filters were placed before the detector to reject unwanted scattered light. Detector output was

processed by a Tektronix TDS3032C Digital Phosphor Oscilloscope interfaced to a PC running Edinburgh's software package. Single wavelength kinetic data were the result of averaging 50 - 100 laser shots and were fit with either Origin or Edinburgh software.

A three-arm, one-compartment photoelectrochemical (PEC) cell was employed in the transient absorption measurements with applied bias. A 395 nm long pass filter was positioned in front of the cell to preclude direct band gap excitation of the semiconductor. The arm for the photoanode was a 10 mm path length pyrex curvette. A platinum wire was used as photocathode and Ag/AgCl(BASi, MF-2079) as the reference electrode. The photoanode was inserted at a 45° angle into a homemade Teflon seat located in the cuvette. The photoanode was allowed to reach equilibrium with electrolyte for ~ 40 min before measurements. The background current was stabilized at the applied bias before laser excitation. All experiments were carried out under argon at 22 ± 2 ˚C unless otherwise specified. Current measurement and applied bias were performed on a PineWavenow potentialstat. All bias values were reported relative to the normal hydrogen electrode (NHE).

2.2.5 **Specelectrochemistry**

Spectroelectrochemical measurements, based on a procedure developed by Fitzmaurice,[45] were used to determine semiconductor conduction band edges. Applied potential measurements utilize a CH Instruments Model 601D Series Electrochemical Workstation (CHI) with nanoTiO_2 or nanoNb_2O_5/FTO as the working electrode, a platinum wire counter electrode and a Ag/AgCl reference electrode (BASi) in the three-arm PEC cell used in TA. After deaerating for 40 min with Argon, the measurements were performed in 0.1 M $HClO_4$ aqueous solution and in pH 4.5 lithium acetate/acetic acid buffer with 0.1 M $LiClO_4$. A 395 nm long pass filter was inserted in the path of spectrometer beam to prevent direct band gap excitation. The absorbance spectra of

samples were measured with an Agilent 8453 UV-visible diode array spectrophotometer that was interfaced with a CHI potentiostat. The digital output lines of the "Cell Control" port of the potentiostat were connected to the GPIO input lines of the spectrophotometer via a custom cable, allowing scans to be initiated via macro commands in the CHI software program. The bias potential applied to the sample slide was varied from +0.4 to -0.7 V vs. NHE at intervals of 5 mV. Following a 10 s period for equilibration of the sample, the spectrophotometer was triggered automatically to acquire a new scan at each applied potential.

Potential step chronoamperometry was used to study the transient current response under applied bias.[46] In each scan, nanoTiO_2 and nanoNb_2O_5 films were first equilibrated at 0.7 V (vs. NHE) for 5 min in pH13 NaOH solution that was pre-deaerated in argon for 30 min. The applied potential was shifted immediately to a preset bias followed by transient current decay recorded over a 10 s interval with a sampling time of 0.5 ms. The potential was shifted from -0.2 and then to -1.05 V vs NHE under control of the CHI potentiostat.

2.2.6 Steady state I-V measurements

Illumination was provided by a spectral light engine from Lumencor (λ_{max} = 445 nm, 20 nm bandwidth, output ~ 1-100 mW cm^{-2}). The light source was integrated with a Newport optical fiber and a focusing/imaging beam probe. The irradiation beam diameter was 10 mm. Photocurrents with applied bias were performed by a Wavenow potentiostat.

2.2.7 H_2 measurements

Photoelectrochemically evolved hydrogen was quantified by headspace gas analysis on a Varian 450-GC with a molecular sieve column and a PDHID detector. Gaseous samples (0.6 mL) were drawn from the headspace by a gas-tight 0.5 mL syringe (Vici) and injected into the GC. Calibration curve for H_2 was determined separately.

2.2.8 **Photo-stability studies**

Photostability measurements were performed by using a previously reported procedure.[47] The light from a Royal Blue (455 nm, FWHM ~30 nm, 475 mW/cm^2) Mounted High Power LED (Thorlabs, Inc., M455L2) powered by a T-Cube LED Driver (Thorlabs, Inc., LEDD1B) was focused to a 2.5 mm diameter spot size by a focusing beam probe (Newport Corp. 77646) outfitted with a second lens (Newport, Corp 41230). Light output was directed onto the derivatized thin films placed at 45° in a standard 10 mm path length cuvette containing 5 mL of the solutions of interest. The illumination spot was adjusted to coincide both with the thin films and the perpendicular beam path of a Varian Cary 50 UV-Vis spectrophotometer. The absorption spectrum (360-800 nm) of the film was obtained every 15 minutes during 16 hours of illumination. The incident light intensity was measured using a thermopile detector (Newport Corp 1918-C meter and 818P-020-12 detector). The solution temperature, 22 ± 2 °C, was consistent throughout the duration of the experiment.

2.3 Results and discussion

2.3.1 Structure

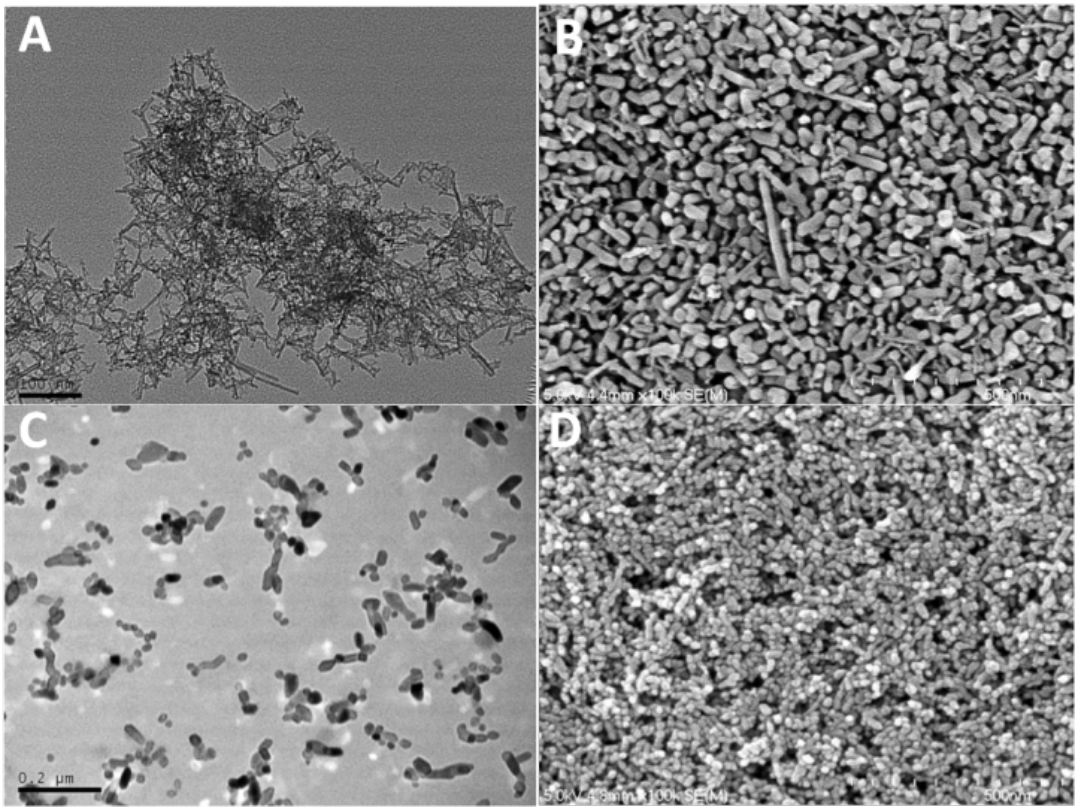

Figure 2-2. TEM image of a Nb_2O_5 monolith (A) and TiO_2 nanoparticles (C) after autoclaving at 230 °C for 12 hours and 210 °C for 13 hours respectively; FE-SEM image of nanoNb_2O_5 (B) and TiO_2/FTO (D) nanofilms annealed at 600 °C and 450 °C.

TEM images of Nb_2O_5 monoliths and TiO_2 nanoparticles after being autoclaved and FE-SEM images of Nb_2O_5 and TiO_2/FTO films after annealing are shown in Figure 2-2. For Nb_2O_5 there is a notable change in morphology between the autocalved monoliths (Figure 2-2A) and the annealed film (Figure 2-2B). The film is composed of a nanoporous network containing predominantly nanoparticles with a small amount of scattered rods, consistent with Lenzmann's earlier results.[42] The rod structures originate from the autoclaving process and nanoparticles

grow during the annealing process. In contrast, the size and shape of TiO_2 nanoparticles are maintained during the annealing process (Figure 2-2C and D).

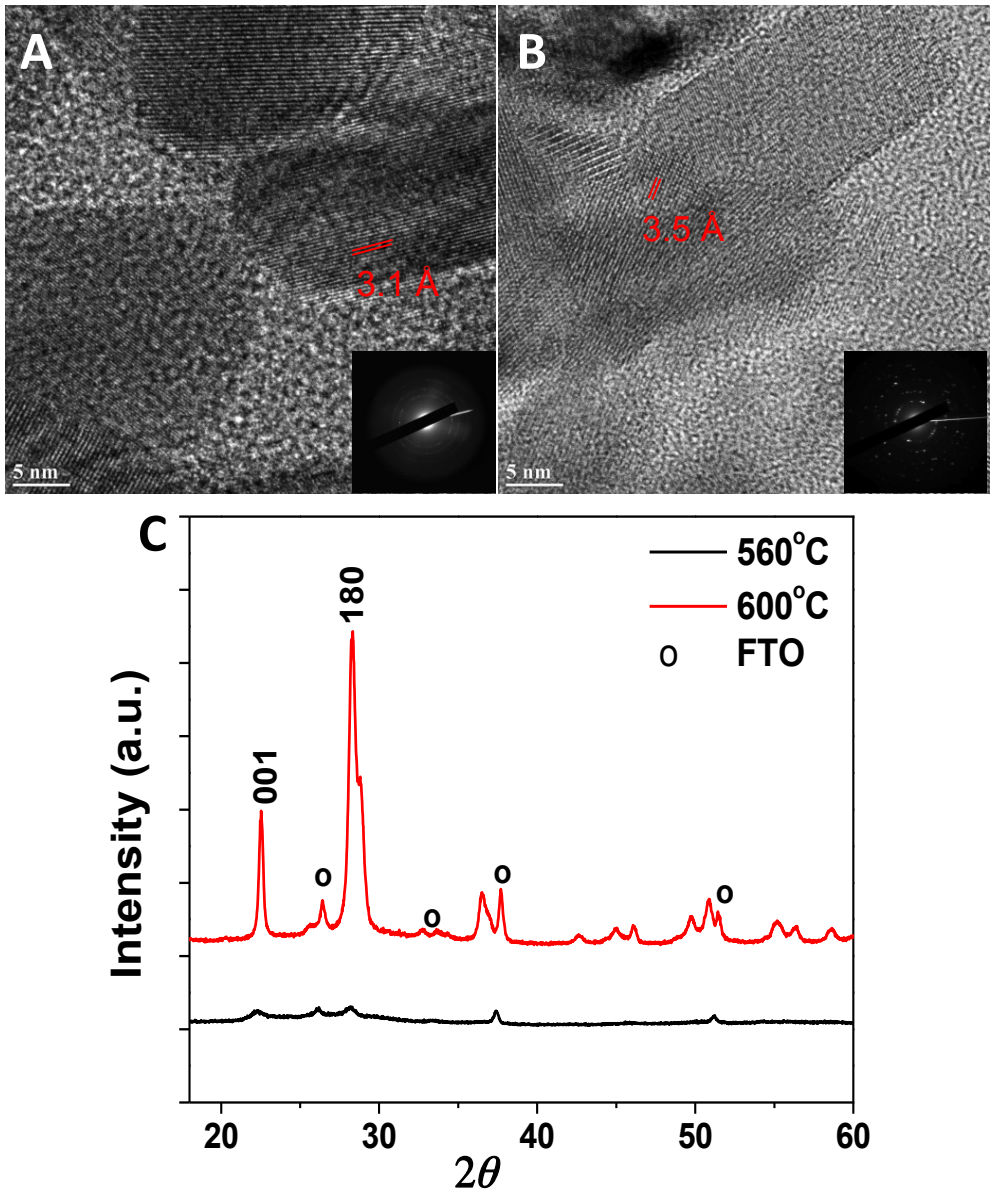

Figure 2-3. HRTEM of Nb_2O_5 (A) and TiO_2 (B) particles; C) XRD pattern of nanoNb_2O_5/FTO film annealed at 560 °C (black) and 600 °C (red).

The XRD pattern for nanoNb_2O_5/FTO films annealed at 560 °C and 600°C are shown in Figure 2-3C. The diffraction patterns indicate that the Nb_2O_5 film is dominated by the

orthorhombic T-phase (Pbam(55), JCPDS#27-1003 and #30-0873). Also in accord with Lenzmann's results, the film annealed at lower temperatures (560 °C) has reduced peak intensities due to the decreased crystallinity of the particles. [42] The Nb_2O_5 average particle size was determined by use of the Scherrer equation 2-1 .[48]

$$D \approx \frac{0.9\lambda}{\beta \cos\theta} \qquad (2\text{-}1)$$

In this equation, D is the average crystal thickness, λ is the x-ray wavelength, β is the full-width at half maximum intensity (FWHM) in radians, and θ is the Bragg angle. The average particle size in the Nb_2O_5/FTO films was found to be 30.7 nm. The HRTEM images of Nb_2O_5 (Figure 2-3A) and TiO_2 (Figure 2-3B) particles exhibit clear lattice fringes, consistent with highly crystalline samples after annealing. The interplanar spacing of 0.31 nm in Nb_2O_5 and 0.35 nm in TiO_2 closely correspond to the literature value of crystal planes (180) in orthorhombic Nb_2O_5[49] and (101) in anatase TiO_2[50] exposed on the crystal surfaces.

2.3.2 Band gap (E_g) and conduction band (E_{cb})

The absorbance spectrum of T-phase Nb_2O_5 and anatase TiO_2 films is shown in Figure 2-4A. The conduction band potential (E_g) was determined from a Tauc plot by using equation 2-2.[51] The optical band gap energy for Nb_2O_5 (3.30 eV) is larger than for anatase TiO_2 (3.22 eV). In equation 2-2, A is a constant; n = 1 for direct or n = 4 for indirect band gap semiconductors; α is the absorption coefficient; n = 4 used in the calculations here.

The absorption changes at 800 nm under applied potential can be seen in Figure 2-4B and C. E_{cb} was determined by spectroelectrochemical measurements, based on a procedure developed by Fitzmaurice. [45]

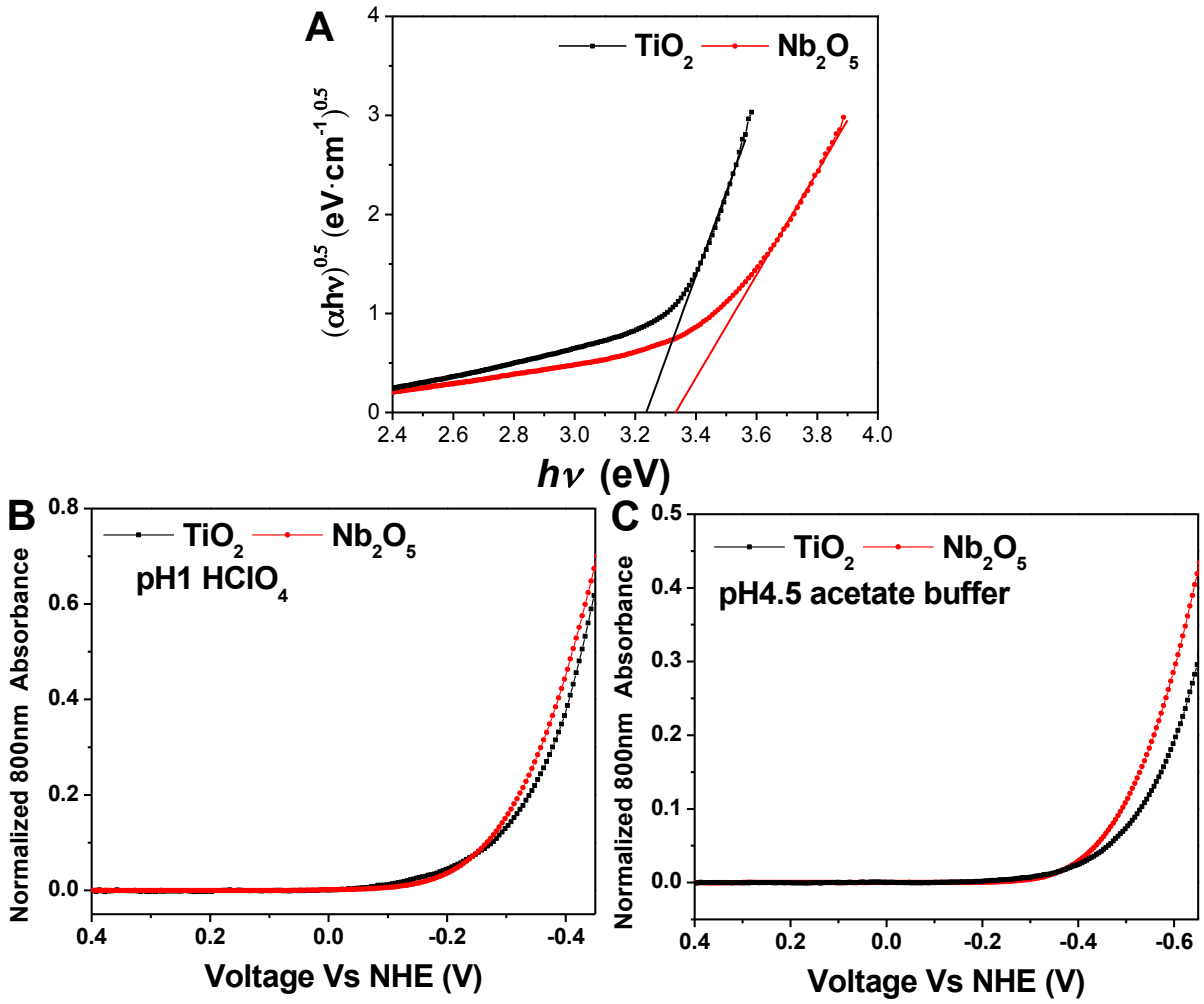

Figure 2-4. Tauc plots (A) and absorption changes at 800 nm as a function of applied potential in aqueous 0.1 M $HClO_4$ (B) in pH 4.5 0.1 M lithium acetate/acetic acid (LiOAc/HOAc), and (C) in 0.1 M $LiClO_4$ for nanoTiO_2 (-■-) and (-●-) for nanoNb_2O_5 in all graphs.

Based on these results, the conduction band for T-phase Nb_2O_5 is positively shifted (NHE scale) compared to anatase TiO_2 at both pH = 1 and pH = 4.5. The conduction band for Nb_2O_5 is ~ -0.23 V at pH 1 and -0.43 V at pH 4.5; and that for anatase TiO_2 films is ~ -0.27 V at pH 1 and -0.49 V at pH 4.5. According to Fitzmaurice,[52] the potential for TiO_2 is pH dependent with E_{cb} = -0.16 - 0.06pH (V/NHE) which gives E_{cb} = -0.22 V at pH 1 and -0.43 V (vs NHE) at pH 4.5. These calculated values are close to the measured results in Figure 4. Like TiO_2, Nb_2O_5

photoelectrodes follow a Nernstian shift in conduction band potential (~ 57 mV per pH unit).The differences in E_g and E_{cb} between these two metal oxides is small (< 0.1 eV) and any real differences blurred by measurement error.

$$\alpha = A\frac{(h\upsilon - E_g)^{n/2}}{h\upsilon} \qquad (2\text{-}2)$$

For comparison, the band edges for two pulsed laser deposited (PLD) thin oxide films (t-phase PLD-Nb_2O_5 and anatase PLD-TiO_2, thickness12 ± 3nm) have been determined by a combination of UPS, XPS and IPS (UV, X-ray and Inverse Photoemission Spectroscopy). Using this approach, the transport gap of the two oxides is found to be comparable, while the conduction band edge of PLD-Nb_2O_5 is found 0.1 eV above the conduction band of PLD-TiO_2, in good agreement with our results.[53]

These results are counter to previous reports which suggest that the conduction band energy of Nb_2O_5 is ~ 0.2 to 0.4 eV higher than TiO_2. There is a significant discrepancy between the results presented here and those previously reported. The discrepancy between conduction band potentials for Nb_2O_5 may be due to a combination of the crystal phase being studied, and the morphology of the films. For example, Viet et al. [33] reported E_{cb} to be ~ 0.8 eV higher for T-phase Nb_2O_5 electrospun nanofibers compared to TiO_2. For amorphous Nb_2O_5, a positive shift of ~ 0.2 eV was reported relative to nanocrystalline Nb_2O_5.[24] In general, in making comparisons of this kind, it is clear that attention must be paid to such variables as crystal structure, morphology, and defects. In any case, we conclude that the nanocrystalline T-phase Nb_2O_5 films prepared here have similar but slightly more positive E_{cb} values relative to anatase TiO_2.

2.3.3 **Trap state analysis**

Trap states also significantly influence n-type semiconductor behavior.[54-56] It has been proposed that trapped electrons in surface states are fully responsible for the optical response to bias. [57] However, Fitzmaurice et al.,[54] attribute the optical absorption spectrum in the near infrared mainly to conduction band electrons with a small contribution from trap states. Because of this, it is necessary to consider that the slightly more positive E_{cb} value for Nb_2O_5 could arise from the spectroelectrochemical response of trapped electrons in Nb_2O_5.

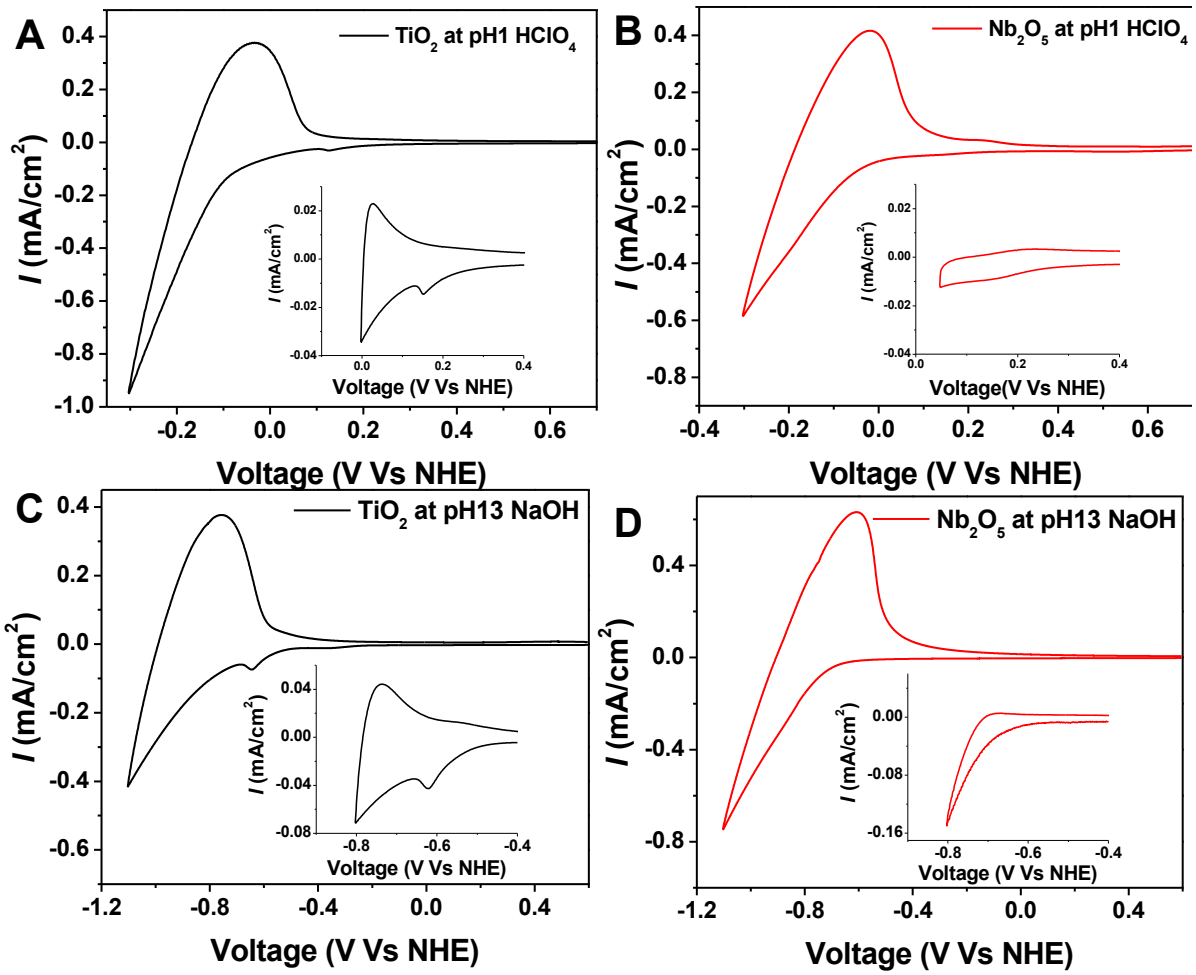

Figure 2-5. Cyclic voltammograms (CV) for TiO_2 (—) and Nb_2O_5 (—) in 0.1 M $HClO_4$ (A and B) and at 0.1 M NaOH (C and D) in aqueous solutions (100 mV/s). Insets: CVs with scan reversal before reaching the conduction band energy (50 mV/s).

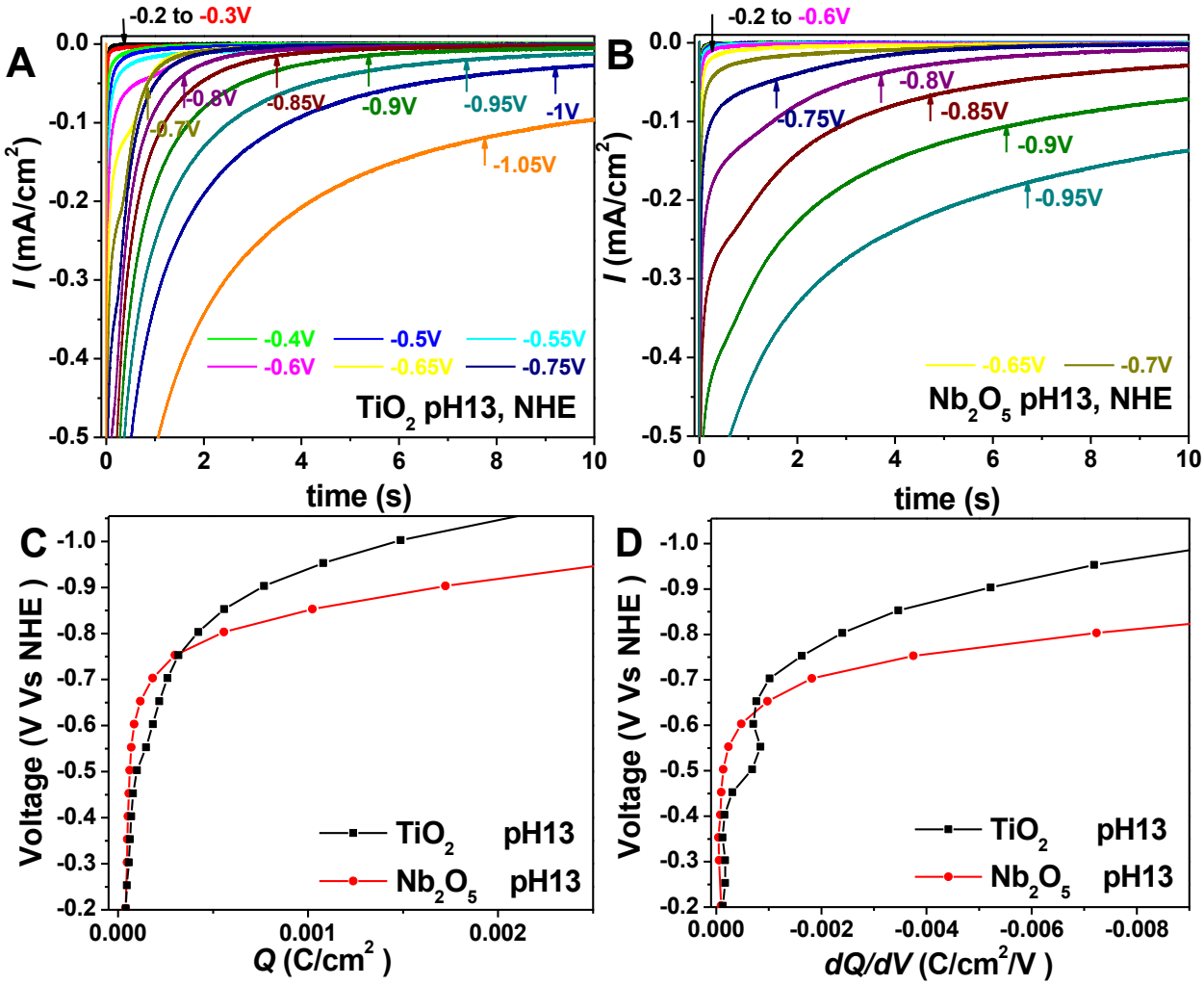

Figure 2-6.Transient current density decays obtained for TiO_2 (A) and Nb_2O_5 (B) electrodes at pH 13 (NaOH) by stepping the applied potential from -0.2 V to -1.05 V after equilibrating at 0.7 V for 5 min before each scan. C) Cathodic charge density accumulated and D) the first derivative of accumulated charge density for nanoTiO_2 (-■-) and nanoNb_2O_5 (-●-), respectively. All bias values are versus NHE and metal oxides are 5.5 ± 1 microns thick.

Cyclic voltammetry (CV) measurements for the two metal oxides at pH 1 and 13 are shown in Figure 2-5. In voltammograms of TiO_2, small reduction waves appear ~ 0.2 - 0.3 eV below the conduction band which are generally assigned to mono-energetic, deep trap states ($E_{me,trap}$).[52,58] Lindquist et al. [46] observe a CV wave with higher peak current under more basic

conditions in agreement with results obtained here (Figure 2-5A and C). The increased current is attributed to higher trap state densities in basic conditions. For Nb_2O_5, no such peaks were observed prior to the conduction band edge in pH 1 and pH 13 (Figure 2-5B and D). The absence of this wave can be attributed to a low concentration of band gap-localized deep traps, provided that exhaustion of trap energy level forming a local CV peak.[59]

Trap states were further investigated by using chronoamperometry (Figure 2-6A and B). In these experiments, transient current density decays for nanoTiO_2 and nanoNb_2O_5 at pH 13 were measured by first applying a positive bias (0.7 V vs NHE) to the electrodes for 5 min. The applied potential was then shifted to negative values ranging from -0.2 V to -1.05 V and the change in current was monitored for 10 seconds after the potential change. The total charge (Q)

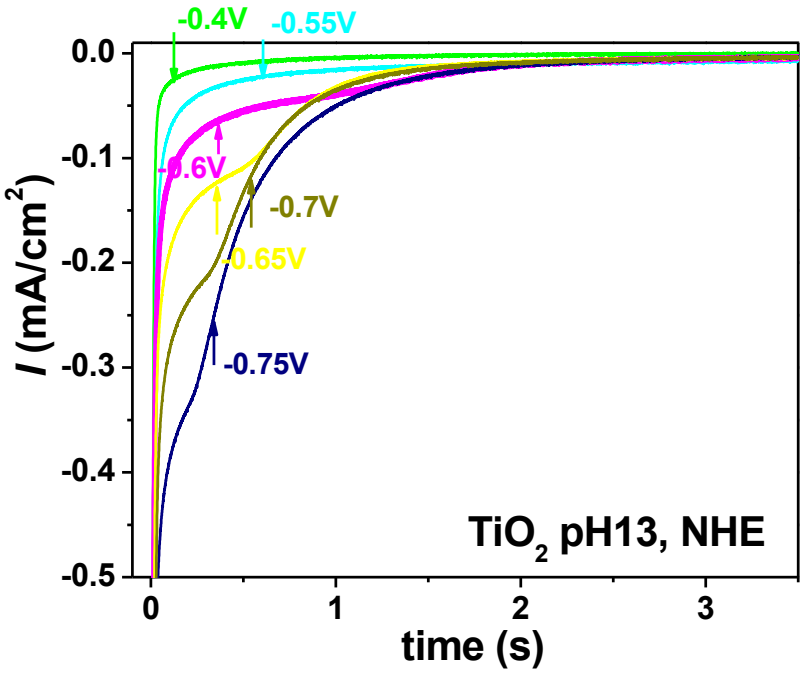

Figure 2-7.Transient current decay for nanoTiO_2 at pH 13 NaOH stepping from -0.2 to -0.75 V vs NHE after equilibrating at 0.7 V for 5 min.

passed during the decay was determined by integrating current density vs time curves in Figure 2-6A and 2-6B. Figure 2-6C shows the charge density per area (Q/cm^2) with respect to the applied bias V. Assuming that the trap density is proportional to dQ/dV,[46] Figure 2-6D depicts the trap state distribution as a function of applied potential for TiO_2 and Nb_2O_5 films at pH 13.

All current decay traces in Figure 2-6A and 2-6B display an initial sharp cathodic peak followed by a rapid decay within a few ms arising from capacitive charging of the film and FTO substrate. [60] For TiO_2 (Figure 2-6A and Figure 2-7.), when the potential is biased to -0.4 V, a second slow decay component appears at the onset of the CV pre-peak in Figure 5C. It arises from the onset of electron occupation of monoenergetic deep trap states. Increasing the bias more negatively between -0.55 and -0.6 V results in a plateau region in the middle of the fast and slow decays. A further increase in bias to -0.7 V leads to a shorter duration for the plateau region. These observations can be explained by assuming a Gaussian distribution of mono-energetic trap states, [46] as shown in Figure 2-6D. With this interpretation, trap state are low below -0.4 V with a short timescale for trap filling. Most mono-energetic traps are between -0.55 V and -0.6 V, requiring longer filling times. From -0.65 to -0.7 V, the trap filling time decreases due to a reduced trap state density. When the bias is shifted to -0.75 V, the plateau region time is reduced and total trap filling times increase. In parallel, accumulated charge (Figure 2-6C) and trap densities (Figure 2-6D) rise with an exponential onset consistent with electron occupation of another trap state region, ($E_{ex,trap}$). [61] These trap states have an exponential distribution tailing off below the conduction band. The kinetics for filling monoenergetic trap states is enhanced due to the higher driving force at more negative potentials.

For transient currents in nanoNb_2O_5 (Figure 2-6B.), there is no significant change in fast transient decay until the bias is scanned to between -0.6 and -0.65 V. Past this point, an

exponential growth with potential is triggered simultaneously with accumulated charge growth (Figure 6C), trap state densities rise, Figure 2-6D, and current density increase (Figure 2-5D). Based on the absence of a Gaussian trap density distribution and CV pre-peak, nanoNb_2O_5 appears to have mainly an exponential distribution of band tail traps with only a few mono-energetic trap states below -0.6 V.

Transient current decay measurements do not decay to zero within the measurement window with the potential shifted to -0.9 to -1 V for TiO_2 and to -0.8 to -0.9 V for Nb_2O_5. Recalling that the conduction band potential for TiO_2 is calculated to be -0.94 V at pH 13, these observations are consistent with E_{cb} values for nanoTiO_2 and nanoNb_2O_5 in the vicinity of -0.95 and -0.85 to within ± 50 mV, respectively. This conclusion is also consistent with the lower conduction band for T-phase Nb_2O_5 prepared here compared to anatase TiO_2 as a photoelectrode.

In summary, TiO_2 trap states appear to consist of deep trap $E_{me,trap}$ and band tail trap $E_{ex,trap}$ states. The dominant trap states in T-phase Nb_2O_5 are band tail trap states, $E_{ex,trap}$. This result is particularly important given that trap states can significantly influence n-type semiconductor behavior and device performance.[54-56]

2.3.4 Steady State Emission

The photo excitation-quenching-back electron transfer scheme for surface-bound **RuP** on metal oxide surfaces (M_xO_y, M_xO_y = nanoTiO_2 or nanoNb_2O_5) is depicted in Scheme 2-1. Following photoexcitation of **RuP**, there is a competition between electron injection (k_{inj}) and excited state decay by radiative (k_r) and nonradiative (k_{nr}) pathways. The injection electron in M_xO_y, then recombines with $\mathbf{Ru^{III}P}$ through back electron transfer (k_{bet}).

Steady-state emission spectra for **RuP** on nanoTiO_2 and nanoNb_2O_5 in aqueous 0.1 M $HClO_4$ are shown in Figure 2-8. The emission intensity on ZrO_2 is relatively high because, in

contrast to TiO_2, the conduction band potential (~ -1.4 V vs NHE, pH = 7[62]) is more negative than the excited state redox potential of **RuP** ($E^{o'}(Ru^{III/II}P^*)$~ -0.75 V) and electron injection does not occur.[63]

Scheme 2-1. Photo excitation-quenching-back electron transfer scheme for surface-bound RuP on metal oxide surfaces. (M_xO_y = nanoTiO_2 or nanoNb_2O_5)

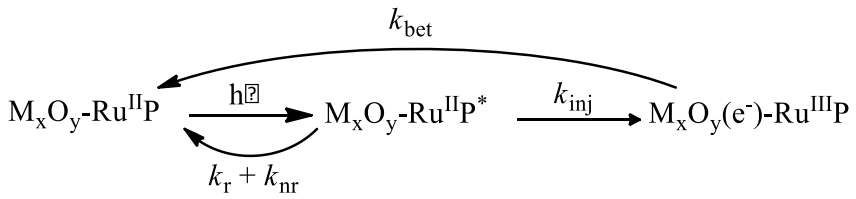

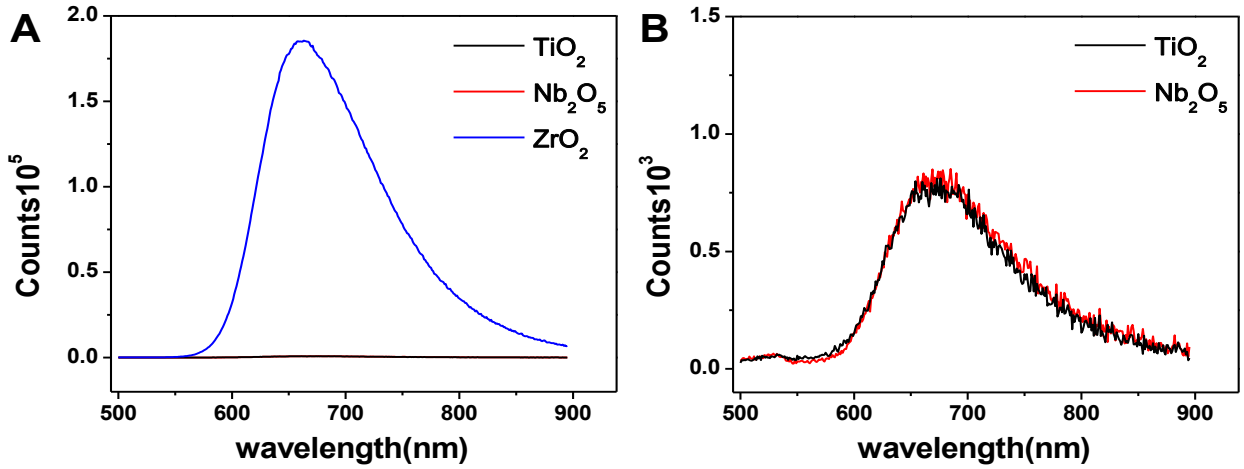

Figure 2-8.A: Emission spectra of RuP loaded nanoTiO_2, nano Nb_2O_5 and ZrO_2 in pH 1 $HClO_4$. B: Zoomed emission spectrum for TiO_2 and Nb_2O_5 in A.

2.3.5 Transient Absorption

Electron transfer dynamics for **RuP** on nanoTiO_2 and nanoNb_2O_5 films were investigated by nanosecond laser flash photolysis with excitation at 532 nm and monitoring at 400 nm. Absorbance-time traces for **RuP**-loaded nanoTiO_2 and nanoNb_2O_5 in pH 1 and pH 4.5 solutions are shown in Figure 2-9. The time-dependent amplitude decrease in OD to the baseline following

excitation is due to back electron transfer, $M_xO_y(e^-)$-**Ru^{III}P** → M_xO_y-**Ru^{II}P**, in Scheme 2-1. Absorbance-time decay traces could be successfully fit by the tri-exponential decay function in equation 2-3a. Weighted average lifetimes (<τ>) were calculated from equation 2-3b, and $t_{1/2}$, the time for half the total absorbance change to occur, from equation 2-3c.[13,64]

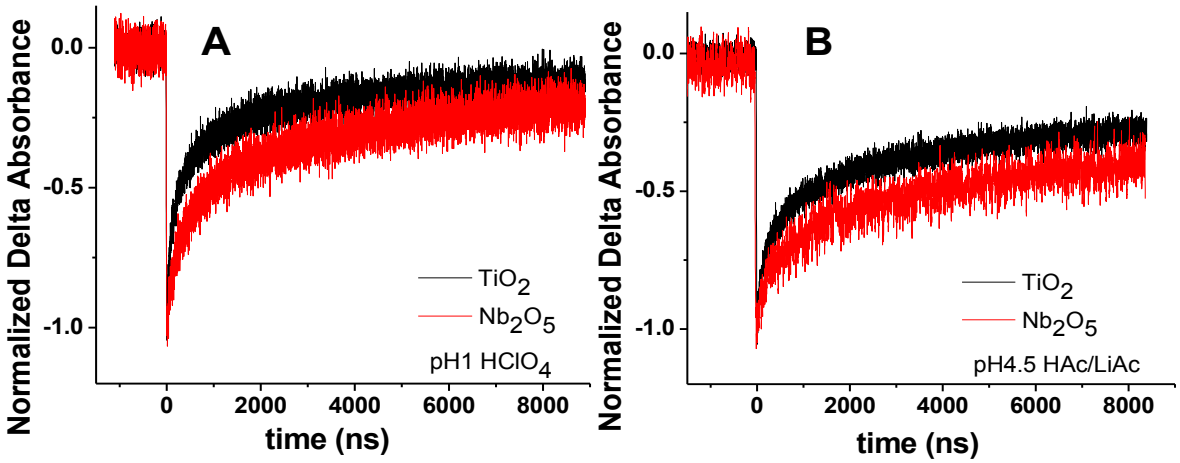

Figure 2-9.Time-resolved absorption traces of RuP-derivatized TiO_2 (black line) and Nb_2O_5 (red line) in argon deaerated 0.1 M $HClO_4$ (a) and in pH 4.5 LiAc/HAc with 0.1 M $LiClO_4$ (b) probed at 400 nm following 532 nm excitation. (Γ_{TiO2} = 1.93 × 10^{-8} and Γ_{Nb2O5} = 0.99 × 10^{-8} mol/cm^2/μm); (b) (Γ_{TiO2}= 2.01 × 10^{-8} and Γ_{Nb2O5}= 1.47 × 10^{-8} mol/cm^2/μm).

$$A = A_1 e^{-t/\tau_1} + A_2 e^{-t/\tau_2} + A_3 e^{-t/\tau_3} \tag{2-3a}$$

$$\tau_{ave} = \Sigma A_i \tau_i^{\,2} / \Sigma A_i \tau_i \tag{2-3b}$$

$$t_{1/2} = t \; at \; A_t = A_0/2 \tag{2-3c}$$

$$\Phi_{inj} = \frac{\dfrac{\Delta A_{sam}(\lambda_p)}{\Delta \varepsilon_{sam}(\lambda_p)}}{(1-10^{-A_{sam}(\lambda_{ex})}) \times [\dfrac{\dfrac{\Delta A_{ref}(\lambda_p)}{\Delta \varepsilon_{ref}(\lambda_p)}}{1-10^{-A_{ref}(\lambda_{ex})}}]} \tag{2-4}$$

where $\Delta A(\lambda_p)$ is transient absorption signal at probing wavelength (λ_p), $\Delta\varepsilon$ is the difference in molar extinction coefficient between ground and oxidized states and $A_{\lambda ex}$ is the absorbance of photoanode at the excitation wavelength (λ_{ex}). Laser excitation wavelength of TA was 532 nm in all cases. In this paper, reference is **RuP**/TiO_2 in 0.1 M $HClO_4$.

Electron injection yield for nanoNb_2O_5-**RuP** was determined by thin film actinometry with **RuP** on nanoTiO_2 in aqueous 0.1 M $HClO_4$ (Φ_{inj}= 100 %) as the reference.[65] Yields were calculated by using the change in molar absorptivity between ground and excited states, $\Delta\varepsilon_{(400nm)}$= -6500 $M^{-1}cm^{-1}$ and equation 2-4. [63] Injection yields, back electron transfer rate constants (k_{bet}), and half times ($t_{1/2}$) are summarized in Table 2-1.

Table 2-1. Injection yield and kinetic parameters for RuP on nanoTiO_2 and nanoNb_2O_5.

Oxide		ϕ_{inj} [a]	Lifetime (μs)				
			t_1 (A_1)	t_2 (A_2)	t_3 (A_3)	τ_{ave} [b]	$t_{1/2}$ [c]
TiO_2	pH1	1	0.09(42)	0.76(33)	10.97(26)	10.02	0.27
	pH4.5	-	0.11(28)	1.12(29)	19.22(43)	18.45	1.21
Nb_2O_5	pH1	0.6	0.17(28)	1.01(31)	11.97(41)	11.23	0.95
	pH4.5	-	0.11(16)	1.08(24)	19.71(60)	19.27	3.8

[a],[b],[c] are calculated by use of equation 2-4, 2-3b and 2-3c, respectively

$$\eta_{col} = \frac{n_{ex}}{e_{inj}} \tag{2-5a}$$

$$e_{inj} = \Phi_{inj} \times I_0 \times (1 - 10^{-A_\lambda}) \quad (2\text{-}5b)$$

Where η_{col} is the electron collection efficiency, n_{ex} is the number of electron passed by integrating current-time traces, e_{inj} is the number of injected electrons, Φ_{inj} is the injection yield, I_0 is the laser energy/pulse in Einstein and A_λ is the absorbance of photoanode at 532 nm, that is, laser excitation wavelength.

$$\Phi_{Fa} = \frac{2 \times n_{H_2}}{n_{ex}} \quad (2\text{-}6a)$$

$$\Phi_{H_2} = \frac{n_{H_2}}{I_0 \times (1 - 10^{-A_\lambda}) \times t} \quad (2\text{-}6b)$$

Where Φ_{Fa} is the Faradaic efficiency, n_{ex} is the number of electron passed during t min by integrating current-time profiles, and n_{H2} is the number of H_2 generated in t min, Φ_{H2} is the hydrogen quantum yield, I_0 is the incident light intensity at excitation wavelength (445 nm), A_λ is the photoelectrode absorbance at 445 nm excitation wavelength, and t is illumination time.

For nanoNb_2O_5 in 0.1 M aqueous $HClO_4$, the average injection yield from three different measurements was Φ_{inj} = 0.6. It is important to note that the injection yields reported here are lower limit estimates since they are limited by the instrument response time (~ 10 ns) which precludes observation of rapid back electron transfer events. For both nanoTiO_2 and nanoNb_2O_5, back electron transfer rates decrease as pH increases, consistent with previous observations.[64] Back electron transfer is noticeably more rapid on nanoTiO_2 than on nanoNb_2O_5 both at pH 1 and pH 4.5, a trend more discernible in the $t_{1/2}$ data.

2.3.6 Transient Absorption with EDTA

Adding irreversible reductive electron transfer scavengers (D) allows for reduction of **Ru^{III}P,** $M_xO_y(e^-)$-**Ru^{III}P** + D → M_xO_y (e^-)-**Ru^{II}P** + D_{ox} (M_xO_y = TiO_2 or Nb_2O_5) which is in competition with back electron transfer. Photo-injected electrons are then free to diffuse to the counter electrode for proton reduction at the cathode of photoelectrosynthesis cell.

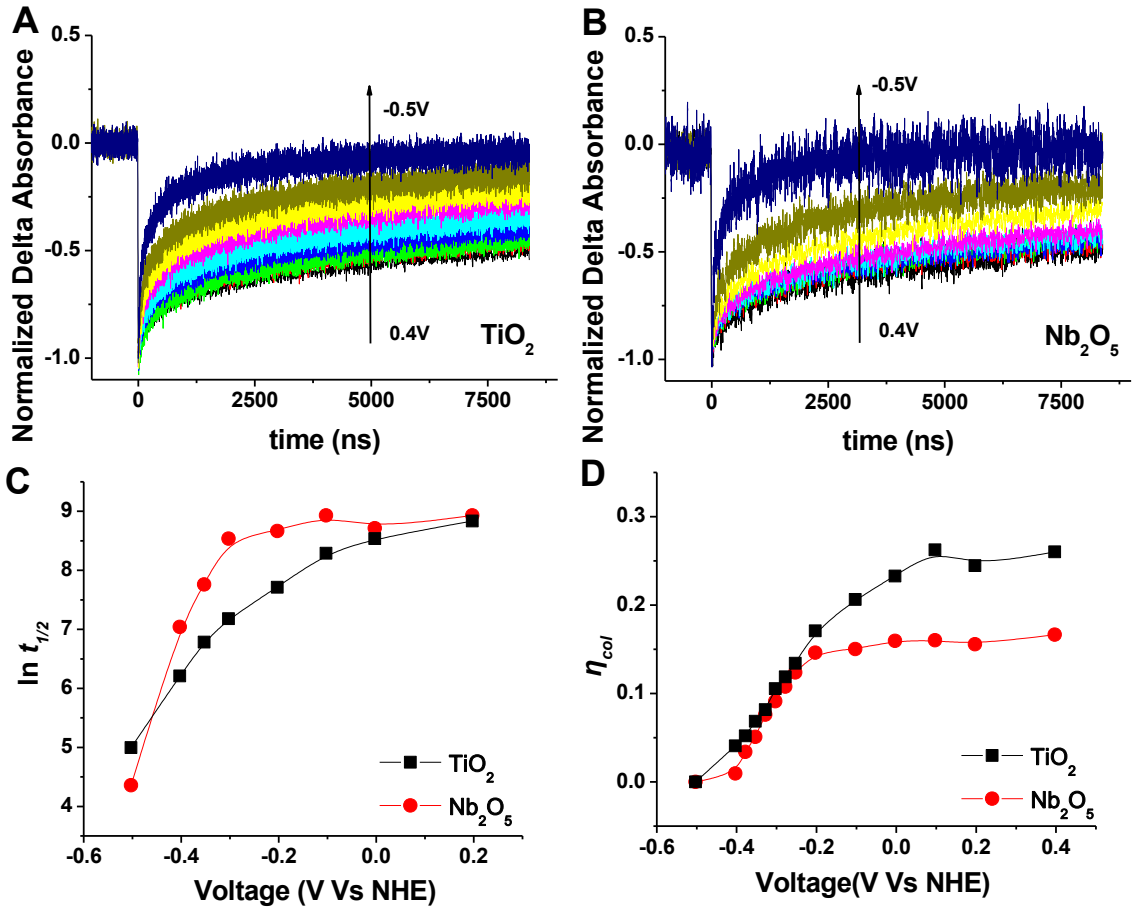

Figure 2-10. Transient absorbance-time traces for nanoTiO_2- RuP (A) and nanoNb_2O_5- RuP (B) as a function of applied bias in water with 20 mM added $EDTA^{4-}$ probed at 450 nm with 532 nm excitation. Half times for Ru^{II} P regeneration (C) and electron collection efficiencies (η_{col}) as a function of applied bias. $\Gamma_{TiO2} = 1.12 \times 10^{-8}$ and $\Gamma_{Nb2O5} = 0.57 \times 10^{-8}$ mol/cm^2/μm.

In these experiments, 20 mM aqueous EDTA solution in pH 4.5 was added. At this pH, EDTA is fully deprotonated and in the tetra-anionic form $EDTA^{4-}$ which is highly active toward reduction of **$Ru^{III}P$** due to its irreversibility and its electrostatic affinity for the oxidized chromophore.[13]

In Figure 2-10A and Figure 2-10B are shown the absorbance-time traces for nanoTiO_2-**RuP** and nanoNb_2O_5-**RuP** as a function of applied potential in aqueous solutions with 20 mM $EDTA^{4-}$. The natural log of $t_{1/2}$ for **$Ru^{II}P$** regeneration as a function of applied bias is shown in **Figure 2-10**C. Transient photocurrent measurements during laser flash photolysis were recorded simultaneously to determine the electron collection efficiency (η_{col}) by equation 2-5, assuming $\Phi_{inj} = 1$ for TiO_2 and 0.6 for Nb_2O_5 at pH 4.5. The variation of η_{col} with applied bias is shown in Figure 2-10D.

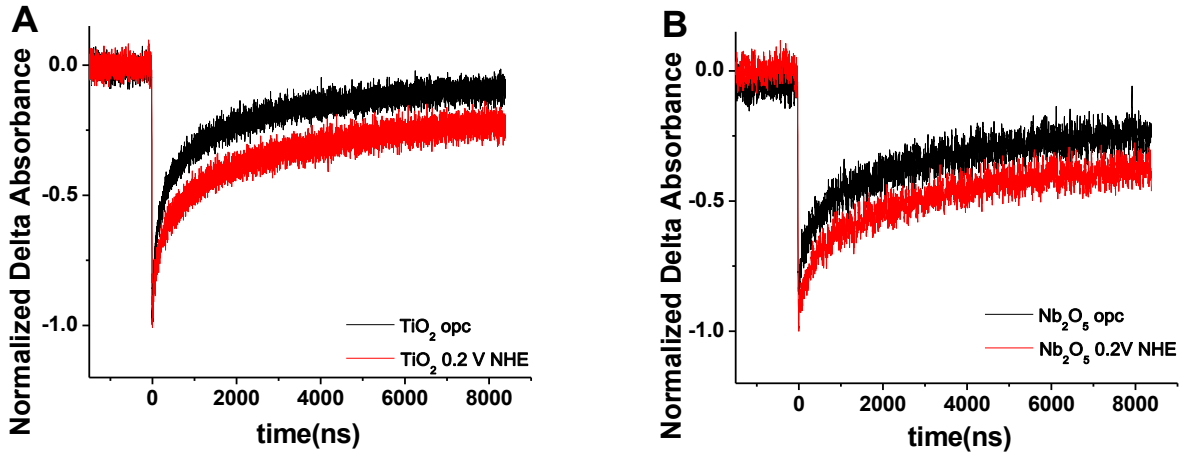

Figure 2-11. Transient absorption-time traces following excitation of nanoTiO_2-RuP (A) and nanoNb_2O_5-RuP (B) in the presence of 20 mM $EDTA^{4-}$ at pH 4.5 (λ_{ex} = 532 nm, probed at 400 nm). open circuit (black); 0.2 V bias (red) vs NHE. Slides were loaded in pH 1 $HClO_4$.

As noted above, at an appropriate applied bias, injected electrons are able to escape the metal oxide into the external circuit with H^+ reduction to H_2 at the Pt cathode. As shown in

Figure 2-11, there is a marked reduction in **Ru^{II}P** regeneration rate under closed-circuit conditions (0.2 V) for both TiO_2 and Nb_2O_5. In the absence of the irreversible electron donor/scavenger, the photocurrents are negligible as shown in transient current time traces with and without added $EDTA^{4-}$(Figure 2-12).

In the presence of $EDTA^{4-}$, both the $t_{1/2}$ (Figure 2-10C) and electron collection efficiency (Figure 2-10D) reach a plateau with onsets at ~ 0.1 V (nanoTiO2) and ~ -0.2 V (nanoNb_2O_5). At these potentials M_xO_y(e)-**Ru^{III}P** recombination was minimized and η_{col} was maximized (Figure 2-10D). Biasing the potential more negatively enhances the back electron transfer rate resulting in a decrease in electron collection efficiency. For both nanoTiO_2-**RuP** (Figure 8A) and nanoNb_2O_5-**RuP** (Figure 2-10B) there is a notable decrease in **Ru^{III}P** lifetime as the applied potential is decreased from 0.4 V to -0.6 V. This trend can most clearly be seen in Figure 2-10C. The Ru^{II}P regeneration rate for nanoNb_2O_5 is slower than for nanoTiO_2 from 0 to -0.4 V.

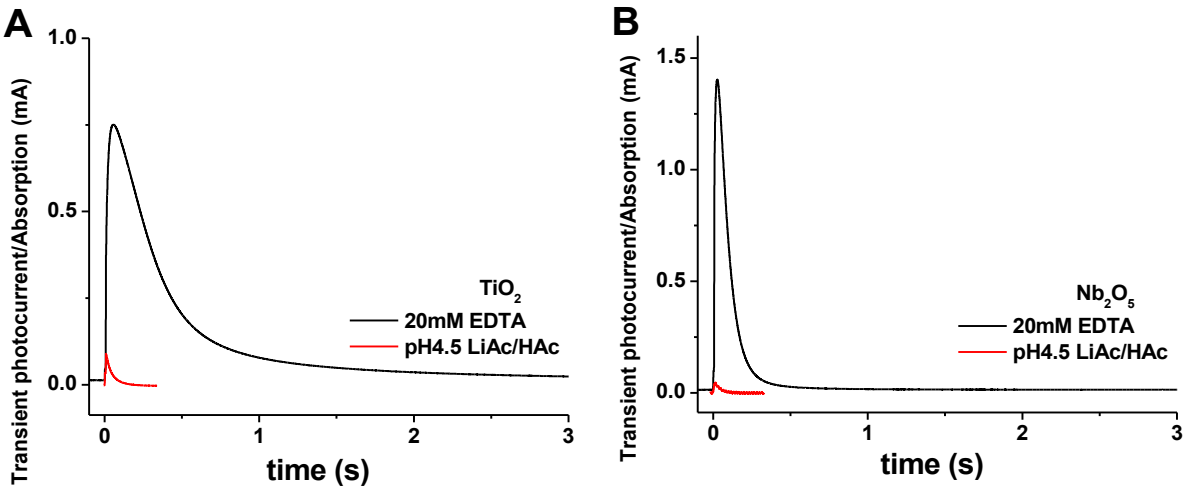

Figure 2-12.Transient photocurrent-time traces following excitation of nanoTiO_2-RuP (A) and nanoNb_2O_5-RuP (B) in the presence of 20 mM $EDTA^{4-}$ at pH 4.5 (λ_{ex} = 532 nm, probed at 400 nm, 0.2 V bias (red) vs NHE). Slides were loaded in pH 1 $HClO_4$.

2.3.7 Steady state photocurrent-voltage measurements

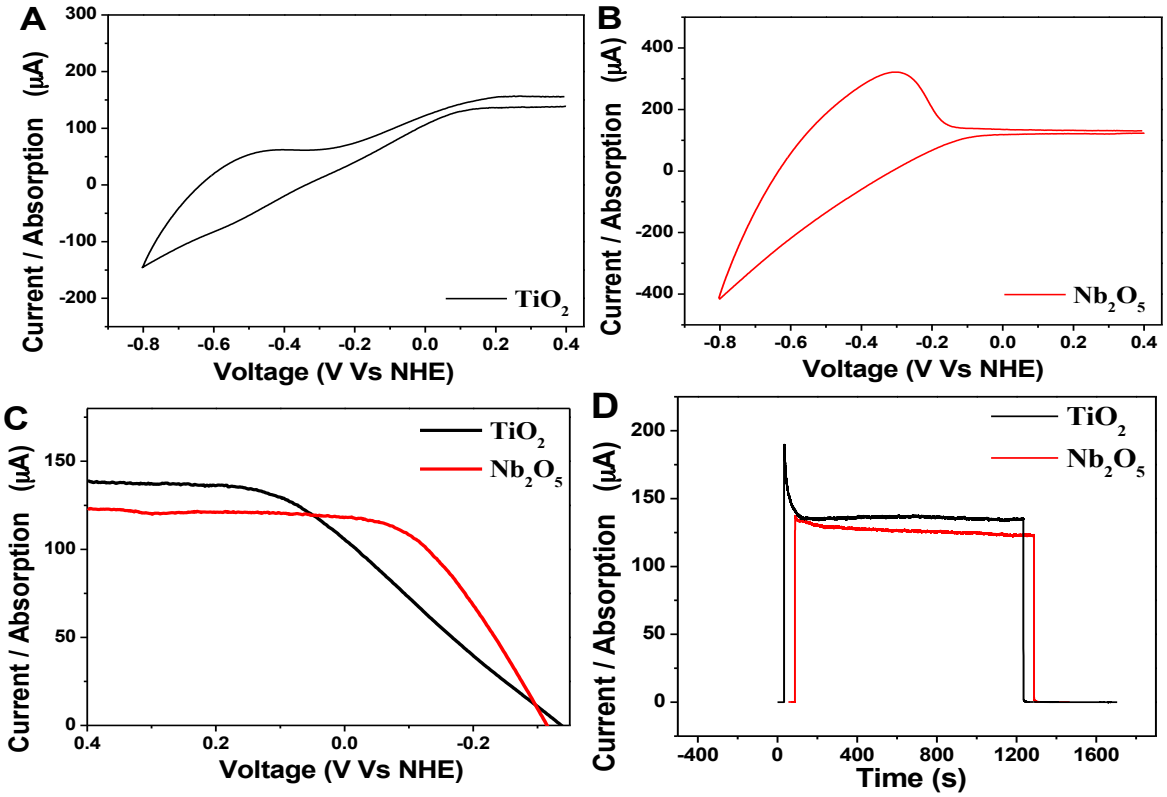

Figure 2-13. CV curves for nanoTiO_2- RuP (—) (A) and nanoNb_2O_5- RuP (—) (B) under 445 nm steady state illumination in 20 mM $EDTA^{4-}$ aqueous solution at a scan rate of 2 mV/s; (C) an enlarged region of the I-V curves in A and B; (D) photocurrent-time traces obtained within 20 min under an applied bias of 0.2 V vs NHE. In all graphs, photocurrents are normalized for absorbance. Light intensity (1.2 mW). $\Gamma_{TiO2} = 1.13 \times 10^{-8}$ and $\Gamma_{Nb2O5} = 0.42 \times 10^{-8}$ mol/cm^2/μm.

CV profiles for nanoTiO_2- **RuP** and nanoNb_2O_5- **RuP** in 20 mM $EDTA^{4-}$ aqueous solutions under 445 nm steady state illuminations are shown in Figure 2-13A. Steady state photocurrents vary with applied bias in agreement with the dependence of $t_{1/2}$ on bias and with the dependence of the electron collection efficiency on bias shown in (Figure 2-10C and Figure 2-10D). The significant cathodic photocurrents in the I-V profiles reach limiting values at an onset of ~ 0.1 V (NHE, TiO_2) and ~ -0.1 V (NHE, Nb_2O_5) with added $EDTA^{4-}$. The small

departure from this onset in the transient absorption measurements (Figure 2-13C and Figure 2-10D) is because of more accurate sampling in the CV profile with a scan rate 2 mV/s. The expanded I-V curve in Figure 2-13C clearly points to a greater fill factor and more positive V_{oc} for nano Nb_2O_5-RuP compared to nanoTiO_2-RuP.

In order to maximize photocurrent for proton reduction, cells were operated under an applied bias of 0.2 V (vs NHE). Photocurrent-time traces for the nanoTiO_2 and nanoNb_2O_5 DSPECs under steady state illumination for 20 min are shown in Figure 2-13D. Evolved hydrogen was measured by quantitative gas chromatography (GC). The Voc, electron collection efficiency (η_{col}), Faradaic efficiency (Φ_{Fa}), and H_2 quantum yields (Φ_{H2}) for both devices are summarized in Table 2-2.

Table 2-2. Summary of DSPEC parameters for nanoNb_2O_5- RuP and nanoTiO_2- RuP in 20 mM $EDTA^{4-}$ aqueous solution under steady state (445 nm) illumination for 20 min independent experiments.

oxide	V_{oc} (V, NHE)[a]	ϕ_{inj}[b]	η_{col}[c]	ϕ_{Fa}[d]	ϕ_{H_2}[e]
TiO_2	-0.38	1	0.33	1	0.16
Nb_2O_5	-0.34	0.6	0.47	1	0.15

[a] open circuit voltage (V_{oc}); [b] in pH 1 $HClO_4$; [c,d,e] are calculated according to equation 2-5 and 2-6. Results are from three independent experiments.

The V_{oc} for the nanoTiO_2-based device was slightly larger than for nanoNb_2O_5 with a difference ~ 40 mV. This trend is consistent with the within 0.1 V more negative conduction band potential of TiO_2 (vs. NHE) found in the above sections.

Contrary to the results in Figure 2-10D, the nanoNb_2O_5 films had a higher electron collection efficiency (η_{col} = 44 %), than nanoTiO_2 (η_{col} = 33 %) under steady state illumination. The origin of the difference is unclear but may arise from errors in measuring the laser intensity over the long periods required to collect the data. A higher η_{col} for Nb_2O_5 is expected because of the slower back electron transfer rate for $Nb_2O_5(e^-)$-**Ru^{III}P**.

H_2 quantum yields for nanoNb_2O_5-**RuP** (Φ_{H2} = 0.16) is comparable to those found for nanoTiO_2-**RuP** (Φ_{H2} = 0.15). The similarities in overall hydrogen production suggest that Nb_2O_5 is viable alternative to TiO_2 in DSPEC applications.

2.3.8 **Photostability**

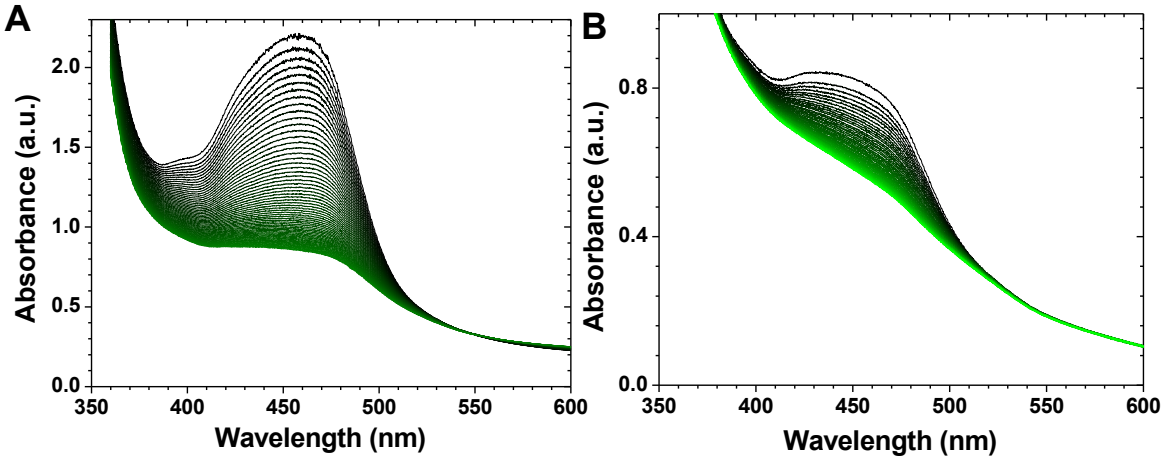

Figure 2-14. Absorption-time changes for RuP on (A) nanoTiO_2 and (B) nanoNb_2O_5 in 0.1 M $HClO_4$ under irradiation (475 mW/cm^2). (0 (black) to 16 hours (green) every 15 minutes).

Photostabilities of **RuP** on nanoTiO_2 and nanoNb_2O_5 in aqueous 0.1 M $HClO_4$ were evaluated by using a previously published procedure with constant irradiation at 455 nm

(FWHM ~ 30 nm, 475 mW/cm^2).[47] A gradual decrease in absorbance from 400- 490 nm is observed for both nanoNb_2O_5-**RuP** and nanoTiO_2-**RuP**. The loss in metal-to-ligand charge transfer (MLCT) absorption is consistent with desorption of **RuP** from the surface (Figure 2-14). Absorption-time traces at 480 nm could be satisfactorily fit to the biexponential function in equation 2-7a with a weighted average rate constant for desorption, k_{des}, defined in equation 2-7b.

$$\mathrm{A} = A_1 e^{-k_1 t} + A_2 e^{-k_2 t} \qquad (2\text{-}7a)$$

$$1/k_{des} = <\tau> = \Sigma A_i \tau_i^{\,2} / \Sigma A_i \tau_i \qquad (2\text{-}7b)$$

The k_{des} value from this analysis for nanoNb_2O_5-**RuP** (4.7×10^{-5} s^{-1}) is within experimental error of k_{des} for nanoTiO_2-**RuP** (5.0×10^{-5} s^{-1}) under the same conditions showing that surface photostability on nanoNb_2O_5 is comparable to that on nanoTiO_2. The comparable photostability of **RuP** on nanoTiO_2 and nanoNb_2O_5 is important for the use of Nb_2O_5 as photoanodes in DSSC and DSPEC applications.

2.3.9 Comparisons

As discussed above, compared to anatase TiO_2, **RuP** derivatized T-phase Nb_2O_5 is shown to have a lower electron injection yield and slower back electron transfer rate. In the literature, Nb_2O_5 has been considered to be a high conduction band material and used as a blocking layer to slow injected electron-hole recombination and increase photocurrents on TiO_2 and ZnO photoanodes.[29,36,66,67] Depending on excited state energetics, a higher energy conduction band could account for a lower electron injection yield due to a reduced driving force for injection. However, our results show that the conduction band for T-phase Nb_2O_5 is slightly more positive than TiO_2 and the electron injection results seem to be contradictory.

Scheme 2-2. Summary of energy diagram and interfacial kinetic processes dictating the performance of DSPECs for H_2 production for nanoNb_2O_5-RuP and nanoTiO_2-RuP.

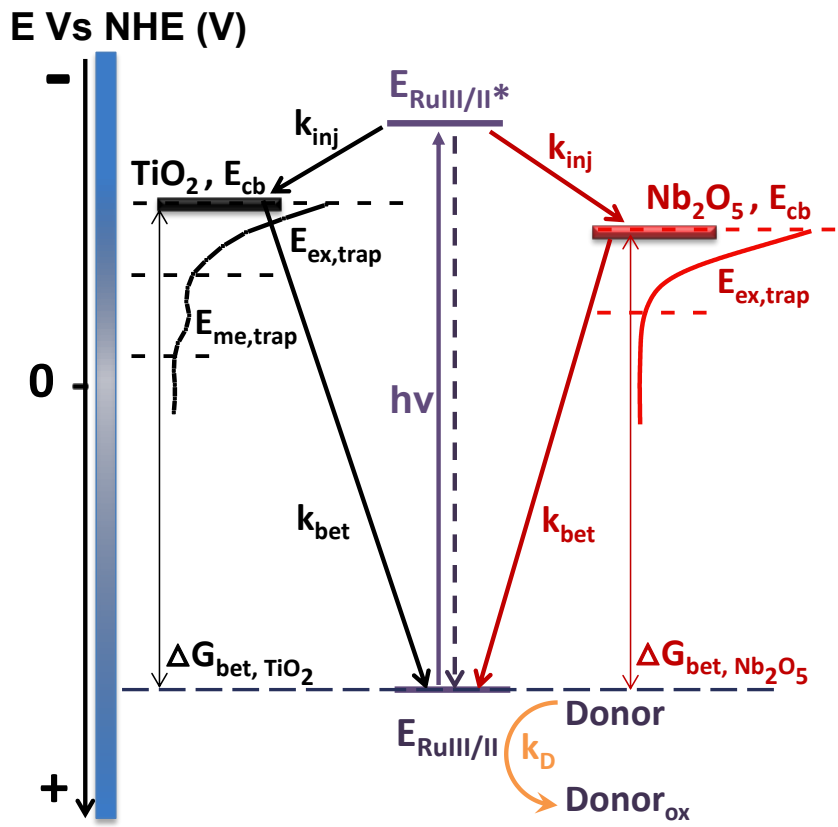

Photoanode:

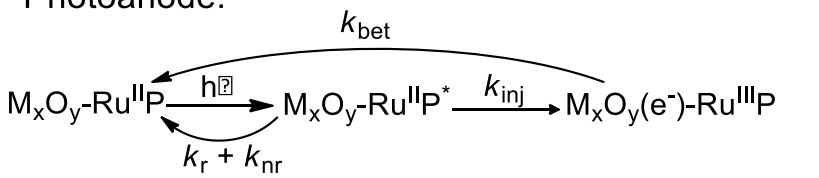

$$2M_xO_y(e^-)\text{-}Ru^{III}P + EDTA \xrightarrow{k_D} 2M_xO_y\text{-}Ru^{II}P + EDTA_{ox}$$

Photocathode:

$$2M_xO_y(e^-) + 2H^+ \xrightarrow{Pt,\ k_{H_2}} H_2 \qquad \text{where } M_xO_y = TiO_2 \text{ or } Nb_2O_5$$

The energy level diagram and major kinetic processes M_xO_y-**RuP** are depicted in Scheme 2-2. Electron injection into nanoTiO_2 and nanoNb_2O_5 from Ru(^{II}) polypyridyl dyes are known to

exhibit biphasic kinetics.[41] There is an ultrafast injection component (< 100 fs) arising from non-equilibrated excited states which is similar for both oxides and a slow component (< ns) that appears to be trap state dependent. In our transient experiments electron injection and sub-nanosecond recombination processes are not resolvable due to the 10 ns response time of the apparatus. Injection followed by a sub-nsec back electron transfer component, $Nb_2O_5(e^-)$-**Ru^{III}P** → Nb_2O_5-**Ru^{II}P**, involving shallow trap-states, could explain the decreased injection yield relative to nanoTiO_2.

Based on the trap state analysis above (also in Scheme 2-1), TiO_2 has a wide distribution of trap states that includes deep trap $E_{me,trap}$ states and band tail trap $E_{ex,trap}$ states. In T-phase Nb_2O_5 trap states are dominated by shallow band tail trap states, $E_{ex,trap}$. Assuming that surface state mediated recombination is small and that the majority of injected electrons are populated in traps, an electron must be thermally excited from a trap state into the conduction band to reach a recombination center, at least when trap densities are high.[61,68] In anatase nanoTiO_2, with a wide trap distribution, the timescale for injected electrons to be trapped and detrapped into the conduction band is assumed to be relatively slow. In nanoNb_2O_5, even if electron injection rate is rapid due to a slightly lower conduction band, a fast component for back electron transfer beyond our nanosecond TA capability may exist in due to trapping-detrapping processes as described above. In nanoNb_2O_5, even if electron injection rate is rapid due to a slightly lower conduction band, a fast component for back electron transfer beyond our nanosecond TA capability may exist. With this consideration and the observation of significantly quenched emission for nanoNb_2O_5-**RuP***, the actual electron injection efficiency might be similar for two metal oxides.

It is notable that nanoNb_2O_5 features an approximately three fold decrease in back electron transfer rate on the nsec timescale compared to TiO_2. This is presumably due to a

decrease in electronic coupling to the surface, an enhanced interfacial barrier to back electron transfer, or a combination of the two. Amorphous $Nb_2O_5.nH_2O$ is known to have both Brønsted and Lewis acid sites on its surface and is commonly used as heterogeneous acid catalyst.[69,70] These sites may have a high affinity for injected electrons contributing to the slow component for back electron transfer. The comparisons made here are independent of surface loading and the thicknesses of the oxide films (data not shown).

With $EDTA^{4-}$, a competition for $\mathbf{Ru^{II}P}$ regeneration exists between back electron transfer (k_{bet}) and $\mathbf{Ru^{III}P}$ reduction by EDTA (k_D). For both metal oxides, applying a negative bias fills trap states causing injected electrons to be trapped at increasingly shallow trap states. This effect is the origin of the enhancement in k_{bet} as a function of bias and is consistent with the experimental results in Figure 2-10.

2.4 Conclusions

A systematic, integrated experimental analysis of **RuP**-derivatized Nb_2O_5 and TiO_2 nanoparticle films in a DSPEC application has been conducted. The results of the study are important in gauging the potential use of Nb_2O_5 as an alternate photoanode material in photoelectrochemical applications. The particular goal of the current study was to exploit the reported higher conduction band potential of Nb_2O_5 in DSPEC applications. The results of a variety of experiments — conduction band potential, trap state distribution, transient absorption, steady state I-V, and photoelectroelectrochemical H_2 production — are integrated to establish a protocol for comparing metal oxide materials in a general way for possible photoanode applications.

In contrast to the generally accepted, higher conduction band potential for Nb_2O_5, we find that for a T-phase orthorhombic Nb_2O_5 nanocrystalline film, the conduction band potential

is slightly positive (< 0.1 eV) of that for anatase TiO_2. Experimental measurements on anatase TiO_2 demonstrate a wide distribution of trap states including deep trap and band tail trap states. T-phase Nb_2O_5 is dominated by shallow band tail trap states. Trap state distributions, conduction band energies, and interfacial barriers appear to contribute to a slower back electron transfer rate, lower injection yield on the nsec timescale, and a lower V_{oc} for T-phase Nb_2O_5 compared to anatase TiO_2. In an operating proton reduction DSPEC, with EDTA as a reductive scavenger, H_2 quantum yield and photostability measurements show that Nb_2O_5 is comparable to TiO_2.

2.5 REFERENCES

(1) O'Regan, B.; Gratzel, M. *Nature* **1991**, *353*, 737.

(2) Yum, J.-H.; Baranoff, E.; Kessler, F.; Moehl, T.; Ahmad, S.; Bessho, T.; Marchioro, A.; Ghadiri, E.; Moser, J.-E.; Yi, C.; Nazeeruddin, M. K.; Grätzel, M. *Nat. Commun.* **2012**, *3*, 631.

(3) Chen, C.-Y.; Wang, M.; Li, J.-Y.; Pootrakulchote, N.; Alibabaei, L.; Ngoc-le, C.-h.; Decoppet, J.-D.; Tsai, J.-H.; Grätzel, C.; Wu, C.-G.; Zakeeruddin, S. M.; Grätzel, M. *ACS Nano* **2009**, *3*, 3103.

(4) Grätzel, M. *Inorg. Chem.* **2005**, *44*, 6841.

(5) Hagfeldt, A.; Boschloo, G.; Sun, L.; Kloo, L.; Pettersson, H. *Chem. Rev.* **2010**, *110*, 6595.

(6) Treadway, J. A.; Moss, J. A.; Meyer, T. J. *Inorg. Chem.* **1999**, *38*, 4386.

(7) Alstrum-Acevedo, J. H.; Brennaman, M. K.; Meyer, T. J. *Inorg. Chem.* **2005**, *44*, 6802.

(8) Concepcion, J. J.; Jurss, J. W.; Brennaman, M. K.; Hoertz, P. G.; Patrocinio, A. O. v. T.; Murakami Iha, N. Y.; Templeton, J. L.; Meyer, T. J. *Acc. Chem. Res.* **2009**, *42*, 1954.

(9) Gagliardi, C. J.; Westlake, B. C.; Kent, C. A.; Paul, J. J.; Papanikolas, J. M.; Meyer, T. J. *Coord. Chem. Rev.* **2010**, *254*, 2459.

(10) Desilvestro, J.; Graetzel, M.; Kavan, L.; Moser, J.; Augustynski, J. *J. Am. Chem. Soc.* **1985**, *107*, 2988.

(11) Youngblood, W. J.; Lee, S.-H. A.; Kobayashi, Y.; Hernandez-Pagan, E. A.; Hoertz, P. G.; Moore, T. A.; Moore, A. L.; Gust, D.; Mallouk, T. E. *J. Am. Chem. Soc.* **2009**, *131*, 926.

(12) Zhao, Y.; Swierk, J. R.; Megiatto, J. D.; Sherman, B.; Youngblood, W. J.; Qin, D.; Lentz, D. M.; Moore, A. L.; Moore, T. A.; Gust, D.; Mallouk, T. E. *Proc. Natl. Acad. Sci. USA* **2012**.

(13) Song, W.; Brennaman, M. K.; Concepcion, J. J.; Jurss, J. W.; Hoertz, P. G.; Luo, H.; Chen, C.; Hanson, K.; Meyer, T. J. *J. Phys. Chem. C* **2011**, *115*, 7081.

(14) Jose, R.; Thavasi, V.; Ramakrishna, S. *J. Am. Ceram. Soc.* **2009**, *92*, 289.

(15) Sayama, K.; Arakawa, H.; Domen, K. *Catal. Today* **1996**, *28*, 175.

(16) Lenzmann, F.; Krueger, J.; Burnside, S.; Brooks, K.; Grätzel, M.; Gal, D.; Rühle, S.; Cahen, D. *J. Phys. Chem. B* **2001**, *105*, 6347.

(17) Maruska, H. P.; Ghosh, A. K. *Solar Energy* **1978**, *20*, 443.

(18) Scaife, D. E. *Solar Energy* **1980**, *25*, 41.

(19) Sayama, K.; Sugihara, H.; Arakawa, H. *Chem. Mat.* **1998**, *10*, 3825.

(20) *Light, Water, Hydrogen: The Solar Generation of Hydrogen by Water Photoelectrolysis*; Grimes, C. A.; Varghese, O. K.; Ranjan, S., Eds.; Springer: New York, 2007.

(21) Chen, X.; Shen, S.; Guo, L.; Mao, S. S. *Chem. Rev.* **2010**, *110*, 6503.

(22) Prado, A. G. S.; Bolzon, L. B.; Pedroso, C. P.; Moura, A. O.; Costa, L. L. *Appl. Catal. B.* **2008**, *82*, 219.

(23) Kung, H. H.; Jarrett, H. S.; Sleight, A. W.; Ferretti, A. *J. Appl. Phys.* **1977**, *48*, 2463.

(24) Moser, J. E.; Wolf, M.; Lenzmann, F.; Grätzel, M. *Zeitschrift für Physikalische Chemie* **1999**, *212*, 85.

(25) Guo, P.; Aegerter, M. A. *Thin Solid Films* **1999**, *351*, 290.

(26) Kim, Y. I.; Atherton, S. J.; Brigham, E. S.; Mallouk, T. E. *J. Phys. Chem.* **1993**, *97*, 11802.

(27) P. Clechet, J. M., R. Oliver, and C. Vallouy *C.R. Acad. Sci. C* **1976**, *282*, 887.

(28) Barros Filho, D.; Abreu Filho, P.; Werner, U.; Aegerter, M. *J. Sol-Gel Sci. Technol.* **1997**, *8*, 735.

(29) Chen, S. G.; Chappel, S.; Diamant, Y.; Zaban, A. *Chem. Mat.* **2001**, *13*, 4629.

(30) Aegerter, M. A.; Schmitt, M.; Guo, Y. *Int. J. Photoenergy.* **2002**, *4*, 1.

(31) EGUCHI, K.; KOGA, H.; SEKIZAWA, K.; SASAKI, K. *JCS-Japan* **2000**, *108*, 1067.

(32) Wei, M.; Qi, Z.-m.; Ichihara, M.; Zhou, H. *Acta Materialia* **2008**, *56*, 2488.

(33) Le Viet, A.; Jose, R.; Reddy, M. V.; Chowdari, B. V. R.; Ramakrishna, S. *J. Phys. Chem. C* **2010**, *114*, 21795.

(34) Ghosh, R.; Brennaman, M. K.; Uher, T.; Ok, M.-R.; Samulski, E. T.; McNeil, L. E.; Meyer, T. J.; Lopez, R. *ACS Appl. Mater. Interfaces* **2011**.

(35) Xia, J.; Masaki, N.; Jiang, K.; Yanagida, S. *J. Phys. Chem. C* **2007**, *111*, 8092.

(36) Zaban, A.; Chen, S. G.; Chappel, S.; Gregg, B. A. *Chem. Commun.* **2000**, 2231.

(37) Kwang-Soon, A.; Moon-Sung, K.; Jae-Kwan, L.; Byong-Cheol, S.; Ji-Won, L. *Appl. Phys. Lett.* **2006**, *89*, 013103.

(38) Chen, X.; Yu, T.; Fan, X.; Zhang, H.; Li, Z.; Ye, J.; Zou, Z. *Appl. Surf. Sci.* **2007**, *253*, 8500.

(39) Michael R. Norris, J. J. C., Christopher R. K. Glasson, Zhen Fang, Dennis L. Ashford, Jonah W. Jurss, Joseph L. Templeton, Thomas J. Meyer *In preparation* **2012**.

(40) Lee, S.-H. A.; Abrams, N. M.; Hoertz, P. G.; Barber, G. D.; Halaoui, L. I.; Mallouk, T. E. *J. Phys. Chem. B* **2008**, *112*, 14415.

(41) Ai, X.; Guo, J.; Anderson, N. A.; Lian, T. *J. Phys. Chem. B* **2004**, *108*, 12795.

(42) Lenzmann, F.; Shklover, V.; Brooks, K.; Grätzel, M. *J. Sol-Gel Sci. Technol.* **2000**, *19*, 175.

(43) Gallagher, L. A.; Serron, S. A.; Wen, X.; Hornstein, B. J.; Dattelbaum, D. M.; Schoonover, J. R.; Meyer, T. J. *Inorg. Chem.* **2005**, *44*, 2089.

(44) Song, W.; Glasson, C. R. K.; Luo, H.; Hanson, K.; Brennaman, M. K.; Concepcion, J. J.; Meyer, T. J. *J. Phys. Chem. Lett.* **2011**, 1808.

(45) Redmond, G.; Fitzmaurice, D. *J. Phys. Chem.* **1993**, *97*, 1426.

(46) Wang, H.; He, J.; Boschloo, G.; Lindström, H.; Hagfeldt, A.; Lindquist, S.-E. *J. Phys. Chem. B* **2001**, *105*, 2529.

(47) Hanson, K.; Brennaman, M. K.; Luo, H.; Glasson, C. R.; Concepcion, J. J.; Song, W.; Meyer, T. J. *ACS Appl. Mater. Interfaces* **2012**, *4*, 1462.

(48) Patterson, A. L. *Phys. Rev.* **1939**, *56*, 978.

(49) George, P.; Pol, V.; Gedanken, A. *Nanoscale Res. Lett.* **2006**, *2*, 17

(50) Chen, Z.; Zhao, G.; Li, H.; Han, G.; Song, B. *J. Am. Ceram. Soc.* **2009**, *92*, 1024.

(51) Butler, M. A. *J. Appl. Phys.* **1977**, *48*, 1914.

(52) Boschloo, G.; Fitzmaurice, D. *J. Phys. Chem. B* **1999**, *103*, 7860.

(53) Luo, H.; Song, W.; Hoertz, P. G.; Hanson, K.; Ghosh, R.; Rangan, S.; Brennaman, M. K.; Concepcion, J. J.; Binstead, R. A.; Bartynski, R. A.; Lopez, R.; Meyer, T. J. *Chem. Mat.* **2012**, *25*, 122.

(54) Boschloo, G.; Fitzmaurice, D. *J. Phys. Chem. B* **1999**, *103*, 2228.

(55) Berger, T.; Lana-Villarreal, T.; Monllor-Satoca, D.; Gómez, R. *J. Phys. Chem. C* **2007**, *111*, 9936.

(56) Morris, A. J.; Meyer, G. J. *J. Phys. Chem. C* **2008**, *112*, 18224.

(57) Cao, F.; Oskam, G.; Searson, P. C.; Stipkala, J. M.; Heimer, T. A.; Farzad, F.; Meyer, G. J. *J. Phys. Chem.* **1995**, *99*, 11974.

(58) Kavan, L.; Kratochvilová, K.; Grätzel, M. *J. Electroanal. Chem.* **1995**, *394*, 93.

(59) Fabregat-Santiago, F.; Mora-Seró, I.; Garcia-Belmonte, G.; Bisquert, J. *J. Phys. Chem. B* **2002**, *107*, 758.

(60) Kang, S. H.; Kim, J.-Y.; Sung, Y.-E. *Electrochim. Acta* **2007**, *52*, 5242.

(61) Ondersma, J. W.; Hamann, T. W. *J. Am. Chem. Soc.* **2011**, *133*, 8264.

(62) Butler, M. A.; Ginley, D. S. *J. Electrochem. Soc.* **1978**, *125*, 228.

(63) Hanson, K.; Brennaman, M. K.; Ito, A.; Luo, H.; Song, W.; Parker, K. A.; Ghosh, R.; Norris, M. R.; Glasson, C. R. K.; Concepcion, J. J.; Lopez, R.; Meyer, T. J. *J. Phys. Chem. C* **2012**, *116*, 14837.

(64) Brennaman, M. K.; Patrocinio, A. O. T.; Song, W.; Jurss, J. W.; Concepcion, J. J.; Hoertz, P. G.; Traub, M. C.; Murakami Iha, N. Y.; Meyer, T. J. *ChemSusChem* **2011**, *4*, 216.

(65) Bergeron, B. V.; Kelly, C. A.; Meyer, G. J. *Langmuir* **2003**, *19*, 8389.

(66) Ueno, S.; Fujihara, S. *Electrochim. Acta* **2011**, *56*, 2906.

(67) Feng, X.; Shankar, K.; Varghese, O. K.; Paulose, M.; Latempa, T. J.; Grimes, C. A. *Nano Lett.* **2008**, *8*, 3781.

(68) O'Regan, B. C.; Durrant, J. R. *Acc. Chem. Res.* **2009**, *42*, 1799.

(69) Hiyoshi, M.; Lee, B.; Lu, D.; Hara, M.; Kondo, J. N.; Domen, K. *Catal. Lett.* **2004**, *98*, 181.

(70) Nakajima, K.; Baba, Y.; Noma, R.; Kitano, M.; N. Kondo, J.; Hayashi, S.; Hara, M. *J. Am. Chem. Soc.* **2011**, *133*, 4224.

Chapter 3: Nanocrystalline $SrTiO_3$ films Sensitized by a Znic Porphyrin in Dye Sensitized Solar Cells

3.1 Introduction

As a ternary metal oxide, $SrTiO_3$ with perovskite type cubic structure shares a similar structure to anatase TiO_2,[1] where titanium atoms are in 6-fold octahedral coordination in $SrTiO_3$. $SrTiO_3$ was reported to have a more negative flat band potential than anatase TiO_2 [2] and therefore a $SrTiO_3$-based DSSC is expected to have a higher Voc than anatase-based one.[3] However, there have been a limited number of literatures that explore the application of $SrTiO_3$ photoanodes in comparison with TiO_2. Burnside et al. carried out flash laser photolysis and absorbance studies, proposing that the low photocurrents observed for N3 sensitized $SrTiO_3$ nanofilms could be attributed to poor dye loading on the oxide surface, but not to electron injection or transport problems in the semiconductor. [3] Yang et al. found out flat band potential and trap states of $SrTiO_3$ nanocrystalline film greatly dependent on the pH of aqueous electrolyte solution.[4] that Later, Yang group tested flat band edges of $SrTiO_3$ nanoparticle film in propionitrile (PN), acetylacetone (Acac), and PN/Acac in order to study the solvent chelation effects on the band energies.[5] They found out a very negative flat band edge at the present of exclusive tetrabutylammonium ions. Addition of lithium cations will shift flat band positively and reduce trap states densities as well. They also tuned band energies of N3-derivatized $SrTiO_3$ film by optimizing electrolyte composition. The best $SrTiO_3$ DSSC cell in their paper was using

Acac, giving high open-circuit voltage of 0.6 V and short circuit current of 0.41 $mA \cdot cm^{-2}$ under 100$mW.cm^{-2}$ Xe lamp, which could be explained by the smallest trap state density and thus less recombination.

Porphyrin dyes have been widely utilized in DSSCs as chromophores, generally displaying strong visible light absorption due to π-π* transition of the macrocycle from ground state to the first singlet excited state or the second singlet excited state.[1] Compared with traditional Ruthenium polypyridyl compounds, porphyrin dyes are easier to obtain high redox potential (up to -1.3 V vs. NHE) of excited states by changing substituting groups.[2,3] Therefore, porphyrin dye could serve as a modeling chromophore better for $SrTiO_3$ photoanodes that have higher conduction band edge.

In this work, systematic comparison of $SrTiO_3$ to TiO_2 as photoanodes in DSSCs was conducted by using a znic porphyrin dye, ZnPC. Two types of $SrTiO_3$ photoanodes and anatase TiO_2 films were carefully examined after ZnPC sensitization, which was proved to have energy levels and band positions right aligned favorable for efficient electron injection from ZnPC into metal oxides. Nanosecond transient absorption further revealed the interfacial dynamics for ZnPC on $SrTiO_3$ and TiO_2, in which electron injection might be primarily from singlet ZnPC excited state to $SrTiO_3$ while from both singlet and triplet ZnPC excited states to TiO_2 conduction band. In addition, $SrTiO_3$ displayed slower back electron transfer than TiO_2 in the sense of better charge separation. However, ZnPC sensitized DSSCs on TiO_2 showed IPCE and energy conversion efficiency tremendously higher than on $SrTiO_3$, which could be ascribed to suppression of photocurrent from large interfacial charge transfer resistance between conduction band of $SrTiO_3$ and electrolyte (I^{3-}, etc.). Therefore, it may be proposed that the key for $SrTiO_3$ as an efficient photoanodes lies in improving electron transport property by appropriate

fabrication techniques such as toward thinner $SrTiO_3$ films without deterioration of surface area, or toward rod-like structure that is known to have better electron transport.

3.2 Experimental Section

3.2.1 Materials

All materials were used as received without further purification. $LiClO_4$ (99.999 %, trace metal basis), hydroxypropyl cellulose (HPC, average M_W = 80,000, 20 mesh particle size), 4-iodobenzoic acid, tetra-(triphenylphosphine) palladium(0), and CuI were obtained from Sigma-Aldrich. Acetonitrile (MeCN; Optima™ LC/MS), dichloromethane, Ethanol (200 Proof) and methanol were purchased from Fisher Scientific. ***s*-SrTiO$_3$** nanoparticles were purchased from Nanograde *Ltd*. and ***b*-SrTiO$_3$** nanoparticles were purchased from MTI Corporation. Fluorine-doped SnO_2 (FTO) glass substrates of 15 Ω/□ were obtained from Hartford Glass, Inc. 25 μm Surlyn films were purchased from Solaronix and electrolyte for DSSC cells (EL-HPE) were obtained from Dyesol.

3.2.2 Synthesis

Compound ZnPC

Compound **ZnPC** was prepared in high yield from the mono-ethynyl zinc porphyrin and 4-iodobenzoic acid via palladium catalyzed cross coupling reaction (Scheme 3-1.). Synthesis of the monoethynyl zinc porphyrin is reported elsewhere.[4]

Zinc(II) 5,15-bis-ethynyl-10,20-bis[2',6'-bis(3,3-dimethyl-1-butyloxy)phenyl]porphyrinate (156 mg, 0.164 mmol) and 4-iodobenzoic acid (49 mg, 0.197 mmol) were placed into a 100 mL Schlenk flask with a stir bar. Tetra-(triphenylphosphine) palladium(0) (19 mg, 16.4 μmol) and CuI (5 mg, 16.4 μmol) were added. A solvent mixture

Scheme 3-1. Synthetic pathway of ZnPC.

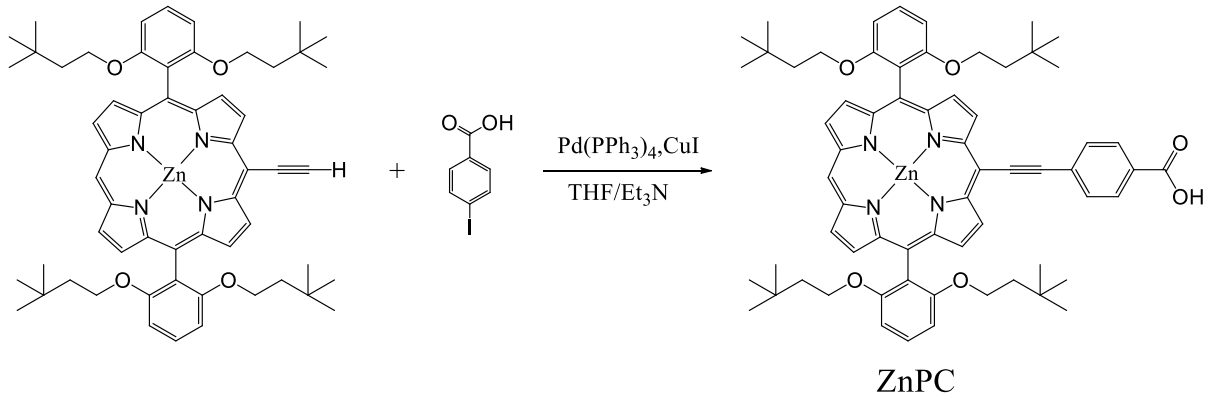

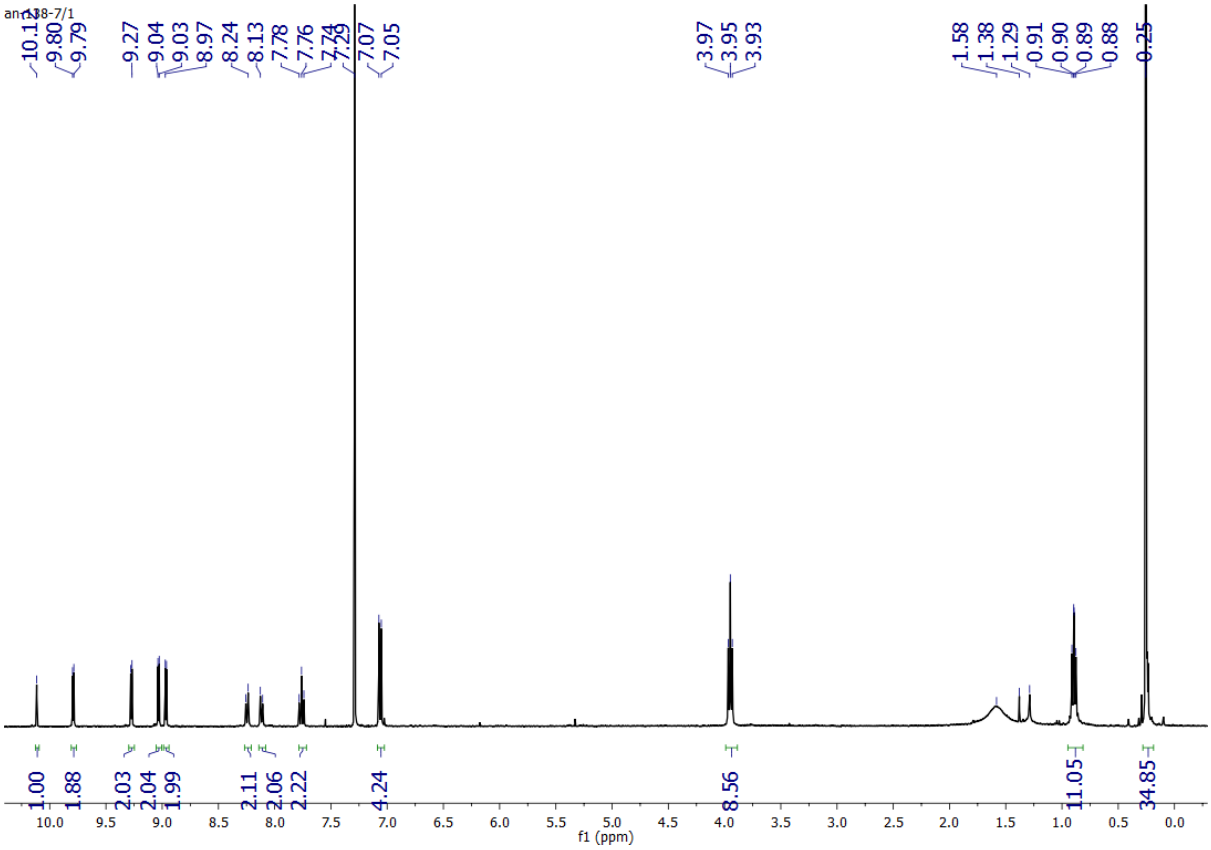

Figure 3-1. 1H NMR spectrum (400 MHz) for **ZnPC** in Deuterated chloroform.

of dry THF (22 mL), and Et_3N (3 mL) was completely degassed by passing N_2 through the solvent and added to the Schlenk tube. Then the reaction mixture was stirred under N_2 atmosphere at 55 °C for 16 h. The reaction mixture was cooled to r.t. and the solvent evaporated.

The residue was purified by column chromatography on silica gel eluted with a mixed solvent of CH_2Cl_2/MeOH = 95:5. The major green band was collected and solvent evaporated (151 mg, 0.141 mmol, 86 % yield based on starting mono-ethynyl porphyrin). ^{1}H NMR ($CDCl_3$): δ 10.12 (s, 1H), 9.79 (d, J = 4.5 Hz, 2H)), 9.27 (d, J = 4.4 Hz, 2H)), 9.03 (d, J = 4.4 Hz, 2H)), 8.97 (d, J = 4.4 Hz, 2H)), 8.24 (d, J = 8.0 Hz, 2H)), 8.11 (d, J = 8.0 Hz, 2H)), 7.76 (t, J = 8.4 Hz, 2H)), 7.06 (d, J = 8.4 Hz, 4H)), 3.95 (t, J = 7.2 Hz, 8H) , 0.89 (t, J = 7.2 Hz, 8H), 0.25 (s, 36H) (see Figure 3-1).

nanoSrTiO$_3$ Preparation

$SrTiO_3$ nanopowder (0.946 *g* for ***s*-SrTiO$_3$** paste and 1.5g for ***b*-SrTiO$_3$** paste) was transferred to a scintillation vial containing 10 mL anhydrous ethanol. The mixture was bath sonicated for 30 minutes, shaken, and then ultrasonicated using a microtip on a 50 % duty cycle for 6 minutes. The resulting suspension was allowed to cool down to room temperature, followed by slowly adding HPC polymer that was haft the weight of $SrTiO_3$ nanopowder. The paste was kept stirring overnight before use. *nano*$SrTiO_3$ films were deposited onto conducting FTO glass substrates by doctor blading which was then followed by firing at 550 ^oC for 1 hour in a box oven.

Anatase TiO_2 (15–20 nm nanoparticles) or ZrO_2 (10–15 nm nanoparticles) slides were prepared according to reported literature procedure. [5,6] Scotch tape was tailored as mask to obtain desired area covered by metal oxide. All metal oxide film thickness was controlled by the numbered layers of scotch tape and monitored by cross-section imaging from scanning electron microscopy (Hitachi S-4700 Cold Cathode FESEM). Metal oxide films were first exposed to 0.2 mM **ZnPC**/toluene solution for 12 h, then to MeCN overnight to remove non-derivatized porphyrin molecules. Surface coverage (Γ in mol/cm^2) was calculated from $\Gamma = A_{(\lambda)}/\varepsilon_{(\lambda)}/1000$,[7]

where $\varepsilon_{(\lambda)}$ was the molar extinction coefficient for **ZnPC** in MeCN/toluene (24:1 v/v) solution determined by inductively coupled plasma mass spectrometry(ICP-MS, Varian 820), and $A_{(\lambda)}$ was the Soret and Q-band absorbances of derivatized films.

3.2.3 DSSC Cell Fabrication

DSSC sandwich cell was fabricated by metal oxide electrode, Surlyn films, and Pt-coated FTO slide with a pre-drilled hole. Electrolyte containing I_2/I_3^- redox couple was injected by vacuum backfilling and the hole was covered by Surlyn film and a cover glass.[8]

3.2.4 Measurements

^{1}H-NMR spectra were recorded on a Bruker NMR 400 DRX Spectrometer at 400 MHz using Deuterated chloroform as solvent. XRD measurement were performed on a Rigaku Multiflex diffractometer in theta-two theta mode using Cu K_α radiation ($\lambda = 1.5418$ Å). Morphology analysis was conducted by a Hitachi 4700 Field Emission scanning electron microscopy (FESEM), a JEM 100CX-II transmission electron microscope (TEM) and a JEOL 2010F FasTEM for HRTEM images. Nitrogen adsorption measurement was obtained on a Quantachrome Autosorb-1C. A customized three-arm photoelectrochemical cell was employed in the electrochemical and spectroelectrochemical measurements. The arm for the photoanode was a 10 mm pathlength Pyrex cuvette. A platinum wire was used as the cathode and $Ag/AgNO_3$ as the reference electrode. The photoanode was inserted at a 45° angle into a homemade Teflon seat located in the cuvette part of the cell. All experiments were carried out under Argon at (22 ± 2) ^oC unless otherwise specified. A CH Instruments model 601D potentiostat was employed for electrochemical characterization. UV-visible measurements were conducted on an Agilent Cary 50 UV-Vis spectrophotometer. Steady-state emission spectra were collected using an Edinburgh FLS920 spectrometer with a 450 W Xe lamp excitation source and R2658P photomultiplier tube

as the detector. Mott−Schottky spectra were conducted with a three-electrode cell at 30 Hz in the dark, using the sintered $SrTiO_3$ photoanodes as the working electrode, a platinum wire as the counter electrode, and a standard $Ag/AgNO_3$ as the reference electrode. The electrolyte was 0.1 M $LiClO_4$ in MeCN. Linear sweep voltammetry and electrochemical impedance spectroscopy (EIS) were employed to characterize device performance by using a Gamry 500 potentiostat with Gamry Framework. An AM1.5 (1 sun) solar simulator (Newport 1000W Xe lamp and an AM1.5 filter) was used as the light source for device irradiation.

3.2.5 Incident photon-to-current conversion efficiencies (IPCE)

IPCE were measured using a homebuilt instrument. White Light from a 75W Xenon lamp in an Oriel photomax housing was passed through an Oriel Cornerstone 260 monochromator. The single color output was then focused onto the device. A metal Faraday cage, which had been painted black, enshrouded devices during the whole measurement and minimized stray light and induced current. Incident photon flux was measured by a UDT S370 optometer coupled with a UDT 260 detector. Light intensity was checked for fluctuation by performing light intensity measurements before and after photocurrent measurements. Fluctuations were found to be ± 5 % or else the data were not used. Current measurements were conducted with a Keithley 2400 sourcemeter. Electrical connection to the device was made using coaxial cable attached directly to the FTO glass via alligators clips. Experiment control including synchronization of data collection with monochromator wavelength movement was achieved via PC control through LabView using homebuilt software.

3.2.6 Transient absorption (TA)

TA measurements were carried out by inserting derivatized films at a 45° angle into a standard 10 mm path length square Pyrex cuvette containing electrolyte. The top of the cuvette

was fit with an O-ring seal with a Kontes valve inlet to allow the contents to be purged with Argon. The experiments were performed by using nanosecond laser pulses produced by a Spectra-Physics Quanta-Ray Lab-170 Nd:YAG laser combined with a VersaScan OPO (5-7 ns, operated at 1 Hz, beam diameter 1 cm) integrated into a commercially available Edinburgh LP 920 laser flash photolysis spectrometer system. A white light probe pulse was generated by a pulsed 450 W Xe lamp. The probe light was passed through a 400 nm long pass filter before reaching the sample to avoid direct band gap excitation of metal oxide films, then detected by a photomultiplier tube (Hamamatsu R928), or by a gated CCD (Princeton Instruments, PI-MAX3, gate width 10 ns, bandwidth 2.05 nm). Appropriate color filters were placed before the detector to reject unwanted scattered light. Single wavelength kinetic data were averaged over 50-100 laser shots.

3.3 Results and Discussion

3.3.1 Morphology of $SrTiO_3$

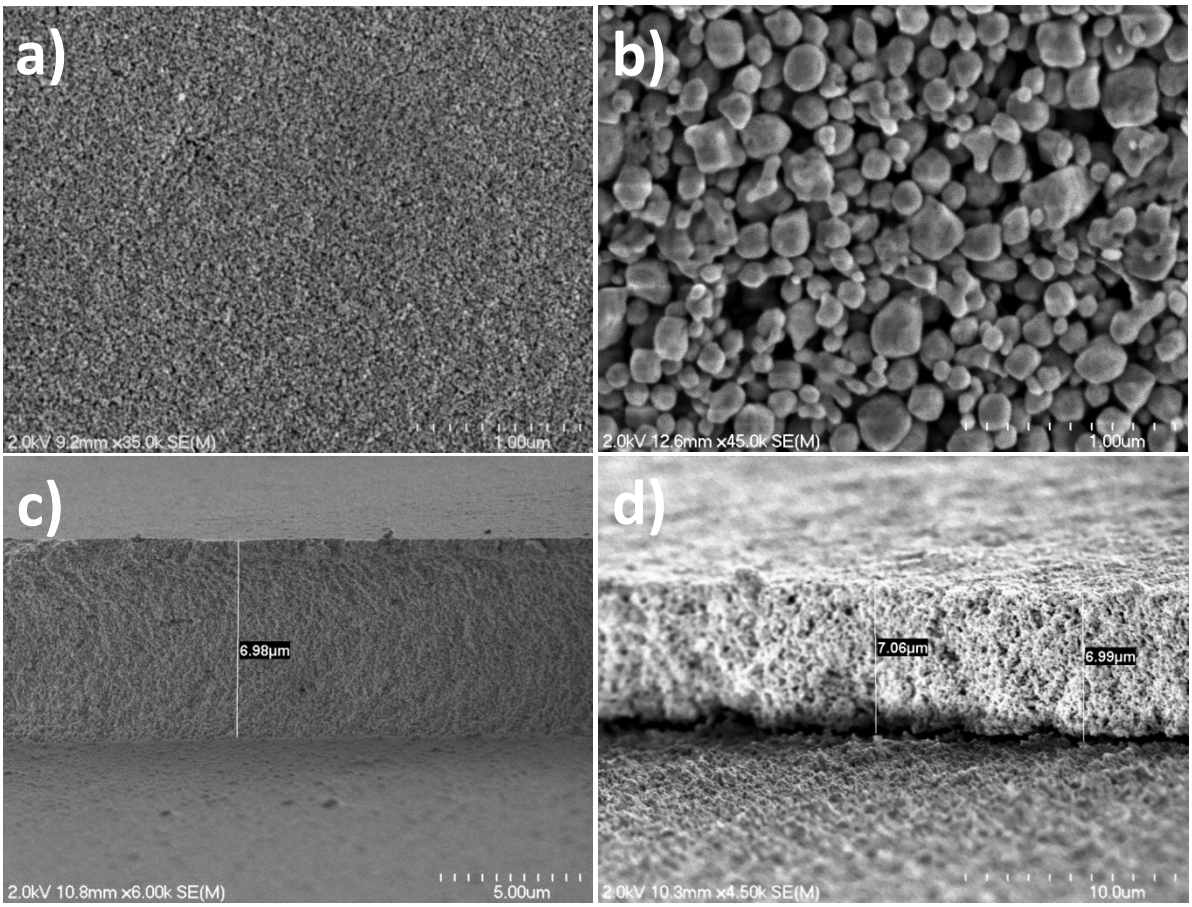

Figure 3-2. FE-SEM images for *s*-$SrTiO_3$ film (a): surface and (c) cross section and *b*-$SrTiO_3$ film (b): surface and (d) cross section films calcinated at 550 ^{o}C for 1 hour.

Two types of $SrTiO_3$ films making from small (s-$SrTiO_3$) and big nanoparticles (b-$SrTiO_3$) were synthesized, as shown in Figure 3-2. The thickness of films could be prepared up to 7 µm according to cross section imaging. The X-ray diffraction diagrams for calcinated

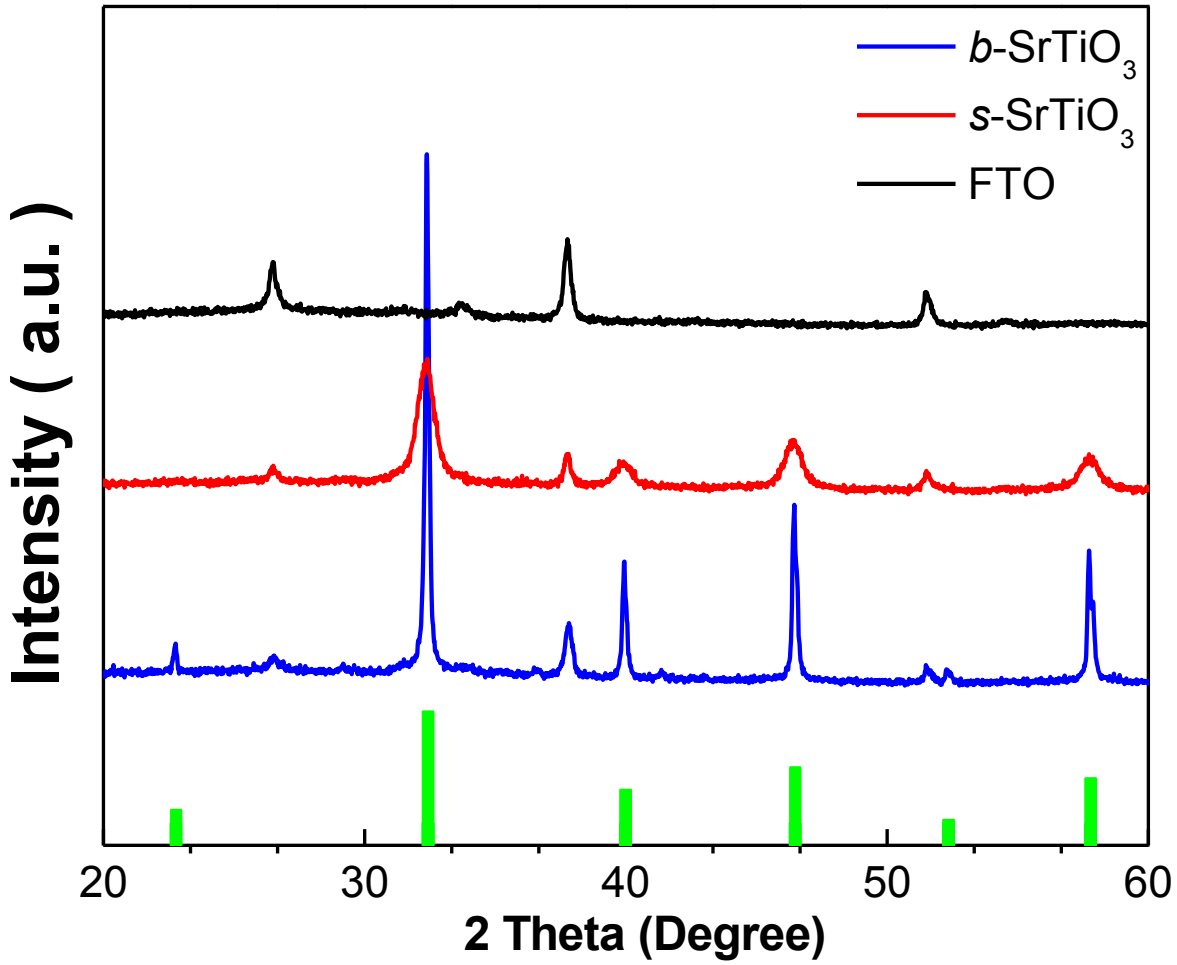

Figure 3-3. X-ray diffraction diagrams (XRD) of *s*-$SrTiO_3$ and *b*-$SrTiO_3$ films. The bars below XRD patterns indicate the position and diffraction lines of cubic $SrTiO_3$ ($Pm\bar{3}m$, JCPDS File No. 35-0734). All films were calcinated at 550 ^{o}C for 60 min.

s-$SrTiO_3$ and *b*-$SrTiO_3$ films at 550 ^{o}C indicated that they belong to cubic $SrTiO_3$ ($Pm\bar{3}m$, JCPDS File No. 35-0734) (Figure 3-3). The HRTEM images of *s*-$SrTiO_3$ and *b*-$SrTiO_3$ particles in Figure 3-4 exhibited clear lattice fringes, consistent with highly crystalline samples after annealing. The close interplanar spacing for both $SrTiO_3$ nanoparticles, ~ 2.7 and 2.8 Å, corresponded to the literature value of (110) facets in cubic $SrTiO_3$ exposed on the crystal surfaces.[9] The sizes determined from HRTEM for *s*-$SrTiO_3$ and *b*-$SrTiO_3$ are ~ 11 and 130 nm

respectively, which are in good agreement with the average sizes calculated by the Scherrer Equation from XRD patterns, ~ 12 and 112 nm.[10]

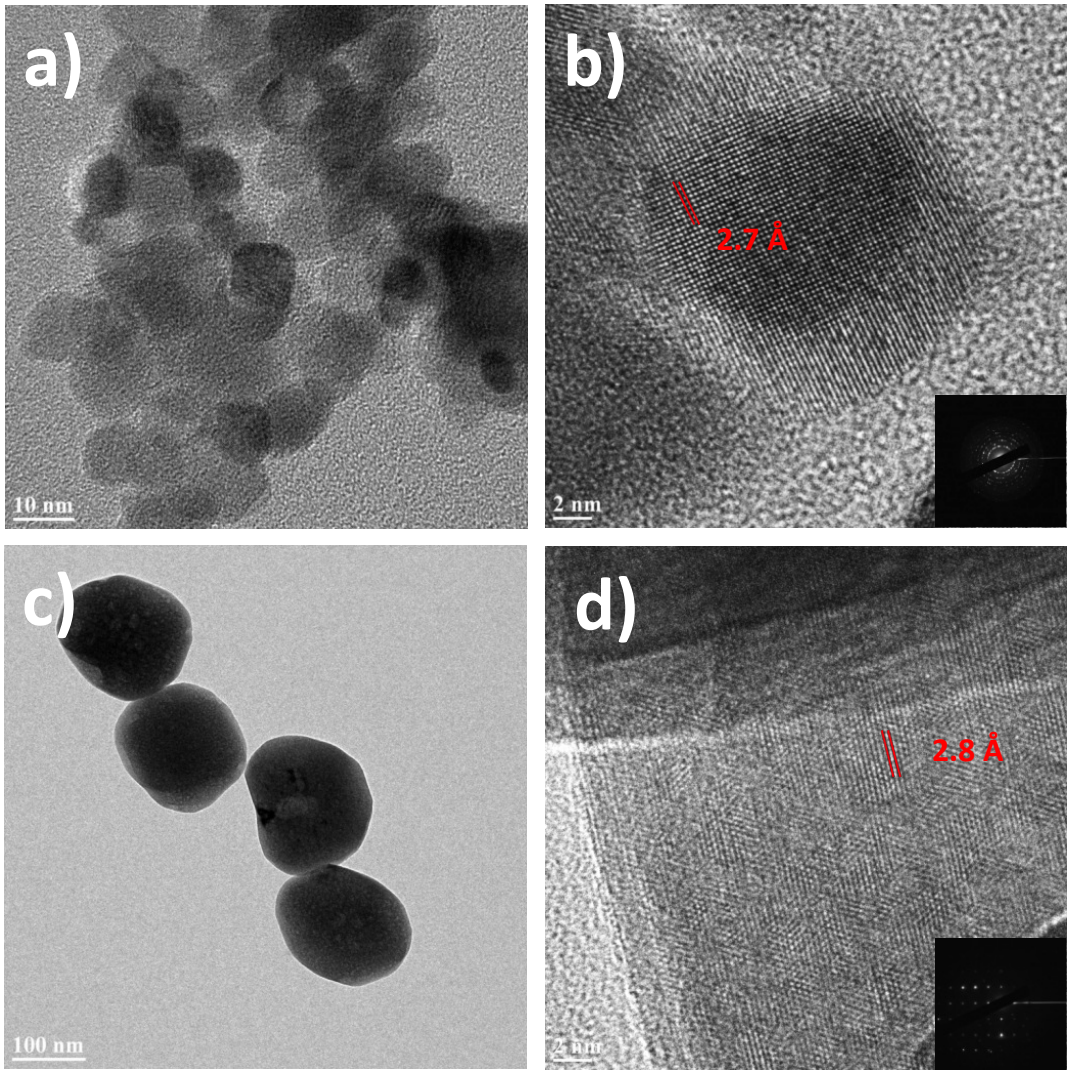

Figure 3-4. HRTEM images for *s*-$SrTiO_3$ (a) and (b) and *b*-$SrTiO_3$ (c) and (d).The lattice fridges in (b) and (d) have an interplanar spacing of ~ 2.7 and 2.8 Å that belongs to (110) planes of cubic $SrTiO_3$ ($Pm\bar{3}m$, JCPDS File No. 35-0734).

Metal oxides nanocrystalline films were measured by N_2 adsorption (Figure 3-5), indicative of type IV isotherm for all metal oxides. TiO_2 and s-$SrTiO_3$ films displayed hysteresis loops of type H1, while *b*-SrTiO3 displayed hysteresis loops of type H3, implying different pore

structures in materials of H3 and H1 loops. The surface area, total pore volume, and porosity were calculated here: for TiO_2, 116 m^2g^{-1}, 0.39 cm^3 g^{-1} and 67 % (density: 3.898 g/cm^3); for *s*-$SrTiO_3$, 83 m^2g^{-1}, 0.29 cm^3 g^{-1}, and 60 % (density: 5.116 g/cm^3); for b-$SrTiO_3$, 49 m^2g^{-1}, 0.3 cm^3 g^{-1}, and 60 % (density: 5.116 g/cm^3). The significant lower surface area for b-$SrTiO_3$ than s-$SrTiO_3$ originated from the bigger $SrTiO_3$ nanoparticles used in b-$SrTiO_3$ films.

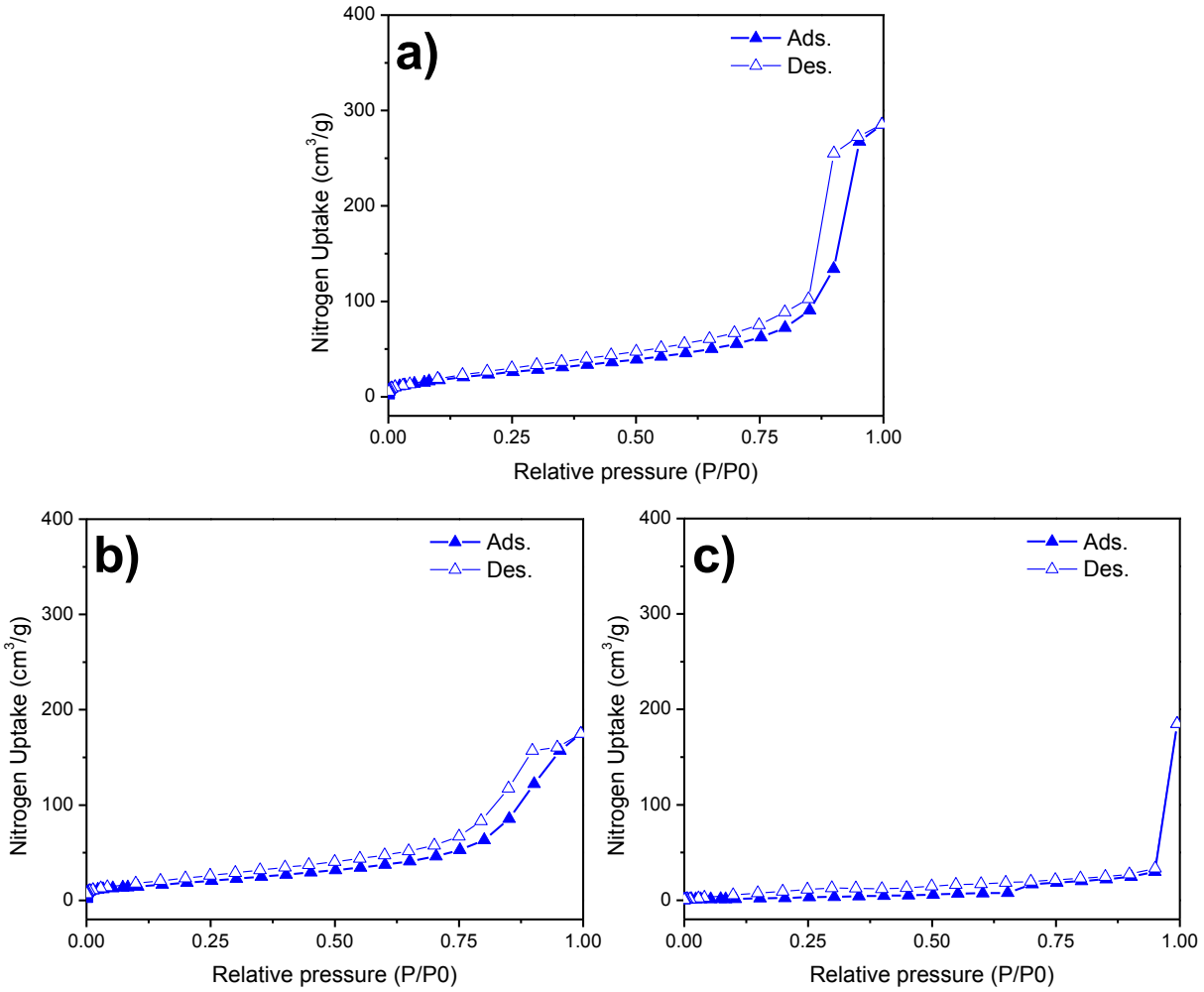

Figure 3-5. N_2 adsorption-desorption isotherms for (a) TiO_2, (b) *s*-$SrTiO_3$, and (c) *b*-$SrTiO_3$ nanostructured films after calcination.

3.3.2 Flat band of $SrTiO_3$ and TiO_2 photoanodes

The Mott-Schottky (MT) plots analysis described a linear relationship between the applied potential and the inverse square of capacitance ($1/C_{sc}^2$) when the doping semiconductor space charge layer region is in depletion.[11] The relationship should be calculated by equation 3-1:

$$\frac{1}{C_{sc}^{\ 2}} = \frac{2}{e\varepsilon\varepsilon_0 N_d A^2}(-\Delta\Phi - \frac{k_b T}{e}) \tag{3-1}$$

Here e is electronic charge (1.6×10^{-19} C), ε_0 is the permittivity of free space (8.86 $\times10^{-12}$ F/m), ε is the dielectric constant of the photoanodes, N_d is dopant (donor or acceptor) concentration, $-\Delta\phi$ is the difference between the applied potential (V) and the flat-band potential ($V - V_{fb}$), k_b is the Boltzmann constant, and T is the absolute temperature, and k_bT/e = 0.026 V at 298 K. E_{fb} refers to the potential when there is no charge accumulation in the semiconductor so that the energy bands show no bending.[11-14] The dopant density N_d can be determined from the slope of the linear region from the MT plot, following equation 3-2:

$$N_d = -\frac{2}{e\varepsilon\varepsilon_0 A^2}(\frac{d(1/C^2)}{dV})^{-1} \tag{3-2}$$

The apparent flat-band potential V_{fb0}, $V_{fb0} = -(V_{fb} + V_1)$ obtained from MT curve was shifted negatively from the real flat band potential V_{fb} by an amount V_1 in the MT analysis of nanoporous TiO_2 electrodes, where $V_1 = N_d e\varepsilon\varepsilon_0/2C_H^2$ and C_H is the Helmoholtz capacitance of the electrode that is in series with C_{sc}.[13] Thus, the capacitance could be described in nanoporous photoelectrode in equation 3-3.

$$\frac{1}{C^{\ 2}} = \frac{2}{e\varepsilon\varepsilon_0 N_d A^2}(-\Delta\Phi - \frac{k_b T}{e}) + \frac{1}{C_H^{\ 2}} \tag{3-3}$$

According to MT analysis results in Figure 3-6, the apparent flat band potential for *s*-$SrTiO_3$, *b*-$SrTiO_3$, and TiO_2 were calculated to be -0.75 V, -0.65 V, and -0.20 V vs. NHE in 0.1 M $LiClO_4$ in MeCN. According to equation 3-2, with e = 1.6×10^{-19} C, $\varepsilon_0 = 8.86 \times 10^{-12}$ F/m, and ε = 45.1 F/m for anatase TiO_2 and 301 F/m for cubic $SrTiO_3$,[15] the electron concentration could be obtained to be 1.2×10^{20}, 2.15×10^{19} and 1.10×10^{20} cm^{-3} for *s*-$SrTiO_3$, *b*-$SrTiO_3$, and TiO_2, respectively. Thus, as-synthesized $SrTiO_3$ films have higher conduction band (~ 50 eV) than TiO_2 films.

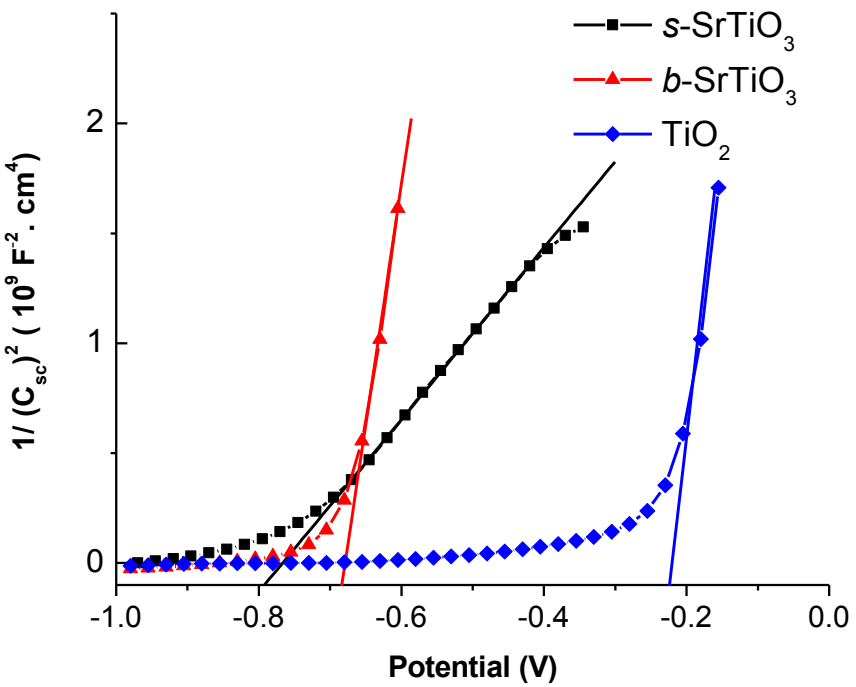

Figure 3-6. Mott-Schottky (MT) plots of the photoanodes, consisting of TiO_2, *b*-$SrTiO_3$, and *s*-$SrTiO_3$ films with 1 cm^2 active area in 0.1 M $LiClO_4$ in acetonitrile (MeCN).

3.3.3 Absorbance, emission spectra for ZnPC on $SrTiO_3$ and TiO_2

In the present study, **ZnPC** was the modeling chromophore to compare TiO_2 and $SrTiO_3$ photoanodes. The UV-vis spectrum of **ZnPC** was characteristic of a porphyrin ring, with an intense Soret band centering at 438 nm and less intense Q bands peaking at 566 and 618 nm

(Figure 3-7a). The Q band decreased from four to two resulting from the introduction of a Zn^{2+}.[16] The emission spectrum exhibited two strong peaks on ZrO_2 at 625 and 683 nm, indicative of primary fluorescence in **ZnPC** (Figure 3-7b).[17] The significant electron quenching for s-$SrTiO_3$ and TiO_2 in emission spectra was evidence for electron injection from excited state, ZnP*, into conduction band of semiconductors, while electron injection was inhibited to ZrO2 due to its high conduction band edge (~ -1.4 V vs NHE, pH = 7).[18] The one-electron oxidation potential ($E_{ZnPC+/0}$) of **ZnPC** was 0.91 V vs. NHE measured by cyclic voltammetry (CV) in MeCN containing 0.1 M $LiClO_4$ as a supporting electrolyte (Figure 3-8a). Based on the absorption, emission, and electrochemical data, the excited state redox potential for **ZnPC**, $E_{ZnPC+/*}$, is approximated to be -1.08 V vs. NHE by extracting the zero excitation energy (E_{0-0}) from the oxidation potentials of the ground state, $E_{ZnPC+/0}$. [19] A summary of band position and energy levels for photoanodes conduction band edges and **ZnPC** are shown in Figure 3-8b, showing that electron injection from ZnPC to three photoanodes is energetically favorable.

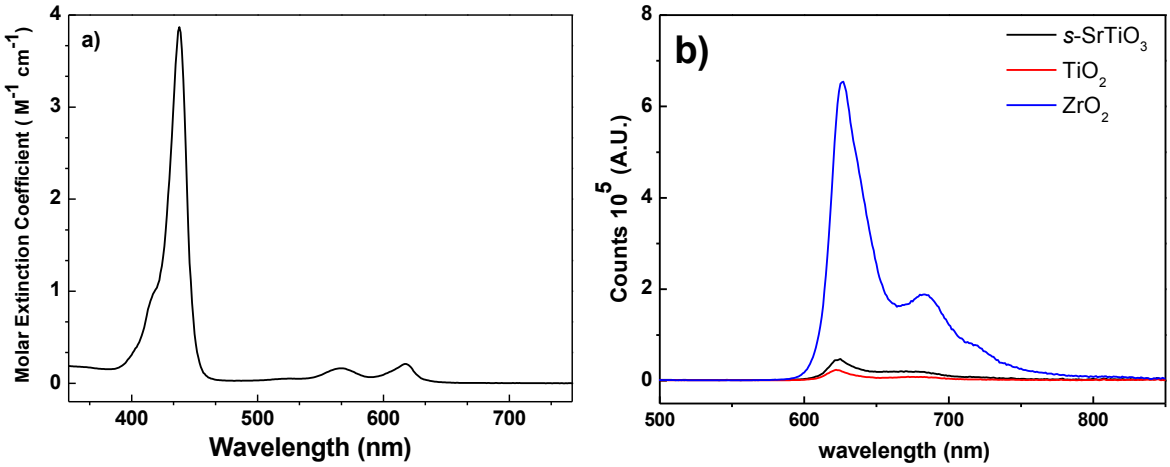

Figure 3-7. (a): UV-vis absorption spectrum of **ZnPC** in MeCN/toluene (24:1 v/v) solution. (b): Emission spectra of **ZnPC** derivatized *s*-$SrTiO_3$, TiO_2 and ZrO_2 in MeCN containing 0.1 M $LiClO_4$ (excitation at 441 nm).

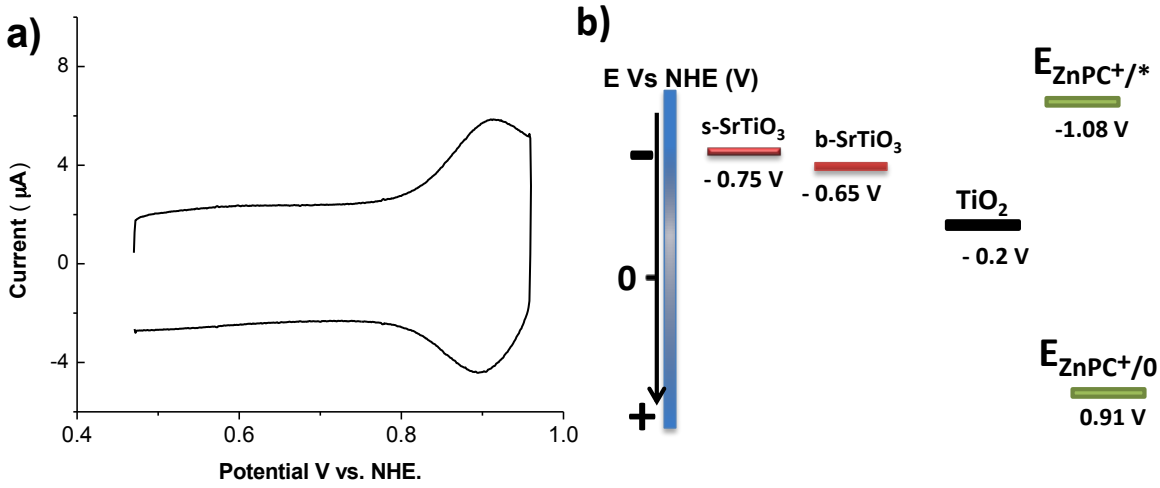

Figure 3-8. (a): cyclic voltammetry (CV) of ZnPC derivatized FTO in MeCN containing 0.1 M $LiClO_4$. (b): band position and energy levels relevant to electron injection of **ZnPC**. For photoanodes, only the positions of conduction band edges are shown here.

3.3.4 Nanosecond transient absorption for ZnPC sensitized $SrTiO_3$ and TiO_2

To further probe the electron transfer process in ZnPC derivatized $SrTiO_3$ and TiO_2 photoanodes, nanosecond laser flash photolysis experiments were conducted. Znic porphyrins are known to adopt inter system crossing and generate triplet states upon photoexcitation.[20] In Figure 3-9. time-resolved transient difference absorption spectra of ZnPC on ZrO_2 with two isosbestic points ~ 614nm and 648 nm were characteristic of absorption changes centered at 510 nm and 780 nm due to triplet-triplet absorption.[21-23] This is consistent with the unquenched electrons on ZrO_2 in previously mentioned emission spectrum Figure 3-7. Porphyrin surface bounded on both $SrTiO_3$ and TiO_2 showed a new absorption peak at ~ 700 nm that could be assigned to porphyrin cation radicals as confirmed by spectroelectrochemical study. This was another evidence for electron injection from ZnPC into conduction band of metal oxides. Electron injection of Znic porphyrins usually finish at sub-ps scale which was beyond nanosecond TA capability.[24,25]

$$A_t = A_0 e^{-(t/\tau)^{\beta}} \tag{3-4}$$

$$k = \tau_{ave}^{-1} = [\tau / \beta\ \Gamma(1/\beta)]^{-1} \tag{3-5}$$

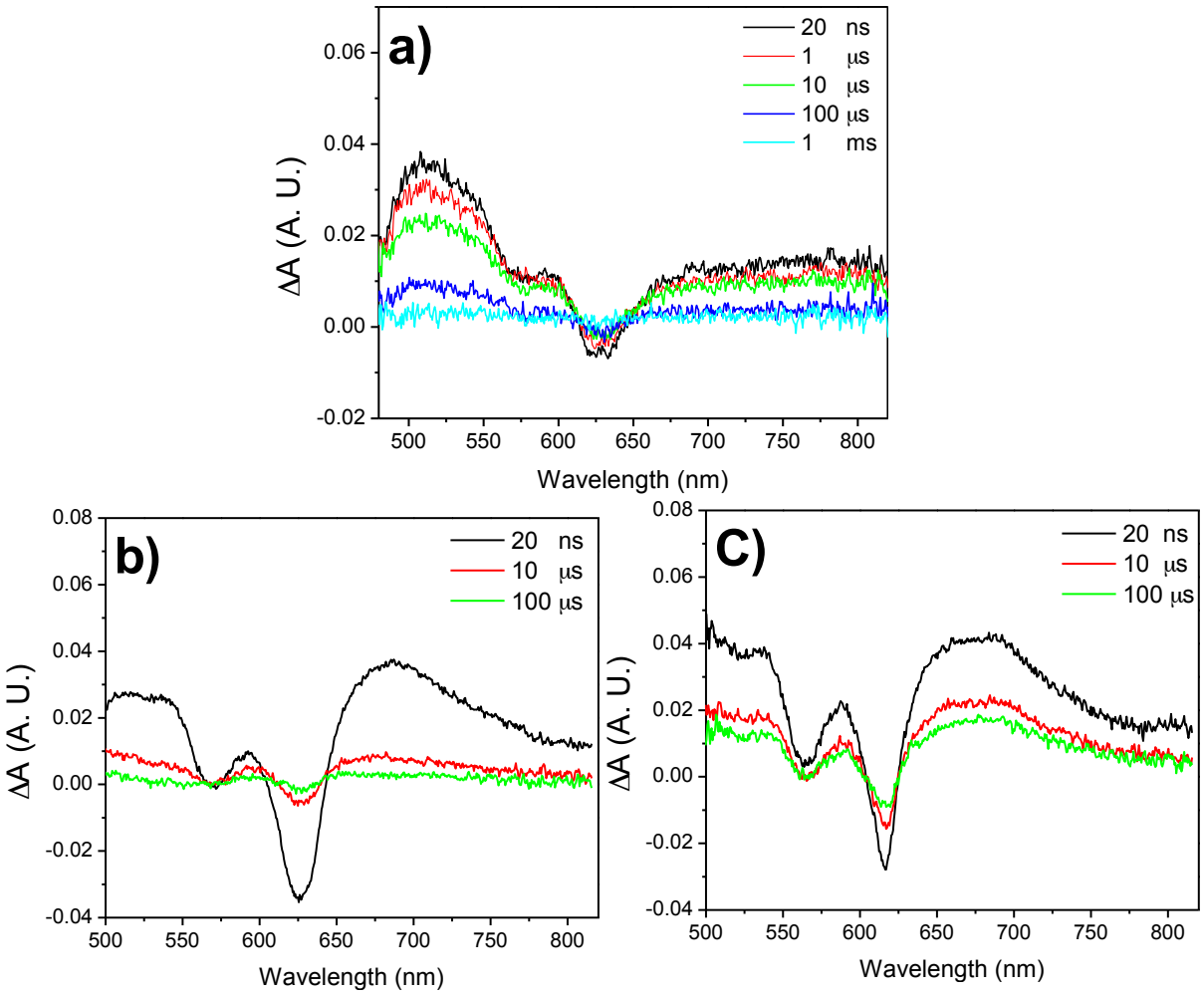

Figure 3-9. Time-resolved transient difference absorption spectra monitored different period of time after laser pulse. Samples were **ZnPC** derivatized (a) ZrO_2, (b) TiO_2 and (c) s-$SrTiO_3$ in deaerated MeCN containing 0.1 M $LiClO_4$ excited with 450 nm nanosecond pulsed laser.

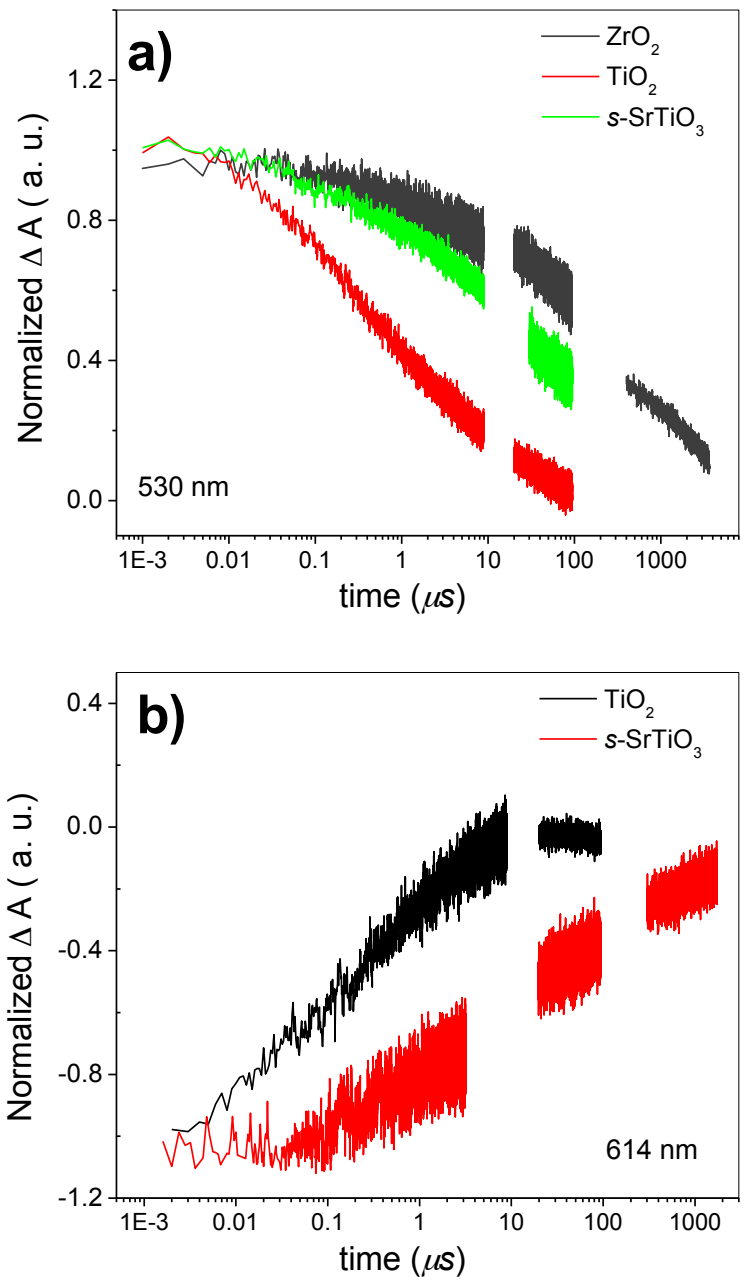

Figure 3-10. Normalized nanosecond absorbance-time traces probed at (a) 530 nm and (b) 614 nm for **ZnPC** derivatized ZrO_2, TiO_2 and s-$SrTiO_3$ in 0.1 M $LiClO_4$ MeCN at room temperature. Data were fit to the stretched exponential function in equation 3-4 and 3-5. Excitation with 450 nm pulsed laser.

To explore the interfacial dynamics between ZnPC and metal oxides photoanodes, absorbance change-time traces were fitted by stretched exponential function in equation 3-4 and 3-5, where τ is a characteristic lifetime, β is inversely related to the width of the underlying Lévy distribution of rate constants with, $0 < \beta < 1$, average life time is τ_{ave} and *k* is the corresponding rate .[26]

Table 3-1. Summary of interfacial dynamics for of ZnPC derivatized ZrO_2, TiO_2 and s-$SrTiO_3$.

	Coverage (mol cm^{-2}) [1]	**Φ_{inj}, injection efficiency**[2]	**nm**	**τ, μs (β)**	**τ_{ave} , μs**
ZrO_2	1.5×10^{-8}	na	530	497.6 (0.32)	3646
TiO_2	2.0×10^{-8}	0.17	530	1.81 (0.32)	13.3
			614	0.42 (0.36)	1.97
s-$SrTiO_3$	1.3×10^{-8}	0.24	530	76.7 (0.31)	650
			614	124.9 (0.29)	1270

[1] Molar absorption coefficient $\varepsilon = 3.9 \times 10^5$ (438 nm), 1.6×10^4 (566 nm) and 2.1×10^4 (618 nm) M^{-1} cm^{-1} in MeCN: toluene (24:1v/v). Slides were partially loaded with ZnPC. [2] TiO_2-$Ru^{II}P^{2+}$ in 0.1 M $HClO_4$ as the actinometer. Injection efficiency was based on absorption change value at 20 ns after laser pulse.

From the data in Figure 3-10a probed at 530 nm, there were long lived triplet excited states (^{3}ZnPC) on ZrO_2, with a life time of 3.636 ms which was in good agreement of other znic

porphyrin triplet life time. [22] Under the same condition, the bleach at 530 nm was speeded up significantly in TiO_2 and moderate in s-$SrTiO_3$ with a life time of 13.3 and 650 μs respectively, which could be ascribed to involvement of ultrafast electron injection. It is ambiguous that whether electrons were from singlet and/or triplet excitation. In similar znic porphyrins, T1 is ~ 0.45 eV lower than S1.[21,27] Accordingly, the redox potential of triplet excited state of ZnPC could be estimated to be ~ -0.63 V. In light of the high conduction band edge of s-$SrTiO_3$ (-0.75 V), it is highly possible that singlet electron injection was dominant process in s-$SrTiO_3$, while singlet and triplet electron injection occur simultaneously in TiO_2, leading to an overall faster decay in bleach at 530 nm.

Back electron transfer (BET) between injected electrons inside semiconductor conduction band and oxidized porphyrin cation radicals was investigated at isosbestic point 614 nm in Figure 3-10b. The rate of BET at s-$SrTiO_3$ (τ_{ave} = 1.27 ms) was noticeably slower than at TiO_2 (τ_{ave} = 1.97 μs).This slow recombination in $SrTiO_3$ than TiO_2 is advantageous for conduction band electrons escape into outer circuit in a photoelectrochemical cell. Apparent injection yields, $\mathbf{\Phi_{inj}}$, were determined from absorbance change-time trace probed at 614 nm, with the assistance of **RuP** on nanoTiO_2 in aqueous 0.1 M $HClO_4$ (Φ_{inj} = 100 %) as the reference.[28] Yields were calculated by using the change in molar absorptivity between ground and excited states, $\Delta\varepsilon_{(614nm)}$= -6800 $M^{-1}cm^{-1}$.[29] Injection yields were calculated to 0.24 and 0.17 for s-$SrTiO_3$ and TiO_2, respectively. Due to the limited time sensitivity of nanosecond TA, this apparent injection yield only describes net outcome of electron injection and BET recombination at 20 ns after laser pulse. The slightly larger injection yield for $SrTiO_3$ over TiO_2 implied the existence of sub-ns BET recombination in TiO_2 mesoporous films. All photophysical parameters were summarized in Table 3-1.

3.3.5 IPCE abd J-V curve for ZnPC derivatized $SrTiO_3$ and TiO_2 DSSCs.

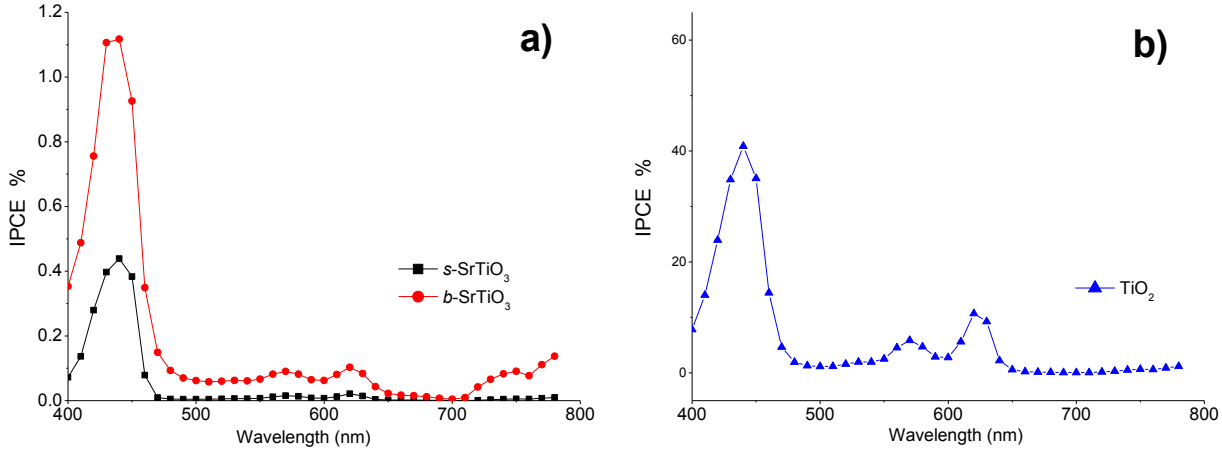

Figure 3-11. Incident photon-to-current conversion action (IPCE %) spectra of TiO_2, *s*-$SrTiO_3$, *b*-$SrTiO_3$ photoanodes sensitized with **ZnPC** in acetonitrile containing I^-/I^{3-} redox mediator using a 75W Xenon lamp.

As shown in Figure 3-11, the incident photon-to-current conversion efficiency (IPCE) in equation 3-6 [30] for **ZnPC** sensitized TiO_2, *s*-$SrTiO_3$, *b*-$SrTiO_3$ photoanodes were determined to be 40.67 %, 1.1 %, and 0.43 % at 440 nm respectively. IPCE reflects the number of electrons induced by light in the outer circuit divided by the number of incident photons,

$$IPCE\% = 100\frac{1240J_{sc}(Acm^{-2})}{\lambda_{nm}P_{in}(\lambda)(Wcm^{-2})} \tag{3-6}$$

where J_{sc} is the short-circuit current generated by incident monochromatic photon flux and λ is the wavelength of this light at an intensity of P_{in}.

The overall solar-to-electrical energy conversion efficiency, η, for a solar cell is defined in equation 3-7, including parameters from J-V curves of DSSCs: short-circuit current (J_{sc}), open circuit voltage (Voc), and fill factor (FF).

$$\eta = \frac{J_{sc}V_{oc}}{P_{in}} FF \tag{3-7a}$$

$$FF = \frac{P_{\max}}{J_{sc}V_{oc}} \tag{3-7b}$$

The photovoltage and photocurrent of DSSCs based on TiO_2, *s*-$SrTiO_3$, and *b*-$SrTiO_3$ employing ZnPC as chromophore were characterized under the simulated AM 1.5 illuminations (100mW/cm2). Only J–V curves of TiO_2 DSSC is displayed in Figure 3-12a, determined to have V_{oc} = 0.57 V, J_{sc} = 7.245 mA/cm^2, FF = 0.60, and η = 2.55 %. There was barely little photocurrent for two $SrTiO_3$ samples which was consistent with small IPCE value at peak position. This low photocurrent was not originated from bad loading as all three photoanodes had high surface area. Nyquist plots of corresponding DSSCs under forward bias were conducted to explore the possible origins in Figure 3-12b and c. An enlarged inset for the high frequency portion in Figure 3-12b is assigned to the resistance of Pt and capacitance C_{pt} of the electrolyte|Pt cathode interface. The diameter of the low frequency semi-cycle (right) represented the charge-transfer resistance (R_{CT}) from conduction band of metal oxides to triiodide ions(I_3^-) in the electrolyte. Under dark condition, *s*-$SrTiO_3$ (280 Ω) > *b*-$SrTiO_3$ (40 Ω) > TiO_2 (18 Ω) in terms of R_{CT} according to Figure 3-12b. The large value of R_{CT} for *s*-$SrTiO_3$ results in slow recombination between conduction band electrons and I_3^-. The I_3^- is formed at the counter electrodes and diffuses into mesoporous metal oxide films. This result is consistent with slower back electron transfer for *s*-$SrTiO_3$ than TiO_2 presented previously by nanosecond TA. Under light illumination in Figure 3-12c, *s*-$SrTiO_3$ (110 Ω) > *b*-$SrTiO_3$ (20 Ω) > TiO_2 (12 Ω) in terms of R_{CT}. Triiodide ions are formed by oxidized dye regeneration on metal oxide electrode surface. Consequently, R_{CT} values for all three metal oxides are reduced in the light than dark condition. Additionally,

high values of R_{CT} lead to pronounced reduction in the photocurrent for *s*-$SrTiO_3$, and *b*-$SrTiO_3$, giving rise to barely discernable current density in J-V curve and low IPCE value for $SrTiO_3$ photoanodes. It is noticeable that the low current density for SrTiO3 maybe also ascribed to a small electron injection yield from ZnPC into $SrTiO_3$ at ultrafast time scale (< nsc) due to high conduction band level compared to TiO_2.

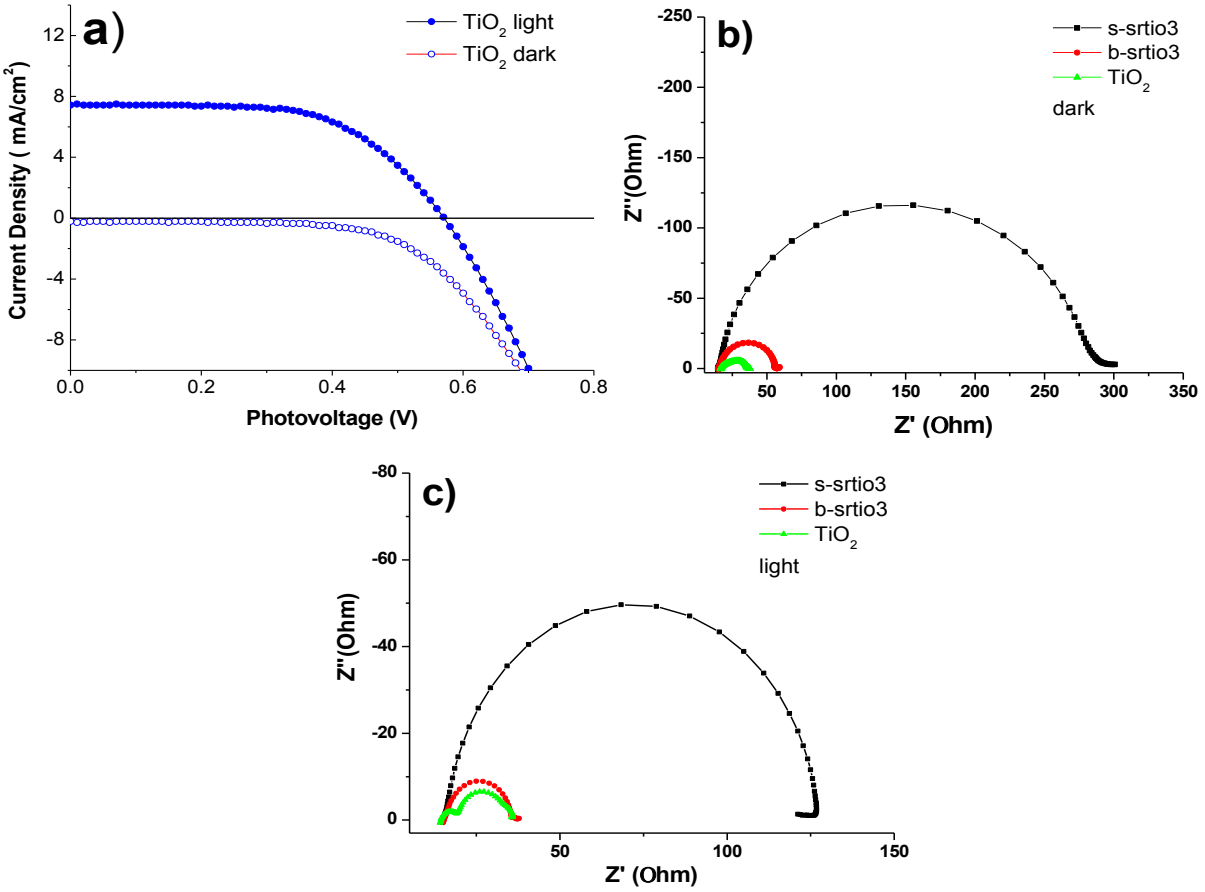

Figure 3-12. (a)Typical J–V curves of DSSCs for TiO_2 sensitized with **ZnPC** under 100 mW/cm^2 AM 1.5 G illumination and under dark, respectively. The area of both devices is 0.36 cm^2. Nyquist plots of representative EIS data at 700 mV forward bias in the dark (b) and light (c, 100 mW/cm^2 AM 1.5 G illumination) condition for DSSCs for TiO_2, *s*-$SrTiO_3$, and *b*-$SrTiO_3$ sensitized with **ZnPC.**

3.4 Conclusion

In this chapter, systematic comparison of $SrTiO_3$ to TiO_2 as photoanodes in DSSCs was conducted by using a znic porphyrin dye, ZnPC, with a high excited state redox potential. Two types of $SrTiO_3$ photoanodes and anatase TiO_2 films were carefully examined after ZnPC sensitization. Their energy levels and band positions were right aligned that was favorable for efficient electron injection from ZnPC into metal oxides. Nanosecond transient absorption further revealed the interfacial dynamics for ZnPC on $SrTiO_3$ and TiO_2, in which electron injection might be primarily from singlet ZnPC excited state to $SrTiO_3$ while from both singlet and triplet ZnPC excited states to TiO_2 conduction band. In addition, $SrTiO_3$ displayed slower back electron transfer than TiO_2 in the sense of better charge separation. However, ZnPC sensitized DSSCs on TiO_2 showed IPCE and energy conversion efficiency tremendously higher than on $SrTiO_3$, which could be ascribed to suppression of photocurrent from large interfacial charge transfer resistance between conduction band of $SrTiO_3$ and electrolyte (I^{3-}, etc.). Therefore, it may be proposed that the key for $SrTiO_3$ as an efficient photoanodes lies in improving electron transport property by appropriate fabrication techniques.

3.5 REFERENCES

(1) Gouterman, M. *Journal of Molecular Spectroscopy* **1961**, *6*, 138.

(2) Watson, D. F.; Marton, A.; Stux, A. M.; Meyer, G. J. *J. Phys. Chem. B* **2003**, *107*, 10971.

(3) Imahori, H.; Hayashi, S.; Hayashi, H.; Oguro, A.; Eu, S.; Umeyama, T.; Matano, Y. *J. Phys. Chem. C* **2009**, *113*, 18406.

(4) Ishizuka, T.; Sinks, L. E.; Song, K.; Hung, S. T.; Nayak, A.; Clays, K.; Therien, M. J. *J. Am. Chem. Soc.* **2011**, *133*, 2884.

(5) Lee, S.-H. A.; Abrams, N. M.; Hoertz, P. G.; Barber, G. D.; Halaoui, L. I.; Mallouk, T. E. *J. Phys. Chem. B* **2008**, *112*, 14415.

(6) Song, W.; Glasson, C. R. K.; Luo, H.; Hanson, K.; Brennaman, M. K.; Concepcion, J. J.; Meyer, T. J. *J.Phys. Chem. Lett.* **2011**, *2*, 1808.

(7) Gallagher, L. A.; Serron, S. A.; Wen, X.; Hornstein, B. J.; Dattelbaum, D. M.; Schoonover, J. R.; Meyer, T. J. *Inorg. Chem.* **2005**, *44*, 2089.

(8) Ito, S.; Murakami, T. N.; Comte, P.; Liska, P.; Grätzel, C.; Nazeeruddin, M. K.; Grätzel, M. *Thin Solid Films* **2008**, *516*, 4613.

(9) Xu, G.; Huang, X.; Zhang, Y.; Deng, S.; Wei, X.; Shen, G.; Han, G. *CrystEngComm* **2013**, *15*, 7206.

(10) Luo, H.; Song, W.; Hoertz, P. G.; Hanson, K.; Ghosh, R.; Rangan, S.; Brennaman, M. K.; Concepcion, J. J.; Binstead, R. A.; Bartynski, R. A.; Lopez, R.; Meyer, T. J. *Chem. Mat.* **2012**, *25*, 122.

(11) ;, E. B. J. R. M. *Impedance Spectroscopy: Theory, Experiment, and Applications, 2nd Edition; Chapter 4*; Wiley: NJ, 2005.

(12) Wang, G.; Wang, Q.; Lu, W.; Li, J. *J. Phys. Chem. B* **2006**, *110*, 22029.

(13) Zaban, F. F.-S. G. G.-B. J. B. P. B. A. *J. Electrochem. Soc.* **2003**, *150*, E293.

(14) Chen, J.-G.; Chen, C.-Y.; Wu, C.-G.; Lin, C.-Y.; Lai, Y.-H.; Wang, C.-C.; Chen, H.-W.; Vittal, R.; Ho, K.-C. *J. Mater. Chem.* **2010**, *20*, 7201.

(15) Lee, B.; Lee, C.-k.; Hwang, C. S.; Han, S. *Current Applied Physics* **2011**, *11*, S293.

(16) Gouterman, M. *The Porphyrins, Vol. 3: Physical Chemistry, Part A*; Academic Press: New York, 1978; Vol. 3.

(17) Milot, R. L.; Moore, G. F.; Crabtree, R. H.; Brudvig, G. W.; Schmuttenmaer, C. A. *J. Phys. Chem. C* **2013**, *117*, 21662.

(18) Butler, M. A.; Ginley, D. S. *J. Electrochem. Soc.* **1978**, *125*, 228.

(19) Rehm, D.; Weller, A. *Israel Journal of Chemistry* **1970**, *8*, 259.

(20) Minaev, B. *Spectrochimica Acta Part A: Molecular and Biomolecular Spectroscopy* **2004**, *60*, 3213.

(21) Kalyanasundaram, K.; Vlachopoulos, N.; Krishnan, V.; Monnier, A.; Graetzel, M. *J. Phys. Chem.* **1987**, *91*, 2342.

(22) Aono, S.; Okura, I.; Yamada, A. *J. Phys. Chem.* **1985**, *89*, 1593.

(23) Cui, X.; Zhao, J.; Yang, P.; Sun, J. *Chem. Commun.* **2013**, *49*, 10221.

(24) Moore, G. F.; Konezny, S. J.; Song, H.-e.; Milot, R. L.; Blakemore, J. D.; Lee, M. L.; Batista, V. S.; Schmuttenmaer, C. A.; Crabtree, R. H.; Brudvig, G. W. *J. Phys. Chem. C* **2012**, *116*, 4892.

(25) Moore, G. F.; Blakemore, J. D.; Milot, R. L.; Hull, J. F.; Song, H.-e.; Cai, L.; Schmuttenmaer, C. A.; Crabtree, R. H.; Brudvig, G. W. *Energy & Environmental Science* **2011**, *4*, 2389.

(26) Lindsey, C. P.; Patterson, G. D. *The Journal of Chemical Physics* **1980**, *73*, 3348.

(27) Rogers, J. E.; Nguyen, K. A.; Hufnagle, D. C.; McLean, D. G.; Su, W.; Gossett, K. M.; Burke, A. R.; Vinogradov, S. A.; Pachter, R.; Fleitz, P. A. *J. Phys. Chem. A* **2003**, *107*, 11331.

(28) Bergeron, B. V.; Kelly, C. A.; Meyer, G. J. *Langmuir* **2003**, *19*, 8389.

(29) Song, W.; Brennaman, M. K.; Concepcion, J. J.; Jurss, J. W.; Hoertz, P. G.; Luo, H.; Chen, C.; Hanson, K.; Meyer, T. J. *J. Phys. Chem. C* **2011**, *115*, 7081.

(30) Burnside, S.; Moser, J.-E.; Brooks, K.; Grätzel, M.; Cahen, D. *J. Phys. Chem. B* **1999**, *103*, 9328.

Chapter 4: Applications of High Surface Area Antimony-doped Tin Oxide Electrodes Templated by Graft Copolymers in Ruthenium Complexes Surface-bounded Electrochemical and Photoelectrochemical Catalysis

4.1 Introduction

Transparent conducting oxides (TCOs) have successfully been utilized in a wide range of optoelectronic and photoelectrochemical devices.[1,2] In comparison to flat TCOs, 3-dimentional mesoporous nanostructured TCOs (2 nm < pore diameter < 50 nm) are characteristic of high interfacial area exposed to electroactive species and fast drift electron transport rather than diffusive transport in traditional metal oxide semiconductors like TiO_2.[3,4] These properties bring mesoporous TCO electrodes with broad applications such as dye sensitized solar cells (DSSCs), electrochemical catalysis, and biochemical sensors.[5-9] Despite that Sn-doped In_2O_3 (ITO) has been the most popular TCO material, demands for finding alternatives to it have substantially increased due to the high cost and rarity of indium metal.[10] Antimony-doped tin oxide (ATO) is a promising alternative to ITO since it has high transparency with a large band gap (> 3.6 eV) and good electric conductivity.[11] Therefore, strategies toward 3-D mesoporous nanostructured ATO films are highly desirable. The most used synthetic route to obtain 3-D mesoporous ATO is based on inorganic metal precursors soft templated by organic surfactant molecules and amphiphilic copolymers through evaporation induced self-assembly (EISA).[12-14] In order to explore large-pore mesoporous materials, amphiphilic copolymers are chosen to structurally direct mesoporous metal oxide formation, driven by microphase separation of copolymers containing thermodynamically incompatible subunits. [1,2] In spite of the elegance of this

approach, it suffers from several limitations. Complications associated with mixed Sn and Sb precursors that often show fast rate for hydrolysis and condensation, making it difficult to control interaction with organic copolymers.[3] In addition, as obtained mesoporous structures are usually amorphous and thus require post annealing at elevated temperature to increase crystallinity, leading to a strain induced collapse of the original mesopores. [4] It apparently limits the choices of structure directing polymers for mesoporous ATO films to poly(ethylene-co-butylene)-b-poly(ethylene oxide) KLE copolymer, polyisobutylene-b-poly(ethylene oxide) copolymer, and pluronic block copolymer F127.[3,5] To overcome these weaknesses, mesoporous materials based on presynthesized well-defined ATO nanocrystals was proposed, which also allows a fine tune of doping level of metal oxides. Müller et al. have attained mesoporous ATO films with presynthesized small ATO nanoparticles through traditional sol-gel technique, which are further soft templated by F127 copolymer.[6] However, pluronic copolymers normally decompose at relatively low temperatures compared with high temperatures to maintain high crystallinity of metal oxides. Moreover, small PPO subunits in pluronic copolymers are unfavorable to large pore size.[4,7] Thus, it is highly demanded to explore non-pluronic copolymers with higher glass transition temperature, and better thermostability in the synthesis of ATO electrodes requiring larger mesopores.

In the present study, we aim at fabricating mesoporous ATO crystalline electrodes, for the first time, based on microwave assisted nanoATO crystals and a grafted copolymer, poly (vinyl chloride)-g-poly (oxyethylene methacrylate) (PVC-g-POEM) by a one pot atom transfer radical polymerization (ATRP). The use of this graft copolymer has already enabled generation of various TiO_2 electrodes with large mesopores in solid state dye sensitized solar cells (DSSCs).[8,9] In addition, even though ATO nanoparticles are able to synthesize via non aqueous

sol-gel route,[10] the microwave irradiation used in this report substantially accelerates the reaction from several hours to 20 min.

The newly synthesized transparent conductive mesoporous ATO film indicates rapid electron transfer and proves itself a suitable substrate for electrochemical catalysis as derivatized by a ruthenium water oxidation catalyst. Moreover, core–shell photoanodes, consisting of core of mesoporous conductive metal oxides and thin shell of wide-bandgap semiconductors, have been successfully applied to DSSCs and photoelectrochemical cell by taking advantage of fast electron transport in conductive core.[11-14] In this report, as obtained mesoporous ATO film deposited with a thin shell of TiO_2 by atomic layer deposition (ALD) are derivatized by a ruthenium chromophore, , working as a photocathode that generates H_2 in the presence of a reductive scavenger ethylenediaminetetraacetic tetra-anion ($EDTA^{4-}$) under light illumination

4.2 Experimental Section

4.2.1 Materials

Tin(IV) tetrachloride, antimony (III) acetate ($Sb(ace)_3$), anhydrous benzyl alcohol, poly(vinyl chloride) (PVC, Mw ~ 97,000 g/mol, Mn ~ 55,000 g/mol), poly(ethylene glycol) methyl ether methacrylate (POEM, Mn ~ 500 g/mol), 1,1,4,7,10,10-hexamethyltriethylenetetramine (HMTETA), 1-Methyl-2-pyrrolidinone (NMP), deuterated tetrahydrofuran, Lithium perchlorate (99.999 % trace metal basis), 70 % perchloric acid (99.999 %), ethylenediaminetetraacetic acid (EDTA) disodium salt dehydrate (ACS reagent), and copper(I) chloride (CuCl, 99 %) were purchased from Aldrich. CuCl was purified by stirring in glacial acetic acid overnight and rinsing with acetic acid, ethanol and acetone. Others were used as received. Metal precursors, NMP, and CuCl were stored inside glove box. Toluene, hydrogen chloride solution (HCl, 37 wt%), ether, acetonitrile, tetrahydrofurane (THF), and methanol

(MeOH) were ordered from Fisher Scientific. Distilled water was further purified using a Milli-Q Ultrapure water purification system.

4.2.2 Synthesis of PVC-g-POEM

The preparation of PVC-g-POEM was modified on the basis of reference [15]. PVC (3 g) was dissolved in 25 mL of NMP by stirring at 90 ^{o}C for 4 h. After cooling down to room temperature, 4.5 g or 7.5 g POEM and 0.195 mL HMTETA were added into the solution through a syringe under N_2 atmosphere and then degassed by three freeze-pump-thaw cycle. CuCl (0.06 g) was added during the final cycle when the contents were frozen in liquid nitrogen. The flask was back filled with nitrogen, sealed, and reacted at 90 ^{o}C for 18 h in oil bath. After polymerization, the resultant mixtures were diluted with THF, purified by a neutral Al_2O_3 column to remove the catalyst. Further purification involved repeating dissolving mixtures in THF and reprecipitating them in methanol three times. As obtained PVC-g-POEM graft copolymer G1 (starting material weight ratio for PVC: POEM = 3: 7.5) and G2 (starting material weight ratio for PVC: POEM = 3: 4.5) were obtained by filtration and dried in a vacuum oven overnight at room temperature.

The successful graft copolymerization of **G1**was confirmed using ^{1}H NMR spectroscopy in deuterated THF as presented in **Figure 4-1**. The strong peaks at around 4.5 ppm is attributed to the -CHCl group in PVC pointed by a. Peaks around 4.1 and 3.3 ppm were assigned to the ethylene oxide units pointed by b. and methyl group pointed by c. of POEM subunits.[16] The accurate molecular weight of PVC-g-POEM copolymer is hard to obtain, but can be roughly estimated based on the molar ratio of comonomer units to PVC repeat units as measured by NMR 1H NMR spectra. [17] Accordingly, $M_{n,\ PVC\text{-}g\text{-}POEM}$ for **G1** was calculated to be ~ 135,000

g/mol and PVC: POEM = 4:6 wt%. By the same method, $M_{n,\ PVC\text{-}g\text{-}POEM}$ for **G2** was estimated to be ~ 81,000 g/mol and PVC: POEM = 7:3 wt%.

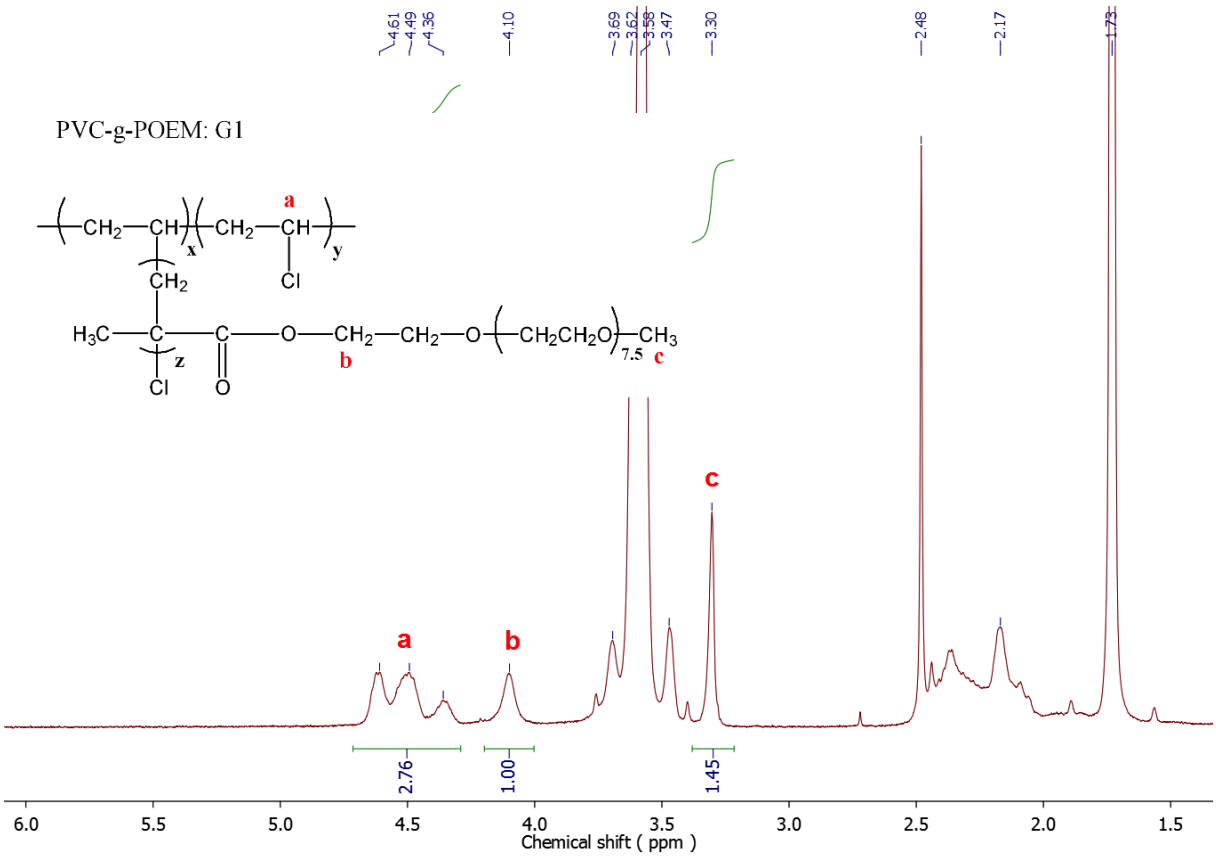

Figure 4-1. ^{1}H NMR spectra of the PVC-g-POEM graft copolymer, G1, with starting material weight ratio of PVC: POEM = 3: 7.5 in deuterated tetrahydrofuran.

Polydispersity index (PDI) of **G1** and **G2** were measured by the gel permeation chromatography (GPC) on a Waters 2695 Separations Module apparatus with a differential refractive index detector, using THF as the eluent. Calibration on the system was performed with polymethylmethacrylate standards (Polymer Laboratories) ranging from 875 g mol^{-1} to 1,677,000 g mol^{-1}. As obtained PDI for G1 and G2 were determined to be 1.48 and 1.55, respectively, displayed in Figure 4-2.

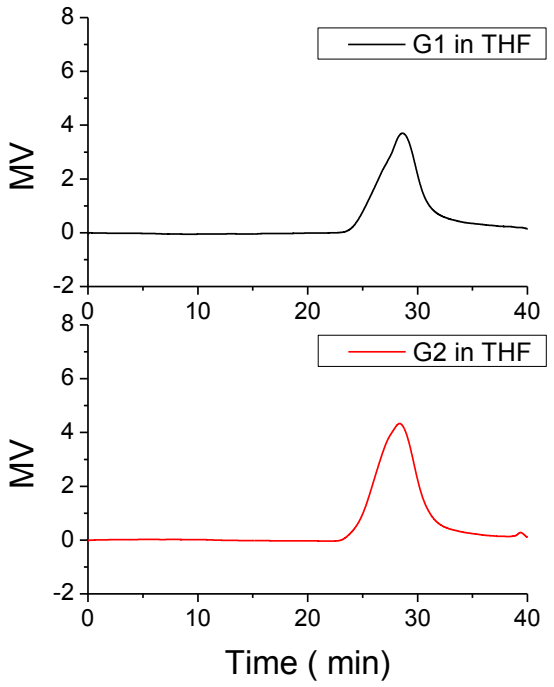

Figure 4-2. GPC trace of PVC-g-POEM copolymer G1 and G2, employing THF as the eluent.

4.2.3 **Mesoporous ATO films**

ATO nanocrystals with different antimony doping ratio are marked as x % ATO, where x= Sb/(Sb+Sn) (mol%). The total amount of antimony and tin was kept constant of 6.825 mmol for the metal precursors in all ATO nanoparticles synthesis. In a typical preparation of 10 % ATO nanocrystals, under glove box, 6.15 mmol $SnCl_4$ and 0.675 mmol $Sb(ace)_3$ were dissolved in 5 mL toluene, and the mixture was slowly added into 25 mL benzyl alcohol under continuous stirring for an hour. The clear solution was taken out from the glove box, and sealed in a microwave vial and heated in a microwave oven (Mars 230/60) with the maximum power set to 400 W, temperature at 200 ^{o}C, and run time to 20 min. The resulting white (pure SnO_2) or yellow monolith was collected by decanting the vessel. This monolith contained ~ 40-50 wt% organic content according to thermogravimetric (TGA) analysis (Figure 4-3a). For making mesoporous ATO films, monolith was washed with 30 mL acetone by glass pipette blowing and soaked for

another 20 min. The resultant nanoparticles were separated by centrifugation at 3000 rpm for 10 min, which had a residual organic content of 10-20 wt% after dried in air tested on TGA (Figure 4-3b). Nanocrystals for X-ray photoelectron spectroscopy (XPS) and Energy dispersive X-ray spectroscopy (EDS) analysis were furthered washed by two cycles of dispersion in acetone, ultrasonication, and centrifuge for 10 min in each step.

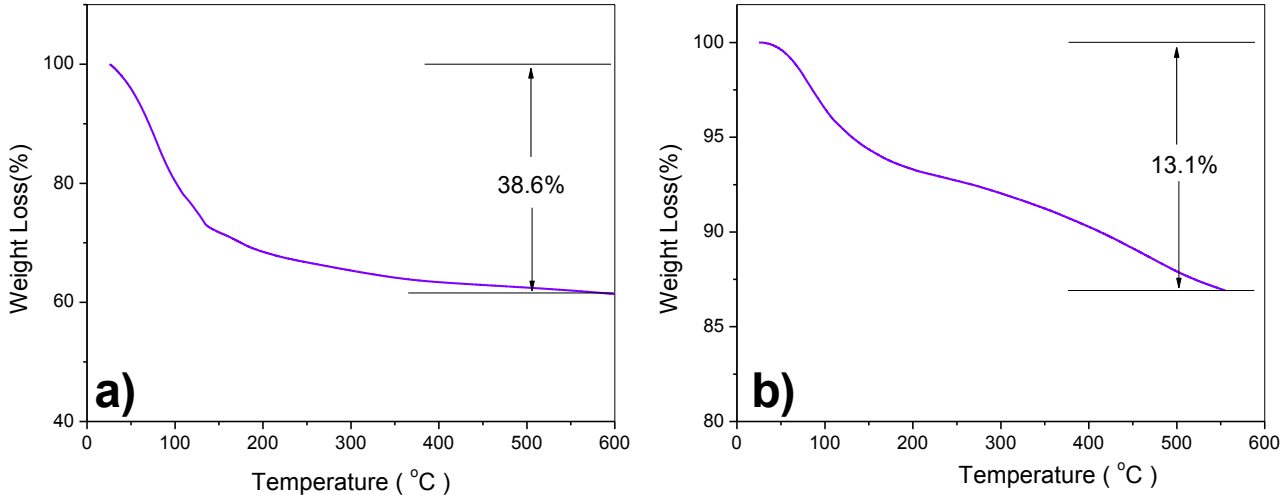

Figure 4-3. Thermogravimetric analysis (TGA) curves of 10 % ATO nanoparticles for (a) monolith without wash and (b) after acetone wash.

0.12 g PVC-g-POEM graft copolymers (**G1** or **G2**) was first dissolved in 1.4 mL of THF and then 0.4 g of the washed ATO nanocrystals were transferred to the polymer solution. 0.156 mL of concentrated HCl was slowly added to induce self-assembly of ATO and copolymer mixture, followed by constant stirring for 4 days. The final solution was transparent yellow to orange. The viscous paste was doctor bladed onto FTO substrate (fluorine-doped SnO_2, sheet resistance 15 Ω/□, Hartford Glass Co. Inc.) with the thickness controlled by layers of scotch tapes. After aging for 30 min, the ATO films were placed in a box oven and calcinated with a ramp of 5 ^{o}C min^{-1} to 350 ^{o}C and held for an hour, then heated to 550 ^{o}C with 2 ^{o}C min^{-1} and held for another hour. A typical film thickness is ~ 2 μm.

4.2.4 **Ruthenium Complexes Synthesis.**

$[Ru(bpy)_2(4,4'-(PO_3H_2)_2bpy)]^{2+}$ Cl_2 ([**RuP**]Cl_2, $(4,4'-(PO_3H_2)_2bpy$ is 4,4′-diphosphonato-2,2′-bipyridine) was prepared by previously published procedures. [18] $[Ru^{II}(Mebimpy)(4,4'-(PO_3H_2)_2bpy)(OH_2)]^{2+}$ (**1-PO_3H_2**, shown in Figure 4-4.) was synthesized by multiple steps based on literature [19] as described below.

Ru(Mebimpy)(4,4'-(H_2O_3P)$_2$-bpy)(Cl)(Cl): $((Mebimpy)(Cl)Ru)_2Cl_2$ [19] (0.29 mmol) and 4,4'-$((C_2H_5O)_2PO)_2$-bpy [18] (0.58 mmol) were suspended in 30 mL of 2:1 EtOH:H_2O, followed by degassing by argon bubbling. The mixture was then transferred to microwave at 160ºC for 30 min. The resulting mixture was filtered hot and the filtrate was evaporated to dryness by rotary evaporation. The obtained solid was dispersed in 35 mL dry acetonitrile that was pretreated with anhydrous $MgSO_4$ overnight. The solution was degassed by N_2 for 30 min first, then quickly injected with bromotrimethysilane (TMS-Br, 2.436 mmol) by syringe. The mixture was heated at 60 ºC under N_2 for 3 days. 20 mL methanol was added into the solution after cooling down to room temperature. After stirring for two hours, solid was dried by rotary evaporation, washed with ether and placed in a vacuum oven overnight. Yield: 78 %.

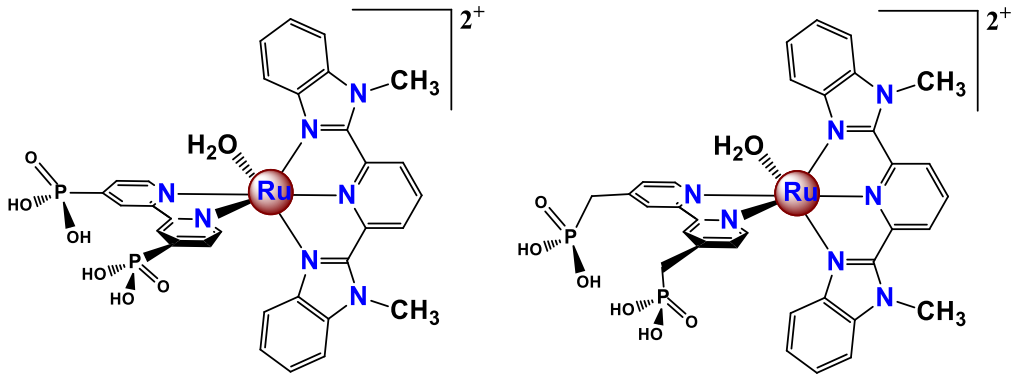

1-PO_3H_2 **2-PO_3H_2**

Figure 4-4. Molecular structures of **1-PO_3H_2** and **2-PO_3H_2**.

$[Ru^{II}(Mebimpy)(4,4'-(PO_3H_2)_2bpy)(OH_2)]^{2+}(PF_6)_2$ $[(1-PO_3H_2)$ $(PF_6)_2]$: Ru(Mebimpy)(4,4'-$(H_2O_3P)_2$-bpy)(Cl)(Cl) solid (440 mg) was added 4 mL neat triflic acid to cover the stir bar and kept stirring for 3 hours. Two equivalents of ascorbic acid dissolved in 3 mL water were slowly added to avoid precipitation of non-reduced complex. After addition of 3 mL saturated NH_4PF_6 aqueous solution, the flask was transferred to refrigerator overnight. The crude product was isolated by filtration, washed with ether and water. The solid was further purified by size exclusion chromatography (Sephadex LH-20) with 1:1 MeOH:H_2O as eluent. Similar fractions (based on UV/Vis absorption spectroscopy) were combined, and the solvent was concentrated by rotary evaporation and set aside for 2 days. The dark red micro-crystalline solid was collected by filtration and dried in a vacuum oven. Yield: 45 %. ^{1}H NMR (400 MHz, N,N-dimethylformamide-d7): 10.23 (m, 1H), 9.82 (m, 1H), 9.358 (d, J = 14.4 Hz, 1H), 8.87-9.25(m, 3H), 8.47 (m, 2H), 7.55-7.29 (m, 3H), 7.1 (m, 3H), 6.32 (m, 3H), 4.64 (s, 6H, 2CH_3, Mebimpy).

4.2.5 Derivatization of Mesoporous nanoATO films.

Stable phosphonate surface binding of the catalyst **1-PO_3H_2** on nanoATO films occurred following immersion of the nanoATO|FTO electrodes in 50 μM catalyst in methanol for 4 hours. The obtained electrodes were soaked in 0.1 M $HClO_4$ overnight before use. NanoATO|TiO_2 core shell films were derivatized by soaking in 0.2 mM **RuP** in a 0.1 M $HClO_4$ aqueous solution overnight, followed by soaking for an additional 12 h in 0.1 M $HClO_4$ to remove any possible **RuP** aggregates.

4.2.6 Atomic layer deposition (ALD).

ALD was performed in a Savannah ALD system from Cambridge Nanotech (Cambridge, MA) with Tetrakis(dimethylamido)titanium (TDMAT) (Sigma-Aldrich) as precursor. The TiO_2 layers were deposited at 130 °C using exposure times of 60 s for both TDMAT (0.25 s pulse) and

water (0.015 s pulse), with 120 s of nitrogen between each pulse. ~ 1.9 nm and 3.5 nm TiO2 shells, on the same nanoATO core, were prepared by 30 and 50 deposition cycles.

4.2.7 **Characterization.**

^{1}H NMR measurements were performed with a 400 MHz Bruker NMR spectrometers (AVANCE-400). X-ray diffraction (XRD) measurements were carried out on a Rigaku Multiflex diffractometer in theta-two theta mode using Cu K_{α} radiation (λ = 1.5418 Å). UV-vis absorption spectra were recorded on an Agilent Technologies Model 8453 diode-array spectrophotometer. Electrochemical measurements were performed on a CH Instruments 601 potentiostat with a platinum wire counter electrode and a saturated calomel electrode (SCE) or Ag/AgCl reference electrode. Morphology analysis was conducted by a JEM 100CX-II transmission electron microscope (TEM), a JEOL 2010F FasTEM for high resolution TEM images (HRTEM), and a focused ion beam (FIB) system (FEI Helios 600 Nanolab) for scanning electron microscopy (SEM). Thermogravimetric analyses (TGA) were recorded on a Perkin Elmer Pyris 1 TGA apparatus. Particle size distribution were tested by dynamic light scattering (DLS) using a nano ZS zetasizer (Malvern Instruments). Attenuated total reflectance Fourier transform infrared spectroscopy (ATR-FTIR) was performed on a Bruker ALPHA FT-IR spectrometer. Nitrogen adsorption measurement was obtained on a Quantachrome Autosorb-1C. Four probe resistivity measurement of nanoATO films were done on a keithley 4200-SCS semiconductor characterization system.

X-ray photoelectron spectra (XPS) were performed on a Kratos Analytical Axis UltraDLD spectrometer with monochromatized X-ray Al Kα radiation (1486.6 eV) of an analysis area of 300×700 μm^2. A survey scan was first performed with a step size of 1 eV, a pass energy of 80 eV, and a dwell time of 200 ms. High resolution scans were then taken for each element present with

a step size of 0.1 eV and a pass energy of 20 eV. The binding energy for all peaks was referenced to the C 1s peak at 284.6 eV. The recorded photoelectron spectra were fitted using mixed Gaussian/Lorentzian profiles, and the concentration of excited surface atoms was determined by measuring the integral intensity of the peaks under study after subtracting the background counts. The amount of antimony doping on ATO nanomaterials was evaluated by deconvolution of the spectrum using Kratos Vision software after background subtraction with the Shirley method. Energy dispersive X-ray spectroscopy (EDS) was obtained on a Hitachi S-4700 SEM system.

Illumination was provided by a spectral light engine from Lumencor (λ_{max} = 445 nm, 20 nm bandwidth, output ~ 1-100 mW cm^{-2}). The light source was integrated with a Newport optical fiber and a focusing/imaging beam probe. The irradiation beam diameter was 10 mm. Photocurrents with applied bias were performed by a Model 601D Series Electrochemical Workstation (CHI).

Photoelectrochemically evolved hydrogen was quantified by headspace gas analysis on a gas chromatography (GC, model: Varian 450-GC) with a molecular sieve column and a PDHID detector. Gaseous samples (0.6 mL) were drawn from the headspace by a gas-tight 0.5 mL syringe (Vici) and injected into the GC. Calibration curve for H_2 was determined separately. 20 μL methane was injected prior to photo excitation as internal standard.

4.3 Results and Discussion

4.3.1 Synthesis of ATO nanocrystals under microwave irradiation

ATO nanoparticle synthesis was based on a microwave assisted non-aqueous sol-gel methodology that is advantageous for slow sol-gel hydrolysis and condensation of metal precursors in the absence of water.[20,21] In this procedure, benzyl alcohol was chosen in that it serves as not only a good nucleophilic attacking agent to react with a variety of metal precursors,

but also a suitable solvent for microwave reaction due to a high boiling point and high dielectric loss factor. [22-24] Although few studies employed microwave energy for ATO nanoparticles preparation, ATO nanocrystals with different Sb doping ratio were successfully obtained by microwave irradiation that substantially reduced reaction time from several days or hours[10,25] to 20 min with $SnCl_4$ and $Sb(acetate)_3$ as precursors in this report.

As shown in Figure 4-5a., small 8 % ATO nanoparticles are only loosely agglomerated, characteristic with a narrow size distribution. The average size of the particles is determined to be ~ 3.2 nm from TEM that is consistent with the DLS size distribution peaking at 3.1 nm. A further increase in temperature (from 150 ^{o}C to 190 ^{o}C) and reaction time (from 20 min to 60 min) had little effect to enlarge particle size (Figure 4-6), probably resulting from high concentration of initial nuclei centers under such rapid thermal/kinetic process. Similarly, small monodispersed nanoparticles were synthesized with Sb % ranging from 0 % to 15 %. The corresponding X-ray diffraction (XRD) patterns (Figure 4-5b.) are assigned to the cassiterite structure of SnO_2 (PDF No. 41-1445).Therefore, SnO_2 cassiterite can accommodate up to 15 % Sb dopants without inclusion of other crystalline phase. The broadening of XRD peaks is consistent with the small size of ATO nanoparticles.

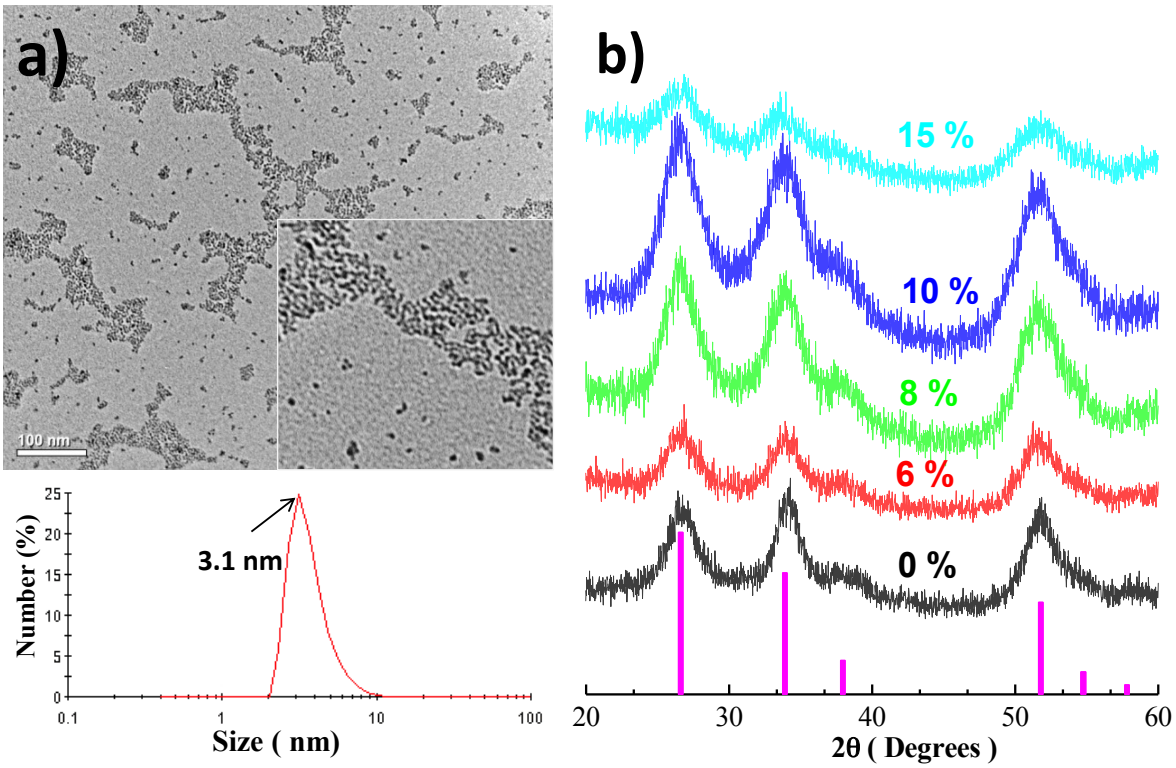

Figure 4-5. (a) Morphology and size of 8 % ATO nanoparticles. The upper: TEM of ATO nanoparticles at low and high magnification (inset) after dispersion in THF on a copper grid. The below: size distribution of the 8 % ATO nanoparticles in THF from DLS measurement. (b): X-ray diffraction diagrams with varying antimony content. The bars below XRD patterns indicate the position and diffraction lines of SnO_2 cassiterite ($P4_2/mnm$, JCPDS File No. 41-1445). All nanoparticles were prepared at 150 ^oC by microwave irradiation for 20 min.

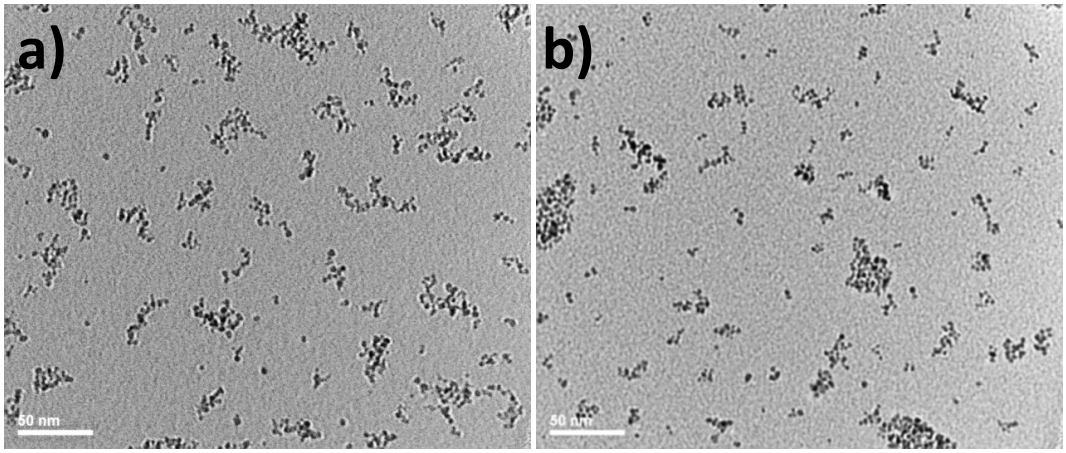

Figure 4-6. TEM image of 10 % ATO nanoparticles obtained by microwave irradiation at 190 ^{o}C for 20 min (a) and 60 min (b).

The existence of only Sn, Sb and O with a small amount of residual Cl in ATO nanocrystals with 6 %, 8 %, 10 % and 15 % antimony doping is clarified by the overview of XPS spectra shown in Figure 4-7. The binding energies at 487.4 and 496.0 eV are attributed to Sn $3d_{5/2}$ and Sn $3d_{3/2}$ respectively. Since the peaks of O 1s overlap with Sb $3d_{5/2}$ at ~ 531 eV, Sb $3d_{3/2}$ peaks are employed to quantify antimony content by deconvolution into two Gaussian lines centering at 540.7 eV for Sb^{5+} and 540.0 eV for Sb^{3+}, respectively. The total antimony doping content from XPS analysis is in good agreement with EDS method (shown in Table 4-1), demonstrating that the actual Sb molar ratio in ATO nanoparticles were well-controlled by the starting antimony and tin precursors and that the relative homogeneous distribution of Sb dopants without significant surface enrichment inside ATO nanocrystals (see Table 4-2). Furthermore, the coexistence of Sb^{5+} and Sb^{3+} with ~ 20 % excess of Sb^{5+} in ATO nanoparticles provide evidence for good conductivity due to net free donor electron as Sb^{5+} substitute for Sn^{4+} ions introduces a shallow donor level close to the conduction band of SnO_2, while the Sb^{3+} doping forms a shallow acceptor level close to the valence band. [26] As synthesized ATO

nanocrystals were yellowish, that might be caused by intervalence transition between Sb^{5+} and Sb^{3+}.[27]

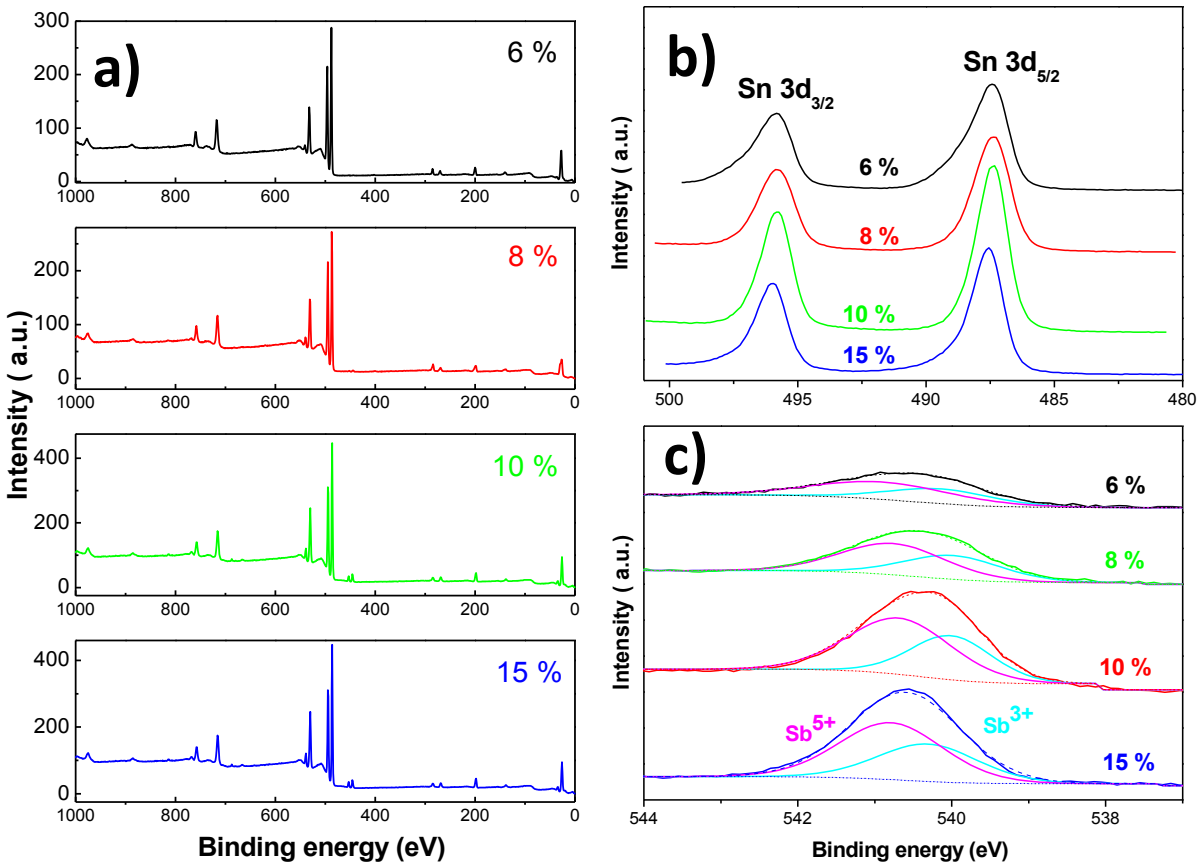

Figure 4-7. XPS results of as synthesized ATO nanoparticles with varying Sb doping ratio from 6 -15 % at 150 ^{o}C for 20 min under microwave irradiation. (a): overview XPS spectrum of ATO nanoparticles. High resolution scans of (b) Sn 3d doublet and (c) Sb $3d_{3/2}$ of ATO nanoparticles. The solid lines represent experimental results, the dot lines indicate background, and the dash lines correspond to Gaussian peak fitting. The Sb^{5+} and Sb^{3+} peaks are drawn in magenta and cyan, respectively.

Table 4-1. EDS data of 10 % ATO nanoparticles as an example.

Element	Weight %	Atomic %
C K	1.02	2.91
N K	1.77	4.32
O K	32.36	69.31
Cl K	7.06	6.82
Sn L	52.44	15.14
Sb L	5.36	1.51
Totals	100.00	

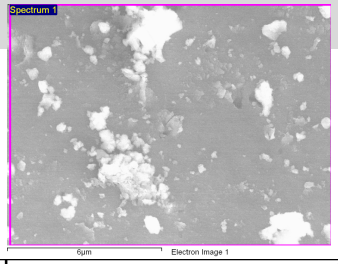

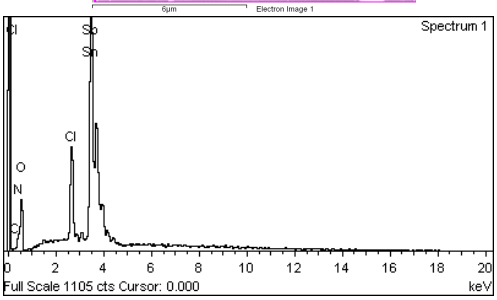

Table 4-2. Properties of ATO nanoparticles with different Sb doping levels.

Sb % in precursor solution (mol %)	Sb % in ATO nanoparticles (mol %)		Molar Fraction of Sb^{3+} and Sb^{5+} atoms % [a]		Mesoporous ATO films templated by PVC-g-POEM resistivity Ω.cm [b]	
	By XPS	By EDS	Sb^{5+}	Sb^{3+}	**G1**	**G2**
6	5.6	6.2	61.3	38.7	34	54
8	7.8	8.2	58.6	41.4	44	58
10	9.9	10.0	61.7	38.3	59	80
15	12.5	14.6	61.2	38.8	88	108

[a]: Determined from XPS. [b]: films calcinated at 550 ^{o}C for 1 hour. Determined from four probe resistivity measurements.

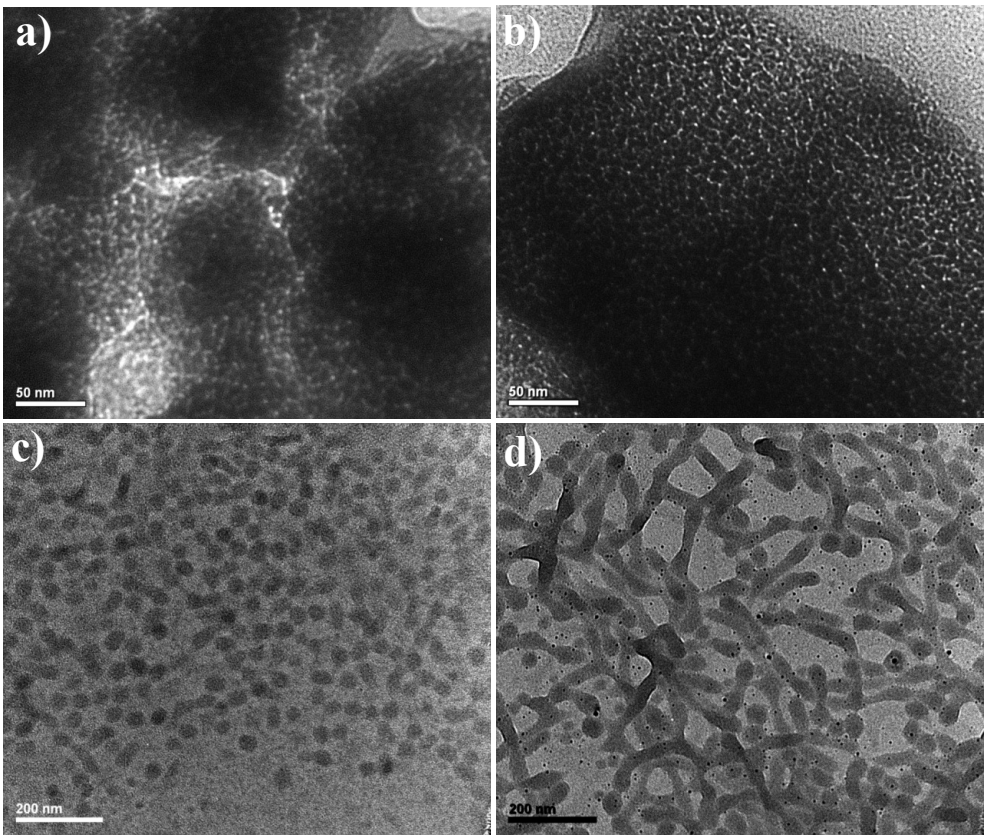

Figure 4-8. TEM images of the PVC-g-POEM graft copolymer; (a) **G1** and (b) **G2** prepared from pure THF; (c) **G1** and (d) **G2** prepared from mixture solution of THF: HCl/ H_2O = 18:1 volume ratio.

Amphiphilic PVC-g-POEM graft copolymers **G1** and **G2** of different PVC to POEM ratios were synthesized through atom transfer radical polymerization (ATRP) (Supporting information). The microphase separation of hydrophilic POEM side chains(glass transition temperature, T_g= -58 ^oC) and hydrohobic PVC main chains(T_g = 70 ^oC)[28] drove PVC-g-POEM self-assembly to nano micelles in the presence of THF, a good solvent for both PVC and POEM chains (solubility parameter, δ , δ_{THF} = 9.5, δ_{PVC} = 9.6 and δ_{POEM} = 10.8 $cal^{1/2}$ $cm^{-3/2}$) and HCl/H_2O, a poor solvent for PVC but a relatively good solvent for POEM domains (δ_{H2O} = 23.5 $cal^{1/2}$ $cm^{-3/2}$) (Figure 4-8.). Accordingly, both PVC and POEM chains were highly stretched in

THF, while introduce of HCl/H_2O selectively reduced swelling of PVC chains owing to increased interfacial energy between PVC and solvent, forming micelles with PVC core and POEM corona. The small size difference of micelles for **G1** (~ 34 nm) and **G2** (40 nm) might be ascribed to the same molecular weight of PVC main chains for the two compositions.

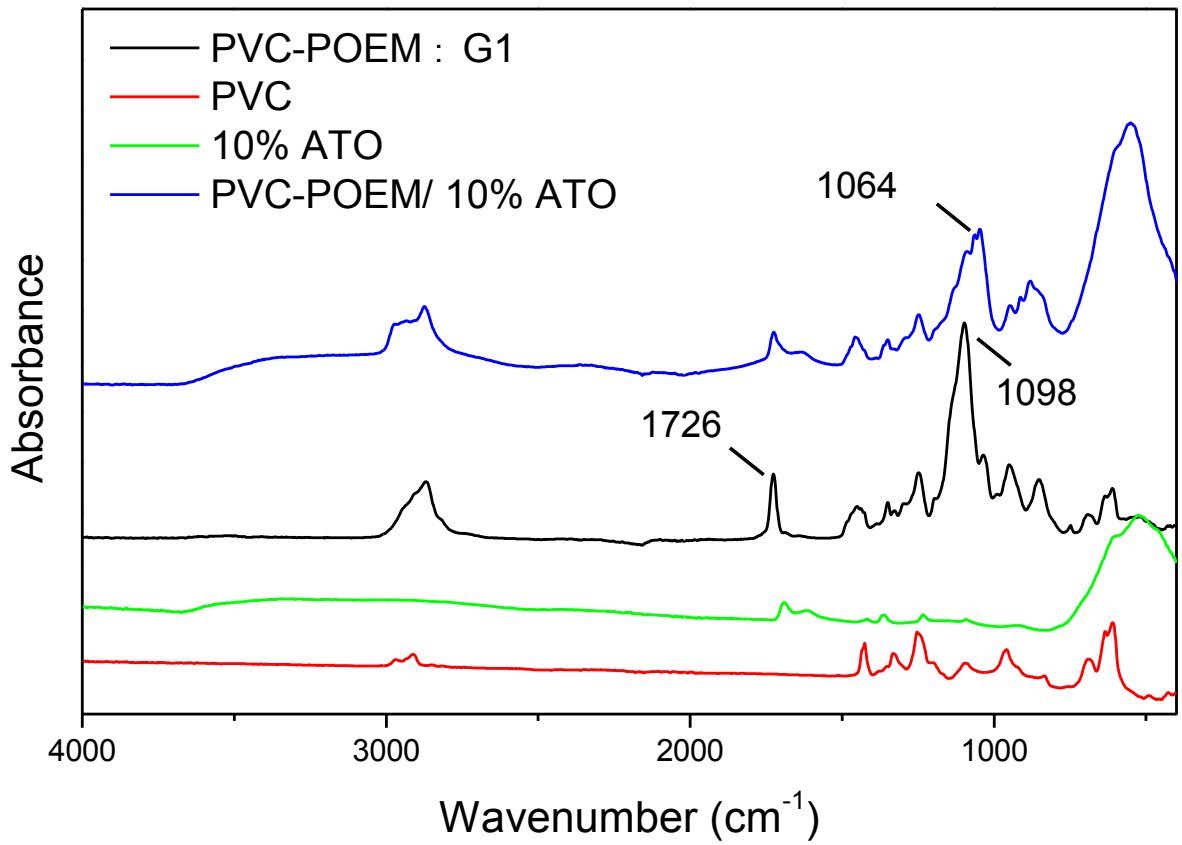

Figure 4-9. FTIR spectra of 10 % ATO nanoparticles, PVC-g-POEM graft copolymer **G1** and **G1**/10 % ATO nanoparticles composite before calcination.

4.3.2 **Mesoporous ATO films via PVC-g-POEM templating**

In order to make mesoporous films, freshly prepared ATO nanocrystals were added into THF solution predissolved with PVC-g-POEM. As-synthesized ATO nanocrystals had good hydrophilicity proved by TGA analysis, containing 10 -50 wt% organic content like adsorbed benzyl alcohol (Figure 4-3.), which was preferential for POEM side chains tethering to nanoparticle surface. Fourier transform infrared (FTIR) spectroscopic illustrated the ether (-O-) stretching band in POEM domain was shifted from 1098 to 1064 cm^{-1} when interacted with ATO nanoparticles, leaving other band nearly unchanged (Figure 4-9.).The templating of PVC-g-POEM originated from the adsorption enthalpy gain of POEM/ATO interaction and conformational entropy loss of POEM domain stretching to incorporate nanocrystals. [29]

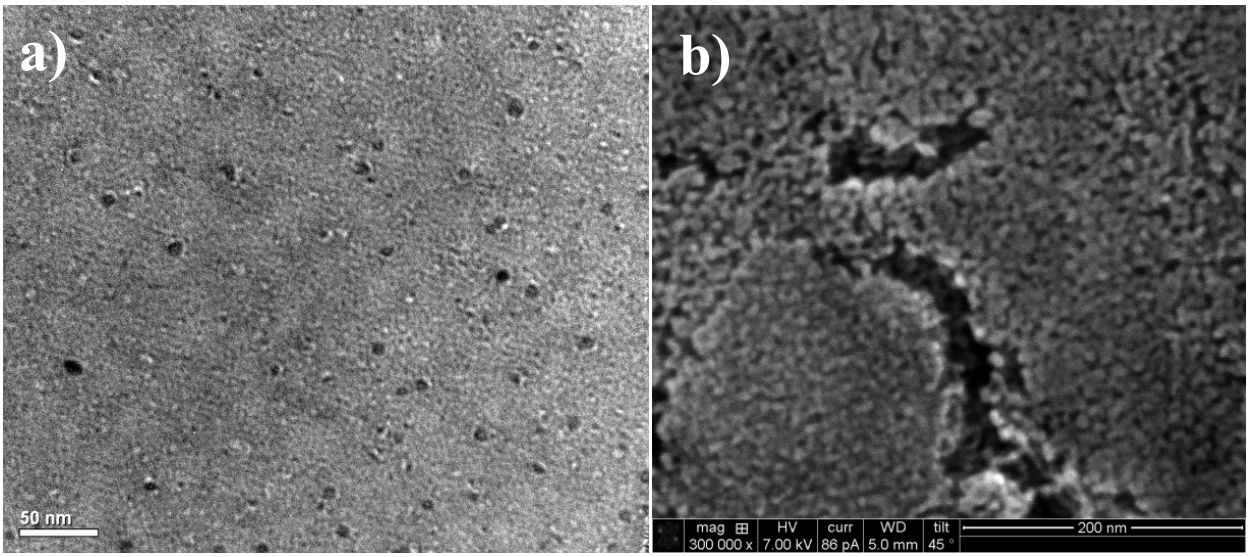

Figure 4-10. (a) TEM image shows disappearance of G1 micelles in mixture of benzyl alcohol, THF and HCl/H_2O, in which benzyl alcohol is over 50 v %. (b): SEM for worm-like ATO films with mainly small mesopores (< 6 nm) prepared from unwashed ATO nanocrystals.

Unwashed ATO nanocrystals brought difficulty in organic content removal and generated worm-like structure with small mesopores (< 6 nm), probably resulting from the disappearance

of PVC-g-POEM micelles with excess benzyl alcohol (Figure 4-10.). Washed ATO nanoparticles were assembled into ordered mesoporous films using PVC-g-POEM as templates, characteristic of large mesopores of 20-40 nm shown in Figure 4-11. Similar as small difference in micelles size, ATO films templated by **G1** and **G2** indicated close mesopore size after polymer removal and nanoparticles sintering at 550 ^{o}C.

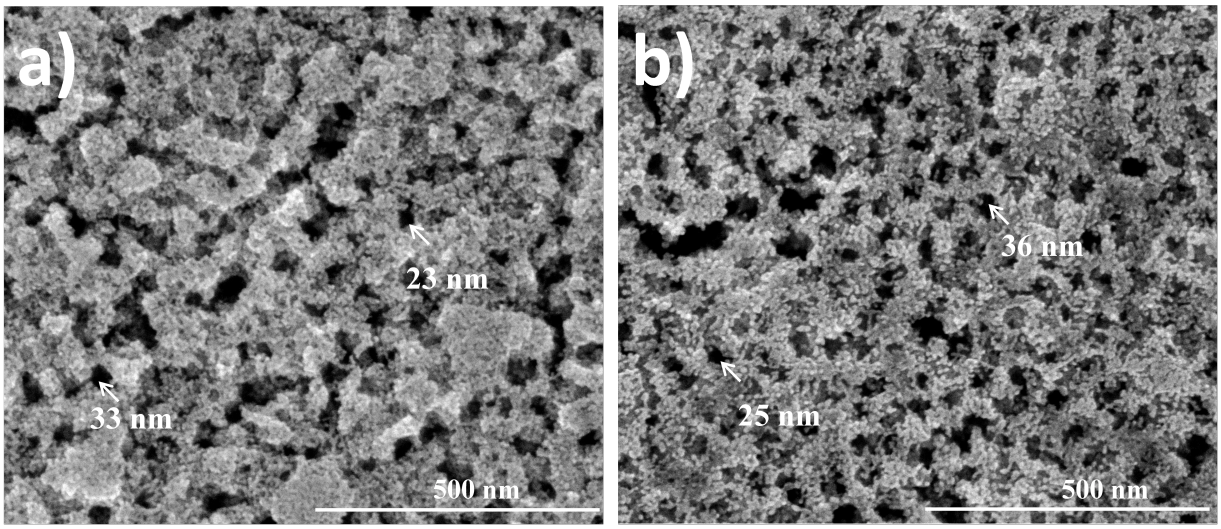

Figure 4-11. SEM images of ordered mesoporous ATO nanocrystal films using PVC-g-POEM as templates. (a) 10 % ATO film templating by **G1** and (b) 8 % ATO film templating by **G2**, respectively.

Moreover, in comparison to **G1**, **G2** templated films indicated smaller wall thickness due to lower content of POEM side chains and improved ordering resulting from higher fraction of POEM monomer tethered to ATO nanoparticles. The latter implies that enthalpy gain is the dominant driving force in the interplay between polymer and ATO.[30] In addition, the polymer/ATO assembly was influenced by antimony doping ratio that varied surface charge of ATO nanocrystals.[6] Mesoscopic aggregation increased in correspondence with the reduction of Sb dopant concentration, leading to decreased transparency from 15 % to 6 % ATO films.

Highly transparent mesoporous ATO films were able to prepare when Sb % is larger than 8 %, accompanied with a color transition from yellowish to bluish after calcination owing to a red to NIR plasma absorption from free electrons.[31] The onset of UV-Vis absorption at ~ 450 nm was consistent with literature value (Figure 4-12a).[32] Both crystallinity and size of ATO nanocrystal increased after calcination, ~ 5 nm at 400 and 550 ^{o}C estimated from XRD patterns by the

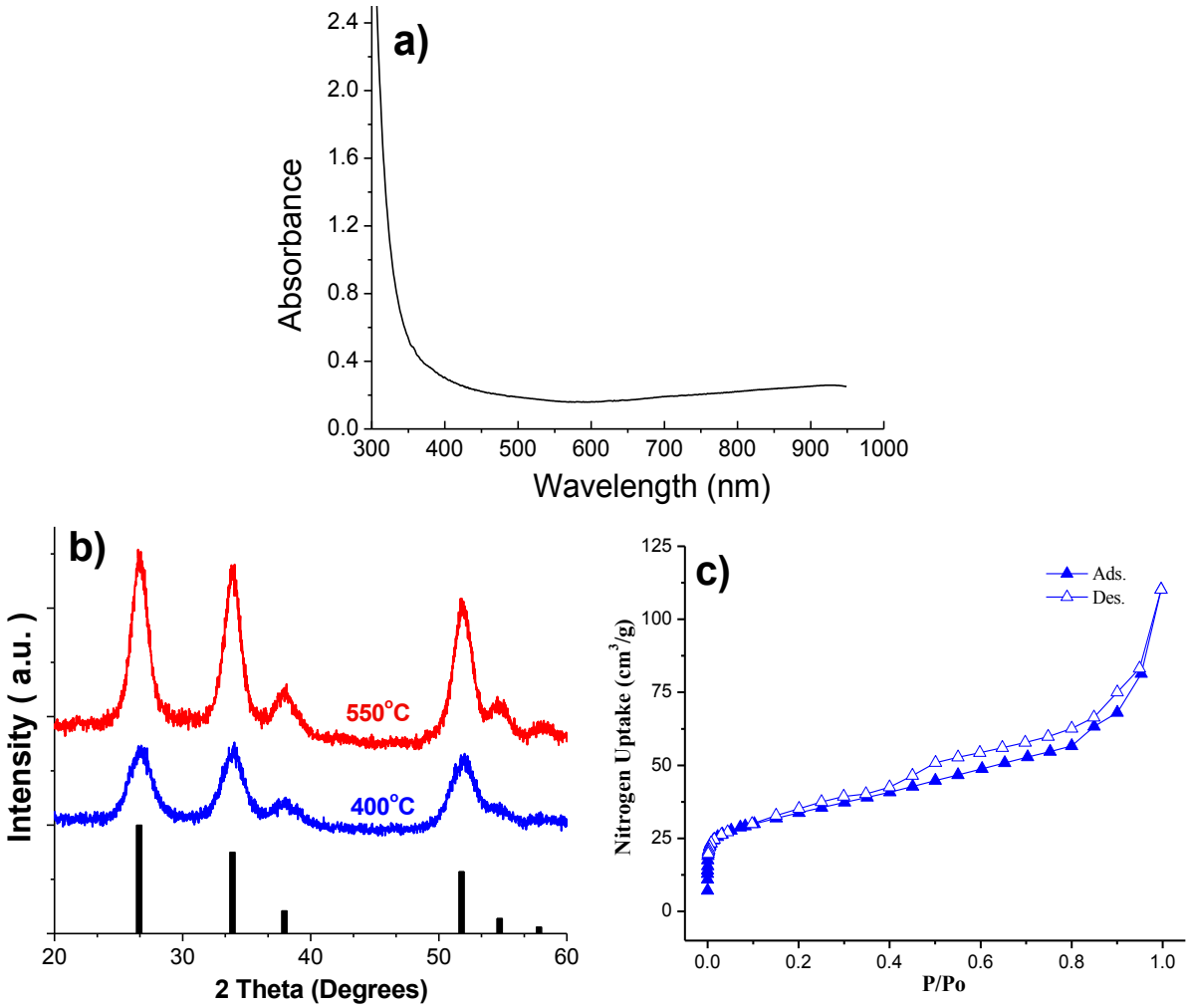

Figure 4-12. (a): UV-vis spectrum of blank FTO|*nano*ATO in pH 1 $HClO_4$. Sb % = 10 %. (b): XRD patterns for 8 % ATO nanocrystals calcinated at 400 and 550 ^{o}C for 60 min. (c): N_2 adsorption isotherms for mesoporous 10 % ATO templated by G1 after calcination at 550 ^{o}C.

Scherrer formula (Figure 4-12b). [3] According to N_2 adsorption isotherms in Figure 4-12c, mesoporous ATO had a high surface area of 120 m^2 g^{-1}, total pore volume 0.247 cm^3 g^{-1} and porosity of 62 % (density: 6.73 g/cm^3 [33]). The resistivity for mesoporous ATO films of varying Sb-doping levels was summarized in Table 4-2. by four probe measurements. The mesoporous ATO films had resistivity ranging from 30 to 110 Ω.cm, which were positively correlated with Sb doping concentration and in good agreement with literature values.[34] The smaller resistivity for **G1** templated ATO films than **G2** might originate from the thicker wall thickness inside mesoporous materials.

4.3.3 Mesoporous ATO films for water oxidation

Catalysts derivatized Sn(IV)-doped In_2O_3 (*nano*ITO) films have been proven to be successful substrates for water oxidation by taking advantage of fast electron transfer and optical transparency that allows monitoring UV-visible spectra of catalysts.[35,36] In order to testify *nano*ATO films as promising alternatives to *nano*ITO film in electrochemical catalysis, a surface bound catalyst [RuII(Mebimpy)(4,4'-$(PO_3H_2)_2$bpy)$(OH_2)]^{2+}$(**1-PO_3H_2**)(Mebimpy is 2,6-bis(1-methylbenzimidazol-2-yl)pyridine) (Figure 4-4) was studied by immobilizing onto *nano*ATO. **1-PO_3H_2** is a derivative of a well-known water oxidation catalyst, [RuII(Mebimpy)(4,4'-$(PO_3H_2CH_2)_2$bpy)$(OH_2)]^{2+}$ (**2-PO_3H_2**, Figure 4-4) with only anchoring group change.[37]

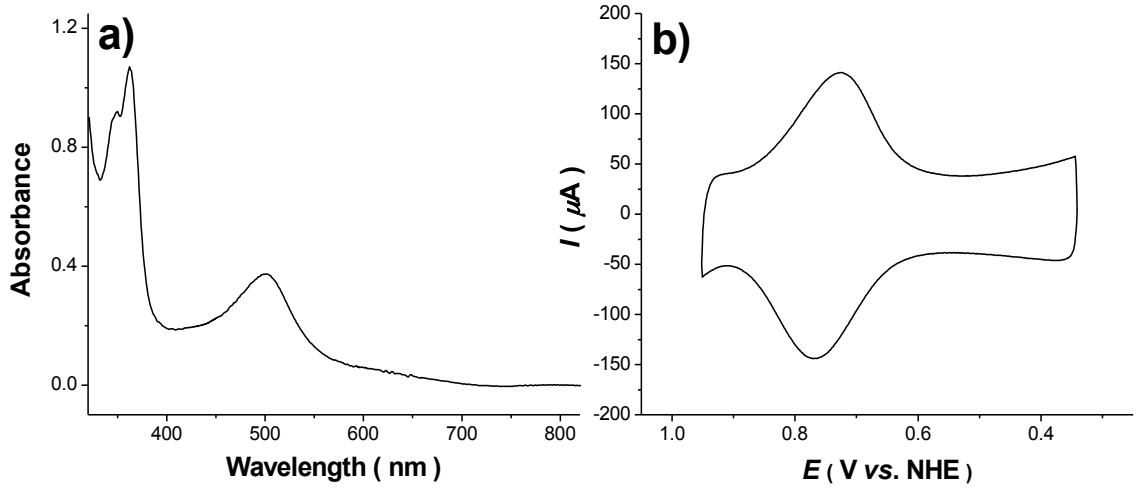

Figure 4-13.(a) UV-vis spectrum of FTO|*nano*ATO|1-PO_3H_2 in pH 1 $HClO_4$. (b) Cyclic voltammograms of FTO|*nano*ATO|1-PO_3H_2 at scan rate 10 mV/s in pH 5 acetate buffer. Sb % = 10 %.

After soaking *nano*ATO film in 50 μM **1-PO_3H_2** methanol solution, resulting UV-visible spectrum was dominated by the Metal-to-Ligand Charge Transfer (MLCT) band at λ_{max} = 498 nm (Figure 4-13a). The extent of surface loading for catalysts (Γ in mol. cm^{-2}) was calculated from UV-visible measurements by $\Gamma_{uv\text{-}vis}$=A (λ)/ (1000×ε (λ)), with A (λ) and ε (λ) the absorbance and molar absorptivities at wavelength λ. [38] For FTO|nanoATO|**1-PO_3H_2**, λ_{max} = 498 nm with $\varepsilon_{max} = 1.5 \times 10^4$ M^{-1} cm^{-1} in methanol were used for the surface analysis. Typical saturated surface coverages of 2.48×10^{-8} mol cm^{-2} (2 μm) were obtained after overnight exposure periods. Surface coverage values were also obtained by the integrated current-potential Ru^{III}-OH^{2+}/Ru^{II}-OH_2^{2+} wave in the absence of substrate by use of equation 4-1 with Q_{cv} the integrated charge, n(=1) the number of electrons transferred for the redox couple, F the Faraday constant, and A the area of the electrode.[39] Integration gave $\Gamma_{echem} = 1.58\times 10^{-8}$ mol cm^{-2}. (Figure 4-13b) Comparison of loadings from UV-visible and electrochemical measurements showed that 64 % of the catalyst sites on FTO|nanoATO|**1-PO_3H_2** are electroactive. This result demonstrated

that FTO|nanoATO electrodes contained more electrochemically accessible catalyst sites than RVC|nanoITO electrodes.[40] Thus, as-prepared high surface *nano*ATO electrodes allowed a large number of effective catalysts immobilized on surface that is comparable to *nano*ITO electrodes and two order of magnitude higher than flat FTO or ITO electrodes(~ 1.2× 10^{-10} mol cm^{-2}) .[35,37]

$$\Gamma = Q_{cv} / nFA \tag{4-1}$$

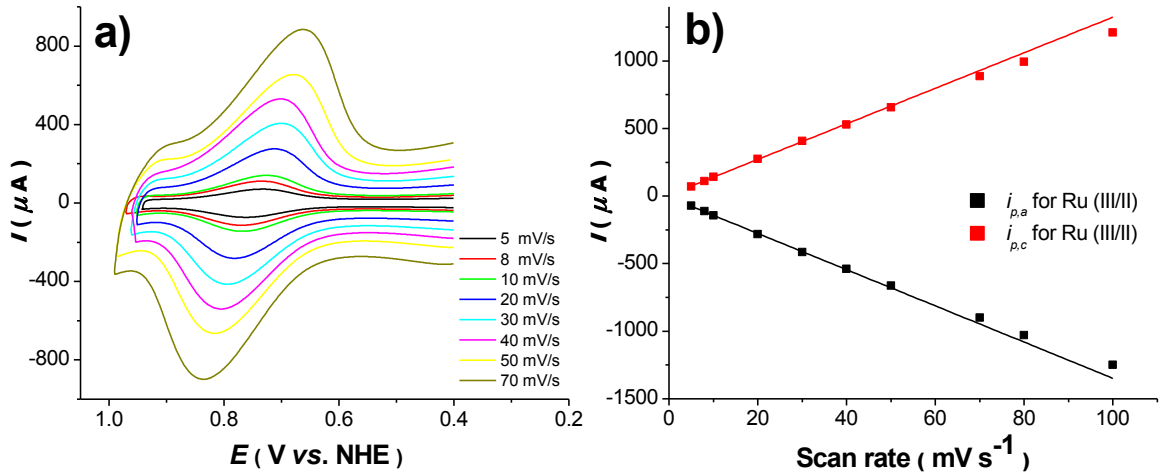

Figure 4-14. (a) Cyclic voltammograms in pH 5 acetate buffer (CH_3CO_2Na = 0.073 M; CH_3CO_2H= 0.027 M; I = 0.5 M) of FTO|*nano*ATO-Ru^{II}-OH_2^{2+} electrodes previously loaded with 1-PO_3H_2 at different scan rates. (b) Anodic and cathodic peak currents for the $Ru^{III/II}$ wave obtained in (a) as a function of the scan rate. Sb % = 10 %.

1-PO_3H_2 functionalized FTO|*nano*ATO electrodes exhibited the expected linear behavior of the peak current for Ru^{III}-OH^{2+}/Ru^{II}-OH_2^{2+} wave as a function of scan rate in the range from 5 to 50 mV/s in Figure 4-14. These results were consistent with kinetically facile electron transfer to and from surface confined redox couples.[1] Peak-to-peak splittings (ΔE_p= $E_{p,a}$ -$E_{p,c}$) were less than 50 mV at low scan rate(≤ 10 mV/s). At higher scan rates (≥ 70 mV/s), ΔE_p increased and peak current deviated from linear dependence on scan rate. Compared to **2-PO_3H_2** with $E_{1/2}$ ~

0.68 V,[2] Ru^{III}-OH^{2+}/Ru^{II}-OH_2^{2+} of **1-PO_3H_2** shifted positively to ~ 0.75 V that was due to the electron-withdrawing substituent effect of **-PO_3H_2** groups at the 4,4′-bpy positions. Sequential pH dependent wave appeared at 0.98 V for $Ru^{III}OH^{2+}$/Ru^{IV}=O^{2+} couples on the surface (

Figure 4-16a inset). Similar as **2-PO_3H_2**, this couple was kinetically inhibited by the kinetic requirement for proton loss from $Ru^{III}OH^{2+}$.

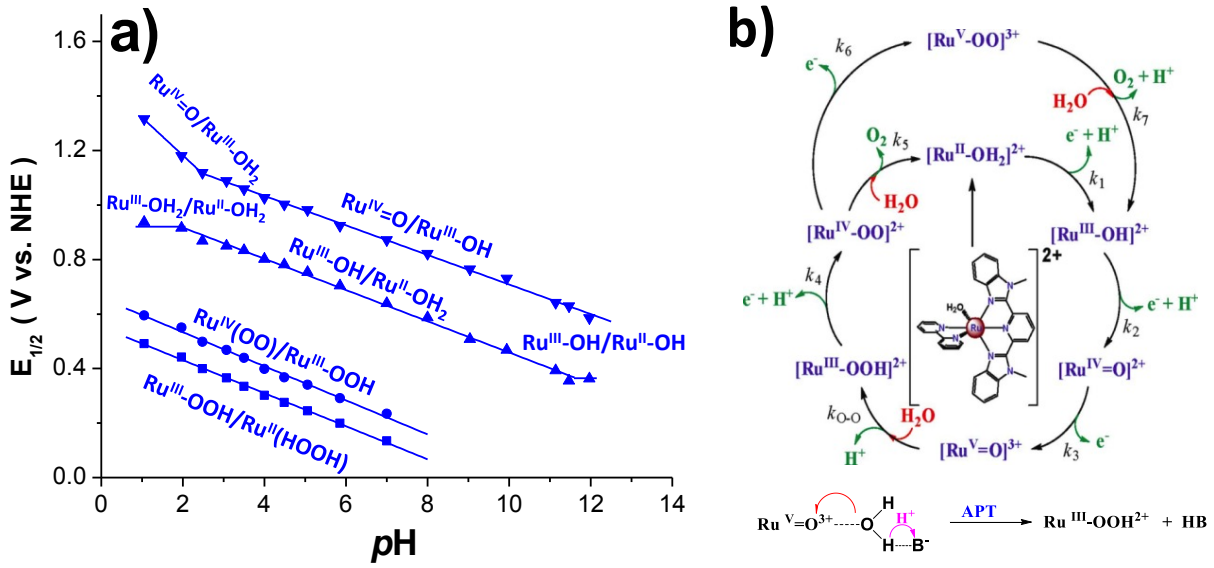

Figure 4-15. (a) Plots of $E_{1/2}$ vs pH for the $Ru^{III/II}$, $Ru^{IV/III}$, and $Ru^{V/IV}$ surface-bound couples at FTO|*nano*ATO|1-PO_3H_2) and for the peroxidic $Ru^{IV}(OO)^{2+}$/Ru^{III}-OOH^{2+} and Ru^{III}-OOH^{2+}/$Ru^{II}(HOOH)^{2+}$ redox couples following an oxidative scan passing 1.6 V vs. NHE. I = 0.5 (b) Mechanism of electrocatalytic water oxidation by the single site water oxidation catalyst.[37,41,42] Sb % = 10 %.

The narrow, skewed reduction wave at $E_{p,c}$ = 0.88 V arose from Ru^{IV}=O^{2+} re-reduction to $Ru^{III}O^{+}$ followed by rapid protonation to give $Ru^{III}OH^{2+}$.[2,5] As described earlier for **2-PO_3H_2**, new pH-dependent waves following an oxidative scan over catalytic onset appeared at $E_{1/2}$ = 0.25 and 0.34 V at the expense of Ru^{III}-OH^{2+}/Ru^{II}-OH_2^{2+} couple. These were assigned to long

lived peroxide couples Ru^{III}-OOH^{2+}/$Ru^{II}(HOOH)^{2+}$ and $Ru^{IV}(OO)^{2+}$/Ru^{III}-OOH^{2+}.[36,41,43] A pH-independent $Ru^{V}=O^{3+}$/ $Ru^{IV}=O^{2+}$ couple, slightly discernable at low pH, appeared after 1.6 V that was often the onset of a catalytic water oxidation wave, with catalytic current significantly larger than bare *nano*ATO film under the same condition.[43]

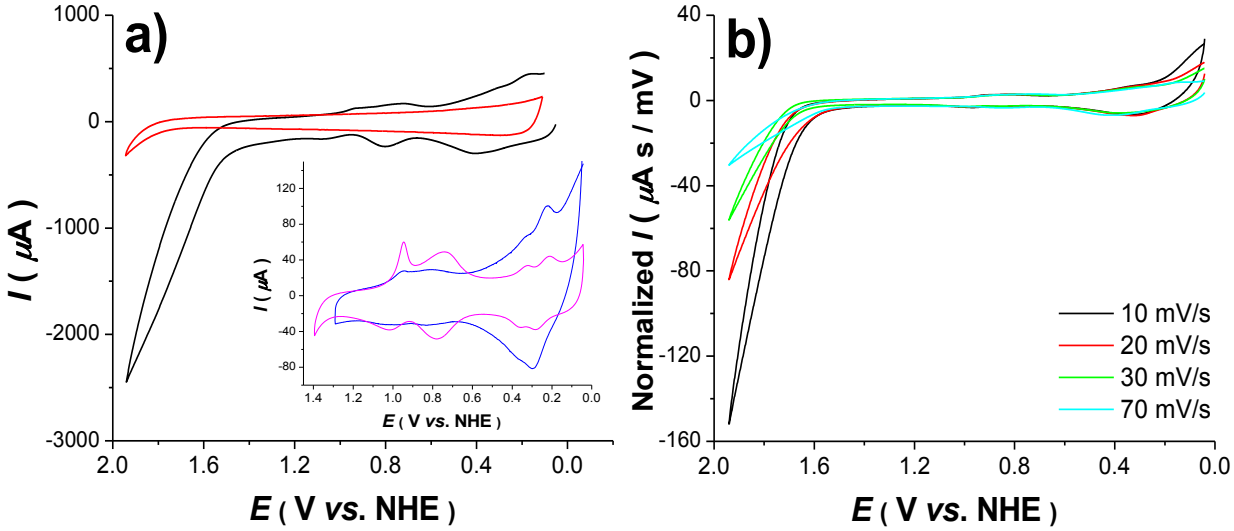

Figure 4-16. (a) Cyclic voltammograms in pH 5 acetate buffer (CH_3CO_2Na = 0.073 M; CH_3CO_2H = 0.027 M; I = 0.5 M) of FTO|*nano*ATO-Ru^{II}-OH_2^{2+} electrodes previously loaded with 1-PO_3H_2 at 50 mV/s (dark line). The red line is the FTO|*nano*ATO background under the same experimental conditions. The inset shows CVs of FTO|*nano*ATO|1-PO_3H_2 at pH 5 after scanning to 1.5 V (violet line) and scanning to 1.9 V (blue line) at 10 mV/s. (b) Normalized cyclic voltammogram of FTO|*nano*ATO|1-PO_3H_2 in pH 5 acetate buffer at different scan rates. The currents are normalized for scan rate, i/υ. Sb % = 10 %.

A Pourbaix diagram ($E_{1/2}$ vs. pH) for **1-PO_3H_2** bounded on nanoATO was summarized in Figure 4-15a. Normalizing scan rate (i_p , i/υ) in Figure 4-16b. , catalytic currents increased with decreasing scan rate that was in consistent with a rate limiting step prior to electron transfer on surface electrodes. According to electrochemical data for **1-PO_3H_2** |*nano*ATO, it is proposed that

1-PO_3H_2 functions similarly as **2-PO_3H_2** following a typical single site water oxidation mechanism with rate limiting O-atom transfer from $Ru^{V}=O^{3+}$ to H_2O in concerted with proton acceptor assisted Atom-proton transfer (**APT**) pathway shown in Figure 4-15b.[42,44]

$$\frac{i_c}{i_p} = \left(\frac{4RTn_{cat}\Gamma_c}{Fn_p{}^2\Gamma_p} \right) k_{obs} (\frac{1}{\upsilon}) \tag{4-2}$$

Where i_c is catalytic current at given potential, i_p is the surface couple peak current, k_{obs} is the water oxidation rate, υ is the scan rate.

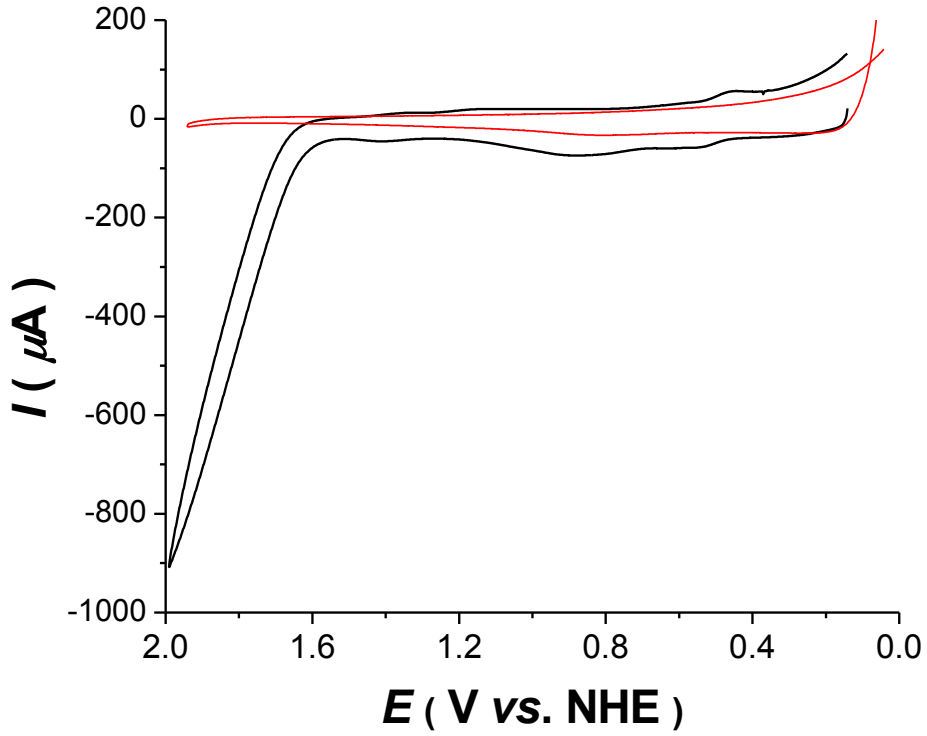

Figure 4-17. Cyclic voltammograms of FTO|*nano*ATO|1-PO_3H_2 (black line) and bare FTO|*nano*ATO electrode at scan rate 10 mV/s in pH 1 $HClO_4$. Sb % molar ratio = 10 %.

Water oxidation catalytic rate, k_{obs}, for **1-PO_3H_2** on nanoATO was readily evaluated by equation 4-2 with i_c the anodic catalytic current at 1.6 V, i_p the anodic current for $Ru^{III/II}$ couple, n the number of electrons transferred per redox event (n_{cat} = 4, n_p = 1), and υ the scan rate.[44,45] As

b)

a result of CVs for **1-PO_3H_2** bounded *nano*ATO in pH 5 acetate buffer and pH 1 $HClO_4$ (Figure 4-17.), the catalytic rate constant was found to be 0.29 s^{-1} and 0.03 s^{-1} in pH 5 and pH 1 $HClO_4$ respectively. The 10-fold increase for water oxidation rate in pH 5 than pH 1 is ascribed to water as poorer proton acceptor base than CH_3COO^- via APT pathway.

4.3.4 Mesoporous ATO core with TiO_2 shell by atomic layer deposition

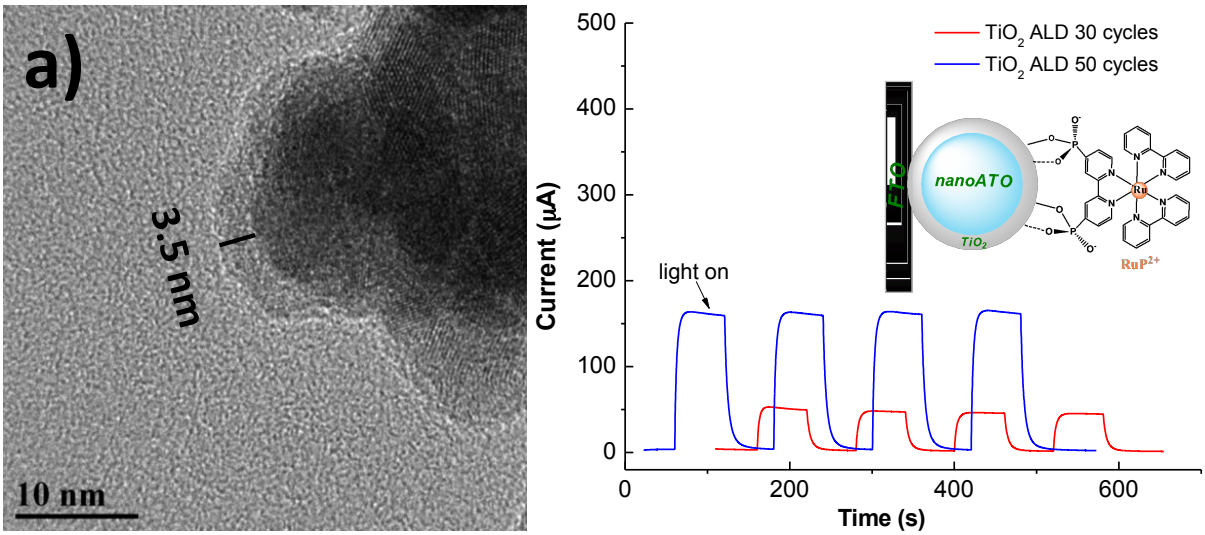

Figure 4-18.(a): HRTEM image of **G1** templated mesoporous ATO atomic layer deposited with 50 cycles TiO_2 layer. TiO_2 shell thickness is 3.5 nm. (b): Photocurrents of **RuP** derivatized 10 % nanoATO-TiO_2 core shell photoanodes applied with 0.2 V vs. NHE under 1.52 mW 445 nm irradiation in 20 mM EDTA aqueous solution of 0.1 M $LiClO_4$.

Core–shell photoanodes consisting of mesoporous conductive metal oxides core like ITO and thin shell of wide-band gap semiconductors, have been successfully applied to DSSCs and photoelectrochemical cells in light of fast electron transfer of the core materials.[12,13] In the present work, mesoporous ATO films were deposited with TiO_2 outer shell and tested their capability as replacement to ITO in core-shell photoanodes. Mesoporous crystalline nanoATO films were coated with an amorphous TiO_2 shell (nanoATO-TiO_2) by atomic layer deposition

(ALD). High-resolution transmission electron microscopy (HRTEM) images demonstrated a TiO_2 shell of 1.9 and 3.5 nm thickness by 30 and 50 deposition cycles (Figure 4-18a).

A photoelectrochemical cell based on $[Ru(bpy)_2(4,4\text{-}(PO_3H_2)_2bpy)]^{2+}$ (**RuP^{2+}**; see Figure 4-18b.) derivatized TiO_2 or Nb_2O_5 as the photoanodes were reported for H_2 evolution in the presence of ethylenediaminete-traacetic tetra-anion (**EDTA^{4-}**) as the reductive scavengers in aqueous solution.[46,47] Mesoporous nanoATO-TiO_2 core shell photoanodes were exploited in the same configuration. The **RuP** surface bounded nanoATO-TiO_2 photoanodes were applied with a 0.2 V vs. NHE bias under a steady state illumination of 1.52 mW in Figure 4-18b, showing that a 3.5 nm shell sample had a higher photoactivity than a 2.0 nm shell. The added scavenger was able to capture Ru^{III} by reduction to Ru^{II}, thus avoiding back electron transfer between photo injected electrons from TiO_2 shell to ATO core, and the oxidized chromophore. Evolved hydrogen was measured by quantitative gas chromatography (GC) after 20 min irradiation. The H_2 quantum efficiency (Φ_{H2}) of a 3.5 nm sample was calculated to be 18 % with 73 % Faradaic efficiency (Φ_{Fa}), while a 1.9 nm sample was calculated to be much lower: 1 % Φ_{H2} and 30 % (equation 4-3 and 4-4). A 3.5 nm sample had a comparable efficiency to nanoTiO_2 photoanode with 92 % Φ_{H2} and 15 % Φ_{Fa}, implying mesoporous ATO electrodes coated with TiO_2 thin shell were suitable core-shell photoanodes in photoelectrochemical cells.

$$\Phi_{\mathrm{Fa}} = \frac{2 \times n_{H_2}}{n_{ex}} \tag{4-3}$$

Where Φ_{Fa} is the Faradaic efficiency, n_{ex} is the number of electron passed during t min by integrating current-time profiles, and n_{H2} is the number of H_2 generated in t min.

$$\Phi_{H_2} = \frac{n_{H_2}}{I_0 \times (1 - 10^{-A_\lambda}) \times t} \tag{4-4}$$

Where n_{H_2} is mole of H_2 produced, I_0 is the incident light intensity at excitation wavelength (445 nm), A_λ is the photoelectrode absorbance at 445 nm excitation wavelength, and t is illumination time.

4.4 Conclusions

We have successfully synthesized mesoporous ATO films by combination of ATO nanocrystals and grafted copolymers PVC-g-POEM. ATO nanoparticles were rapidly prepared through benzyl-alcohol assisted non-aqueous sol gel route under microwave irradiation, which allowed good control of antimony doping, size, and crystallinity. ATO electrodes with high surface area and large mesopores were obtained by pre-made nanocrystals templating by grafted copolymers PVC-g-POEM. Mesoporous ATO films proved themselves suitable alternatives to ITO electrodes in electrochemical catalysis with a ruthenium water oxidation catalyst. Also, mesoporous nanoATO core with a 3.5 nm TiO_2 ALD layer were able to efficiently generate H_2 as nanoTiO_2 in a photoelectrochemical cell.

4.5 REFERENCES

(1) Pan, J. H.; Zhao, X. S.; Lee, W. I. *Chemical Engineering Journal* **2011**, *170*, 363.

(2) Bucknall, D. G.; Anderson, H. L. *Science* **2003**, *302*, 1904.

(3) Hou, K.; Puzzo, D.; Helander, M. G.; Lo, S. S.; Bonifacio, L. D.; Wang, W.; Lu, Z.-H.; Scholes, G. D.; Ozin, G. A. *Adv. Mater.* **2009**, *21*, 2492.

(4) Deng, Y.; Wei, J.; Sun, Z.; Zhao, D. *Chem. Soc. Rev.* **2013**, *42*, 4054.

(5) Wang, Y.; Brezesinski, T.; Antonietti, M.; Smarsly, B. *ACS Nano* **2009**, *3*, 1373.

(6) Müller, V.; Rasp, M.; Rathouský, J.; Schütz, B.; Niederberger, M.; Fattakhova-Rohlfing, D. *Small* **2010**, *6*, 633.

(7) Yu, C.; Fan, J.; Tian, B.; Stucky, G. D.; Zhao, D. *J. Phys. Chem. B* **2003**, *107*, 13368.

(8) Ahn, S. H.; Chi, W. S.; Park, J. T.; Koh, J. K.; Roh, D. K.; Kim, J. H. *Adv. Mater.* **2012**, *24*, 519.

(9) Ahn, S. H.; Chi, W. S.; Kim, D. J.; Heo, S. Y.; Kim, J. H. *Adv. Funct. Mater.* **2013**, *23*, 3901.

(10) Müller, V.; Rasp, M.; Štefanić, G.; Ba, J.; Günther, S.; Rathousky, J.; Niederberger, M.; Fattakhova-Rohlfing, D. *Chem. Mat.* **2009**, *21*, 5229.

(11) Alibabaei, L.; Brennaman, M. K.; Norris, M. R.; Kalanyan, B.; Song, W.; Losego, M. D.; Concepcion, J. J.; Binstead, R. A.; Parsons, G. N.; Meyer, T. J. *Proceedings of the National Academy of Sciences* **2013**, *110*, 20008.

(12) Correa Baena, J. P.; Agrios, A. G. *J. Phys. Chem. C* **2014**.

(13) Alibabaei, L.; Farnum, B. H.; Kalanyan, B.; Brennaman, M. K.; Losego, M. D.; Parsons, G. N.; Meyer, T. J. *Nano Lett.* **2014**.

(14) Yang, Z.; Gao, S.; Li, T.; Liu, F.-Q.; Ren, Y.; Xu, T. *ACS Appl. Mater. Interfaces* **2012**, *4*, 4419.

(15) Ahn, S. H.; Koh, J. H.; Seo, J. A.; Kim, J. H. *Chem. Commun.* **2010**, *46*, 1935.

(16) Lee, K. J.; Park, J. T.; Goh, J. H.; Kim, J. H. *Journal of Polymer Science Part A: Polymer Chemistry* **2008**, *46*, 3911.

(17) Hester, J. F.; Banerjee, P.; Won, Y. Y.; Akthakul, A.; Acar, M. H.; Mayes, A. M. *Macromolecules* **2002**, *35*, 7652.

(18) Norris, M. R.; Concepcion, J. J.; Glasson, C. R. K.; Fang, Z.; Lapides, A. M.; Ashford, D. L.; Templeton, J. L.; Meyer, T. J. *Inorg. Chem.* **2013**, *52*, 12492.

(19) Concepcion, J. J.; Jurss, J. W.; Norris, M. R.; Chen, Z.; Templeton, J. L.; Meyer, T. J. *Inorg. Chem.* **2010**, *49*, 1277.

(20) Cushing, B. L.; Kolesnichenko, V. L.; O'Connor, C. J. *Chem. Rev.* **2004**, *104*, 3893.

(21) Niederberger, M. *Acc. Chem. Res.* **2007**, *40*, 793.

(22) Bilecka, I.; Djerdj, I.; Niederberger, M. *Chem. Commun.* **2008**, 886.

(23) Pinna, N.; Neri, G.; Antonietti, M.; Niederberger, M. *Angew. Chem., Int. Ed.* **2004**, *43*, 4345.

(24) Hu, M.; Xu, J.; Gao, J.; Yang, S.; Wong, J. S. P.; Li, R. K. Y. *Dalton Trans.* **2013**, *42*, 9777.

(25) da Silva, R. O.; Conti, T. G.; de Moura, A. F.; Stroppa, D. G.; Freitas, L. C. G.; Ribeiro, C.; Camargo, E. R.; Longo, E.; Leite, E. R. *ChemPhysChem* **2009**, *10*, 841.

(26) Thangaraju, B. *Thin Solid Films* **2002**, *402*, 71.

(27) Rockenberger, J.; zum Felde, U.; Tischer, M.; Tröger, L.; Haase, M.; Weller, H. *The Journal of Chemical Physics* **2000**, *112*, 4296.

(28) Roh, D. K.; Park, J. T.; Ahn, S. H.; Ahn, H.; Ryu, D. Y.; Kim, J. H. *Electrochim. Acta* **2010**, *55*, 4976.

(29) Buonsanti, R.; Pick, T. E.; Krins, N.; Richardson, T. J.; Helms, B. A.; Milliron, D. J. *Nano Lett.* **2012**, *12*, 3872.

(30) Milliron, D. J.; Buonsanti, R.; Llordes, A.; Helms, B. A. *Acc. Chem. Res.* **2013**, *47*, 236.

(31) Nütz, T.; Felde, U. z.; Haase, M. *The Journal of Chemical Physics* **1999**, *110*, 12142.

(32) Sharma, S.; Volosin, A. M.; Schmitt, D.; Seo, D.-K. *Journal of Materials Chemistry A* **2013**, *1*, 699.

(33) Wu, J.; Chen, F.; Shen, Q.; Schoenung, J. M.; Zhang, L. *J. Nanomaterials* **2013**, *2013*, 2.

(34) Peng, Q.; Kalanyan, B.; Hoertz, P. G.; Miller, A.; Kim, D. H.; Hanson, K.; Alibabaei, L.; Liu, J.; Meyer, T. J.; Parsons, G. N.; Glass, J. T. *Nano Lett.* **2013**, *13*, 1481.

(35) Hoertz, P. G.; Chen, Z.; Kent, C. A.; Meyer, T. J. *Inorg. Chem.* **2010**, *49*, 8179.

(36) Chen, Z.; Vannucci, A. K.; Concepcion, J. J.; Jurss, J. W.; Meyer, T. J. *Proceedings of the National Academy of Sciences* **2011**, *108*, E1461.

(37) Chen, Z.; Concepcion, J. J.; Jurss, J. W.; Meyer, T. J. *J. Am. Chem. Soc.* **2009**, *131*, 15580.

(38) Trammell, S. A.; Meyer, T. J. *J. Phys. Chem. B* **1998**, *103*, 104.

(39) Vannucci, A. K.; Hull, J. F.; Chen, Z.; Binstead, R. A.; Concepcion, J. J.; Meyer, T. J. *J. Am. Chem. Soc.* **2012**, *134*, 3972.

(40) Méndez, M. A.; Alibabaei, L.; Concepcion, J. J.; Meyer, T. J. *ACS Catal* **2013**, *3*, 1850.

(41) Concepcion, J. J.; Jurss, J. W.; Templeton, J. L.; Meyer, T. J. *J. Am. Chem. Soc.* **2008**, *130*, 16462.

(42) Chen, Z.; Concepcion, J. J.; Hu, X.; Yang, W.; Hoertz, P. G.; Meyer, T. J. *Proc. Natl. Acad. Sci. USA* **2010**, *107*, 7225.

(43) Concepcion, J. J.; Tsai, M.-K.; Muckerman, J. T.; Meyer, T. J. *J. Am. Chem. Soc.* **2010**, *132*, 1545.

(44) Vannucci, A. K.; Alibabaei, L.; Losego, M. D.; Concepcion, J. J.; Kalanyan, B.; Parsons, G. N.; Meyer, T. J. *Proceedings of the National Academy of Sciences* **2013**.

(45) Nakagawa, T.; Beasley, C. A.; Murray, R. W. *J. Phys. Chem. C* **2009**, *113*, 12958.

(46) Luo, H.; Song, W.; Hoertz, P. G.; Hanson, K.; Ghosh, R.; Rangan, S.; Brennaman, M. K.; Concepcion, J. J.; Binstead, R. A.; Bartynski, R. A.; Lopez, R.; Meyer, T. J. *Chem. Mat.* **2012**, *25*, 122.

(47) Song, W.; Brennaman, M. K.; Concepcion, J. J.; Jurss, J. W.; Hoertz, P. G.; Luo, H.; Chen, C.; Hanson, K.; Meyer, T. J. *J. Phys. Chem. C* **2011**, *115*, 7081.